

FMM accelerated BEM for 3D Laplace & Helmholtz Equations

Nail A. Gumerov and Ramani Duraiswami

Institute for Advanced Computer Studies, University of Maryland, College Park, MD 20742

Abstract

We describe development of a fast multipole method accelerated iterative solution of boundary element equations for large problems involving hundreds of thousands elements for the Laplace and Helmholtz equations in 3D. The BEM requires several approximate computations (numerical quadrature, approximations of the boundary shapes using elements) and the convergence criterion for iterative computation. When accelerated using the FMM, these different errors must all be chosen in a way that on the one hand excess work is not done and on the other that the error achieved by the overall computation is acceptable. We show results of developed and tested solvers for the boundary value problems for the Laplace and Helmholtz equations using the BEM/GMRES/FMM. The performance tests for both were conducted in the range $N \lesssim 10^6$ and $kD \lesssim 150$ (in the Helmholtz case) and showed good performance close to theoretical expectations.

1 Introduction

For many problems boundary integral (or element) methods have long been considered as very promising. They can handle complex shapes, lead to problems in boundary variables alone, and lead to simpler meshes as the boundary alone must be discretized rather than the entire domain. Despite these advantages, one issue that has impeded their widespread adoption of these methods is that the integral equation techniques lead to linear systems with dense and possibly non-symmetric matrices, for which efficient iterative solvers may not be available. For problems with N unknowns this requires storage of $O(N^2)$ elements of these matrices. The computation of the individual matrix elements is expensive requiring quadrature of singular or hypersingular functions. To reduce the singularity order and achieve symmetric matrices, many investigators employ Galerkin techniques, which lead to further $O(N^2)$ integral computations. Direct solution of the linear systems has an $O(N^3)$ cost. Use of iterative methods can reduce the cost to $O(N_{iter}N^2)$ operations, where N_{iter} is the number of iterations required, but this is still quite large. An iteration strategy that minimizes N_{iter} is also needed. These expenses have meant that the BEM was not used for very large problems.

The development of the fast multipole method (FMM) [4] and use of Krylov iterative methods presents a promising approach to improving the scalability of integral equation methods. The FMM allows the matrix vector product to be performed to a given precision ϵ in $O(N \log N)$ operations, and further does not require the computation or storage of all N^2 elements of the matrices, reducing the storage costs to $O(N \log N)$ as well. Incorporating this fast matrix vector product in a quickly convergent iterative scheme allows the system to be rapidly solved with $O(N_{iter}N \log N)$ cost.

The FMM for the Laplace and Helmholtz equations exploits factorized local and far-field (multipole) expansions of the Green's function obtained via the addition theorem. The basic idea of the FMM is to truncate the infinite series up to p^2 terms in 3D, and use translation operators for reexpansion of the solution about an arbitrary spatial point. The translation operators are also replaced by approximate (truncated) operators. In the original FMM the translation cost for a $O(p^2)$ representation was $O(p^4)$. Subsequent improvements lead to translation methods with costs of $O(p^3)$, $O(p^2 \log p)$ and even $O(p^2)$, though in the latter two cases the asymptotic notation hides a large constant cost. Later this method was intensively studied and extended to solution of many other problems. While the literature and previous work is extensive, reasons of space do not permit us to discuss them. We refer the reader to the comprehensive review [9].

Our particular interest is in the combination of the FMM with the BEM in 3D for solving the Laplace equation, and the Helmholtz equation at low to moderate frequencies. The case of the Helmholtz and the related Maxwell equations is somewhat more complicated, and the development of boundary-element/FMM combinations for different equations is a matter of more recent research. Of particular interest to the initial authors were relatively high frequency applications for which the FMM based on spherical expansion representations of multipoles was not competitive with direct matrix vector products. The development of diagonal translation operators [11] alleviated this difficulty. However, these made the implementation of the FMM/BEM more complex and subject to instabilities at low frequencies, and as a consequence again not too widely adopted.

Contributions of the present paper: In fact the FMM for both the Laplace and Helmholtz equations at moderate frequencies can be handled well by $O(p^3)$ translation techniques based on a decomposition of the translation to rotation and coaxial translations (see [5, 8]). As discussed earlier the FMM requires $O(N)$ or $O(N \log N)$ storage space and $O(N)$ or so operations for the matrix-vector product. While one may wonder about the accuracy of the FMM, where exactness is

sacrificed for the speed, we should emphasize, first, that in practice this accuracy can be made close to machine precision, second, that in the iteration procedures the accuracy should be consistent with the criterion to stop the iterative process, and, finally, that the accuracy of the FMM should be considered together with accuracy of the BEM technique, which employs surface approximation via discretization and approximate computation of the boundary integrals, and based on our experience introduce larger errors than the FMM does. Moreover, we note that for accurate solution of the Helmholtz equation the size of the boundary elements should be much smaller than the wavelength, which produces severe constraints for high frequency problems. Given these considerations it is possible to develop effective large scale FMM solutions. We must emphasize that several other authors (e.g., [10, 13]) have developed FMM/BEM algorithms. Here our intention is to present some aspects of our implementations. In particular our approach is characterized by the use of the Green's identity or layer potentials ("indirect" BEM), collocation techniques, Krylov iterative methods that may be preconditioned, and an overall choice of techniques that have a consistent accuracy in all aspects of the algorithm. The results of solutions of the test problems and issues related to errors and performance of the methods employed are discussed.

2 Problem formulation

We consider boundary value problems for a complex potential ϕ satisfying the Laplace or Helmholtz equations on a finite or infinite domain V in 3D, and subject to boundary conditions on S , the boundary of the domain:

$$\nabla^2 \phi = 0, \quad \nabla^2 \phi + k^2 \phi = 0, \quad \mathbf{x} \in V \subset \mathbb{R}^3, \quad k \in \mathbb{R}, \quad (1)$$

$$\alpha(\mathbf{x}) \phi(\mathbf{x}) + \beta(\mathbf{x}) q(\mathbf{x}) = \gamma(\mathbf{x}), \quad \mathbf{x} \in S, \quad q(\mathbf{x}) = \frac{\partial \phi}{\partial n}(\mathbf{x}) = \mathbf{n}(\mathbf{x}) \cdot \nabla \phi(\mathbf{x}). \quad (2)$$

Here α , β , and γ are some specified complex valued functions on S and \mathbf{n} is the exterior normal. For infinite domains we assume ϕ decays to zero for the Laplace equation and satisfies the Sommerfeld condition for the Helmholtz equation,

$$\lim_{|\mathbf{x}| \rightarrow \infty} \phi = 0, \quad \lim_{|\mathbf{x}| \rightarrow \infty} \left(|\mathbf{x}| \left(\frac{\partial \phi}{\partial |\mathbf{x}|} - ik\phi \right) \right) = 0. \quad (3)$$

Arbitrary solutions to these equations can be expressed as sums of the single and double layer potentials

$$\phi(\mathbf{y}) = \mathbf{K}(\sigma(\mathbf{x})) + \mathbf{L}(p(\mathbf{x})), \quad \mathbf{x} \in S, \quad \mathbf{y} \in V \quad (4)$$

$$\mathbf{K}(\sigma(\mathbf{x})) = \int_S \sigma(\mathbf{x}) G(\mathbf{x} - \mathbf{y}) dS(\mathbf{x}), \quad \mathbf{L}(p(\mathbf{x})) = - \int_S p(\mathbf{x}) \frac{\partial G(\mathbf{x} - \mathbf{y})}{\partial n(\mathbf{x})} dS(\mathbf{x}),$$

where σ and p are surface densities, while G is the free space Green's function for the Laplace or the Helmholtz operators:

$$G(\mathbf{x} - \mathbf{y}) = \frac{1}{4\pi|\mathbf{x} - \mathbf{y}|}, \quad G(\mathbf{x} - \mathbf{y}) = \frac{e^{ik|\mathbf{x} - \mathbf{y}|}}{4\pi|\mathbf{x} - \mathbf{y}|}, \quad (5)$$

respectively. For both equations Green's identity holds, which is equation (4) with $\sigma(\mathbf{x}) = \pm q(\mathbf{x})$ and $p(\mathbf{x}) = \pm \phi(\mathbf{x})$ (here the upper sign refers to the interior and the lower sign to the exterior problem), and which can be used to obtain ϕ in the domain if the potential and its normal derivative are known on the boundary. This leads to the integral equation

$$\pm \frac{1}{2} \phi(\mathbf{y}) = \mathbf{K}(q(\mathbf{x})) + \mathbf{L}(\phi(\mathbf{x})), \quad \mathbf{x} \in S, \quad \mathbf{y} \in S, \quad (6)$$

which can be used together with Eq. (2) for determination of the boundary values. To avoid spurious eigenvalues for the external BEM one of possibilities to resolve this is to stay within the layer potential formulation [1], which provides according to the jump conditions:

$$\phi^\pm(\mathbf{y}) = \pm \frac{1}{2} p(\mathbf{y}) + \mathbf{K}(\sigma(\mathbf{x})) + \mathbf{L}(p(\mathbf{x})), \quad \mathbf{x} \in S, \quad \mathbf{y} \in S, \quad (7)$$

$$q^\pm(\mathbf{y}) = \pm \frac{1}{2} \sigma(\mathbf{y}) + \mathbf{K}'(\sigma(\mathbf{x})) + \mathbf{L}'(p(\mathbf{x})), \quad \mathbf{x} \in S, \quad \mathbf{y} \in S,$$

$$\mathbf{K}'(\sigma(\mathbf{x})) = \frac{\partial}{\partial n(\mathbf{y})} \mathbf{K}(\sigma(\mathbf{x})), \quad \mathbf{L}'(\sigma(\mathbf{x})) = \frac{\partial}{\partial n(\mathbf{y})} \mathbf{L}(\sigma(\mathbf{x})), \quad \mathbf{x} \in S, \quad \mathbf{y} \in S. \quad (8)$$

This can be used for solution of the Helmholtz equation, with $\sigma(\mathbf{x}) = i\eta p(\mathbf{x})$, where η is some complex parameter. In this case equations (7) and (2) lead to the following single integral equation for the layer potential density

$$\alpha(\mathbf{y}) \left\{ \pm \frac{1}{2} p(\mathbf{y}) + i\eta \mathbf{K}(p(\mathbf{x})) + \mathbf{L}(p(\mathbf{x})) \right\} + \beta(\mathbf{y}) \left\{ \pm \frac{1}{2} i\eta p(\mathbf{y}) + i\eta \mathbf{K}'(p(\mathbf{x})) + \mathbf{L}'(p(\mathbf{x})) \right\} = \gamma(\mathbf{y}). \quad (9)$$

Particularly for the external (scattering) problems, which solution is unique, this avoids spurious internal resonances.

3 BEM speed up with the FMM

Several schemes of coupling the BEM with the FMM can be thought, and we also tried a few until we came to the following, rather simple scheme. A matrix-vector product of type $\mathbf{A}\mathbf{u}$ is required. \mathbf{A} is represented as

$$\mathbf{A} = \mathbf{A}_{sparse} + \mathbf{A}_{dense}, \quad (10)$$

where \mathbf{A}_{sparse} can be computed directly using standard quadratures over the element i , for elements j which are in the neighborhood of i . This neighborhood size is a user controllable parameter, and can be varied as needed. The dense part includes most pairwise interactions. As it includes only remotely located elements relatively low order quadrature can be used for them to achieve the required accuracy. Moreover, in our test implementations we used surface discretization with flat triangular elements, for which we used a constant approximation of the unknown function (potential or its normal derivative) over the panel. In this case we also can expect that the Greens function and its derivatives for relatively distant interactions can be approximated in the same way at the same accuracy, and was confirmed by our numerical experiments.

BEM and FMM data structures: Detailed description of the FMM for the Laplace and Helmholtz equations can be found elsewhere [4, 7] and here we just point out few details on the use of the FMM with the BEM. First we note that the data structure of the FMM is based on the octree space subdivision up to some level l_{max} . Selection of l_{max} is dictated by an optimization problem for FMM costs, which balances the costs of the translation and direct summation operations. Deviations from optimal l_{max} are not desirable, as they heavily influence the FMM performance [7]. On the other hand the split in (10) is dictated by the accuracy of the BEM and therefore the size of the neighborhood where we perform direct computations of integrals may not coincide with the sizes of neighborhoods at different levels of the FMM. Our numerical tests show that (fortunately) the size of the neighborhood at the optimal maximum space subdivision level is larger than the size required for direct integral evaluations. This means that all elements which intersect the neighborhood of an element i at the finest level, and whose contribution to the potential at the element center can be classified into two sets. First are the elements j that are closer than some distance r_{min} from the center of i to the closest corner of j . The contribution of these elements is performed using higher order quadrature or special integral treatment (for singular and hypersingular integrals) as in the conventional BEM. The second set of elements are located further than r_{min} . Their contribution is taken into account using low order quadrature, as they are remote in the sense of BEM, but close in the sense of the FMM.

Iterative methods: The basic iterative method we used is the Generalized Minimal Residual Method (GMRES) and its modifications (flexible GMRES, fGMRES) [12], which allow the use of various FMM-based preconditioners [6]. In all cases for the Laplace equation and for the Helmholtz equation at low frequencies unpreconditioned GMRES showed good results, while the convergence rate of this method for the Helmholtz equation substantially reduces at higher frequencies.

Computation of normal derivatives in the FMM: Eq. (9) requires four matrix-vector products, and the use of Eq. (6) requires two matrix-vector products (in the case of mixed boundary conditions). These can be performed by the FMM in a single run, as for a single matrix-vector product. Indeed, the first step of the regular FMM is to build multipole expansions about the centers of the source boxes, \mathbf{x}_* . We handle this step using expansions of Greens function over the multipole basis functions $S_n^m(\mathbf{r})$:

$$G(\mathbf{y} - \mathbf{x}) \approx \sum_{n=0}^{p-1} \sum_{m=-n}^n C_n^m S_n^m(\mathbf{y} - \mathbf{x}_*), \quad C_n^m = C_n^m(\mathbf{x}, \mathbf{x}_*), \quad (11)$$

where p is the truncation number, and expressions for coefficients C_n^m for the Laplace and Helmholtz equations can be found elsewhere [7, 8]. We compute the normal derivative of arbitrary function $F(\mathbf{x})$, which can be expanded into a series over the basis functions with coefficients $\{C_n^m\}$ using sparse-matrix differential operators $\{D_{nn'}^{mm'}\}$:

$$\mathbf{n} \cdot \nabla_{\mathbf{x}} F(\mathbf{x}) \approx \sum_{n=0}^{p-1} \sum_{m=-n}^n B_n^m S_n^m(\mathbf{y} - \mathbf{x}_*), \quad \{B_n^m\} = \{D_{nn'}^{mm'}(\mathbf{n})\} \{C_{n'}^{m'}\}, \quad B_n^m = \sum_{n'=0}^{p-1} \sum_{m'=-n'}^n \sum_{m''=0}^{p-1} \sum_{m'''=-n''}^{n''} D_{nn'}^{mm'} C_{n'}^{m'}. \quad (12)$$

Expressions for $D_{nn'}^{mm'}$ for the Helmholtz equation can be found in [7], while for the Laplace equation can be derived from relations in [3]. Therefore far field expansions of the boundary integrals can be written as

$$\begin{aligned} & \sigma_j \int_{S_j} G(\mathbf{y} - \mathbf{x}) dS(\mathbf{x}) + p_j \int_{S_j} \mathbf{n} \cdot \nabla_{\mathbf{x}} G(\mathbf{y} - \mathbf{x}) dS(\mathbf{x}) \\ & \approx \sigma_j \sum_{q=1}^Q w_q^{(j)} G(\mathbf{y} - \mathbf{x}_q^{(j)}) + p_j \sum_{q=1}^Q w_q^{(j)} \mathbf{n}_j \cdot \nabla_{\mathbf{x}} G(\mathbf{y} - \mathbf{x}_q^{(j)}) \approx \sum_{n=0}^{p-1} \sum_{m=-n}^n A_n^{(j)m} S_n^m(\mathbf{y} - \mathbf{x}_*), \\ & A_n^{(j)m} = \sum_{q=1}^Q w_q^{(j)} \left(\sigma_j C_n^m(\mathbf{x}_q^{(j)}, \mathbf{x}_*) + p_j B_n^{(j)m}(\mathbf{x}_q^{(j)}, \mathbf{x}_*) \right), \quad \{B_n^m\} = \{D_{nn'}^{mm'}(\mathbf{n}_j)\} \{C_{n'}^{m'}\}, \end{aligned} \quad (13)$$

where Q is the order of quadrature over the boundary element S_j with weights $w_q^{(j)}$ and abscissas $\mathbf{x}_q^{(j)}$. A similar situation holds at the evaluation step if using the method of layer potentials, where derivatives $\mathbf{n}(\mathbf{y}) \cdot \nabla_{\mathbf{y}}$ can be computed using respective sparse-matrix differential operator on the expansion coefficients.

4 Laplace equation

Performance tests for the Laplace equation were conducted for multiparticle geometries of type shown in Fig. 1. Analytical solution was generated as a sum of monopoles placed at the center of each ellipsoid, which total intensity was 1. The Dirichlet problem was solved using the BEM and the obtained normal derivatives were compared with the analytical values to evaluate the error of the numerical method. The function values and normal derivatives were computed at mesh vertices (using standard averaging over the elements containing the same vertex), which number is referred further as N (the number of elements was approximately twice larger).

Four methods implemented in Fortran 90 in double precision and compared. First, we used standard BEM, where the BEM matrices were computed, stored, and the linear system resulting from Green's identity was solved using LU-decomposition from LAPACK. Second, the BEM matrices were computed and stored, while unpreconditioned GMRES (CERFACS software available online) was used for iterative solution of the resulting system with a prescribed error $\epsilon = 10^{-5}$ for termination of the process. We checked that in all cases this was sufficient to provide the same error in the numerical solution (relative error of order 10^{-2}). The first two methods require $O(N^2)$ memory for storage of the BEM matrices, and our computational resources limited us to compute problems of size smaller than $N \simeq 10^4$. The other two methods tested required only $O(N)$ memory and so could be used for computation of larger problems on the same computer. Method 3 was the same as Method 2 with the only difference that the entries of the BEM matrices were recomputed each time the matrix-product was requested, thereby avoiding storage. The last method used combined the same GMRES with the same termination error and the FMM for matrix-vector multiplication, where we used truncation number $p = 8$ for all cases. We checked that the error of solution was practically the same for $N \lesssim 10^4$ as for other methods, while for larger N the error decays and stays within the range 10^{-2} - 10^{-4} . Higher accuracy ($\sim 10^{-6}$) was achievable for larger N by increasing p and decreasing ϵ .

Fig. 2 shows that the CPU times for methods 1-4 are scaled approximately as $O(N^3)$, $O(N^2)$, $O(N^2)$, and $O(N)$, respectively, which is consistent with the theory assuming that the number of iterations does not change with N . In fact, the number of iterations do increase slowly with N as shown in Fig. 2 right, which explains deviation of the total CPU time from the linear dependence at larger N . The number of iterations was the same for methods 2-4, except for $N = 488$ where the first two methods converged for 10 iterations, while the FMM-based needed 13 iterations. For $N = 843,264$ (1,679,616 elements, 1728 ellipsoids) the number of iterations was 31 (total CPU time for solution 28 min 19 s, which includes precomputations of the near element interactions, preset of the FMM, and the iterative process with 48 s per matrix vector multiplication).

5 Helmholtz equation

The tests of the BEM for the Helmholtz equation were performed by solution of acoustic scattering problems off objects of different shape. The objects were sound-hard leading to an external Neumann problem for the scattered field. As a test we selected scattering of the plane incident wave from a single sphere, which has an analytical solution in the form of the infinite series (due to Lord Rayleigh, can be found elsewhere, e.g. [7]). These series can be appropriately truncated and the error of the solution can be accurately estimated. We performed tests using the same four methods as reported for the Laplace equation, plus we compared solutions obtained using boundary integral equations resulting from the layer potential and Green's identity. Also some tests using the fGMRES with different preconditioners were performed.

In this paper we report only results obtained using the unpreconditioned GMRES and Green's identity. Fig. 3 shows scattering off a sphere. The numerical solution reproduces fine oscillating structure of the acoustic field near the point $\theta = 180^\circ$ which happens at large ka , where a is the sphere radius. Even the use of high frequency mesh with 480,000

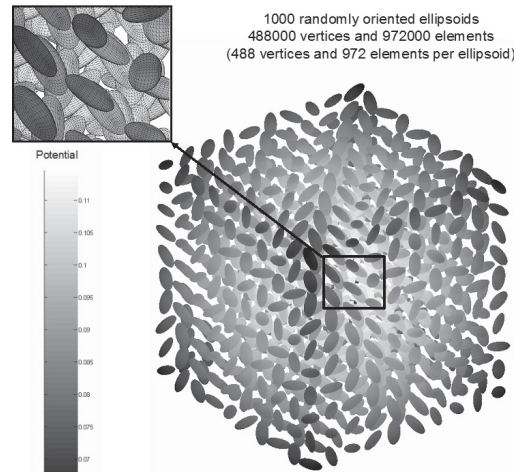


Figure 1: Geometry of the test problems for performance tests for the Laplace equation. Centers of M^3 equal ellipsoids were placed on a cubic grid and each ellipsoid was randomly rotated.

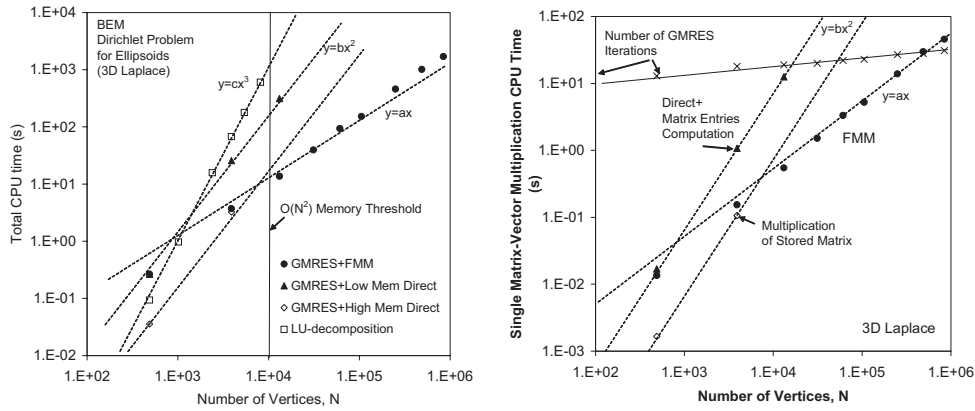


Figure 2: *Left*: Performance of the 4 BEM methods for the Dirichlet problem for the Laplace equation on the domain with a collection of ellipsoids shown in Fig 1. *Right*: CPU time for a single matrix vector multiply. Between 13 and 31 iterations are needed for convergence and are indicated via crosses. (Intel Xeon 3.2 GHz processor with 3.5 GB RAM.)

elements for $ka = 30$ provided $k\delta = 0.4$, where δ is the size of the largest boundary element (about 16 elements per wavelength). Computations of this were performed with 6 levels of the octree with maximum truncation number $p = 22$ at level 2, and convergence to error $\epsilon = 10^{-5}$ took 115 iterations.

The CPU time required for solution of the problem with $ka = 10$ using different methods is shown in Fig. 4. As the kD for different N is fixed ($kD = 34.64$) the methods as in the case of the Laplace equation show scaling close to $O(N^3)$, $O(N^2)$, $O(N^2)$, and $O(N)$, respectively. In the reported case the accuracy of the solution was 0.15 for case $N = 1016$, was $\approx 10^{-2}$ for $N \sim 10^4$ and dropped to $\sim 10^{-4}$ for $N \sim 10^6$ despite the maximum truncation number used in the FMM ($p = 12$) and the GMRES termination criteria ($\epsilon = 10^{-5}$) were the same. This change in the accuracy is due to two factors, first, for the low frequency mesh parameter $k\delta$ was large enough, and second, that finer mesh approximated the sphere better. In contrast to the Laplace equation the number of iterations slightly decreased at increasing N (see Fig. 4 right). This explains the deviation of the total CPU time below the linear asymptote, as the CPU time for the FMM matrix vector product scales almost linearly (Fig. 4 right). For $N \gtrsim 10^3$ direct matrix vector product with recomputation of matrix elements was slower. Note that the FMM for the Helmholtz equation is slower than for the Laplace equation since for the Helmholtz case all variables are complex.

Finally we applied the software for solution of some scattering problems related to hearing. This requires solution of the Helmholtz equation in domains with complex boundaries, such as a human or animal head, and ears for a range of audible frequencies, in the range $kD \lesssim 100$, for which the developed BEM/FMM works well. Parameters such as sound pressure or head related transfer functions (HRTF) are computed. Fig. 5 provides one such case. (A color movie visualizing scattering can be viewed online on the web sites of the authors.)

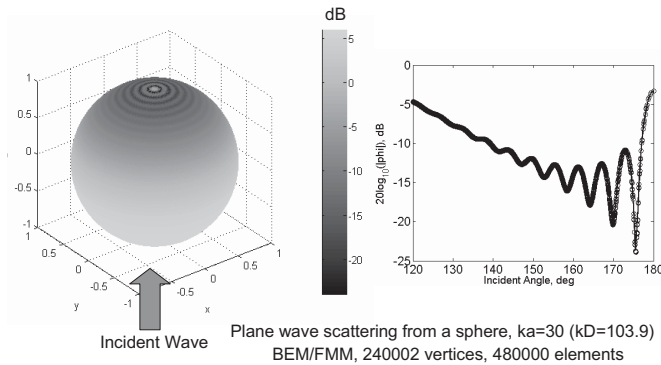


Figure 3: Scattering of a plane wave from a sound-hard sphere. The incidence angle is 0 for the front point and 180° for the rear point.

References

[1] Chen, L.H and Zhou, J. (1992) *Boundary Element Methods*. Academic Press.

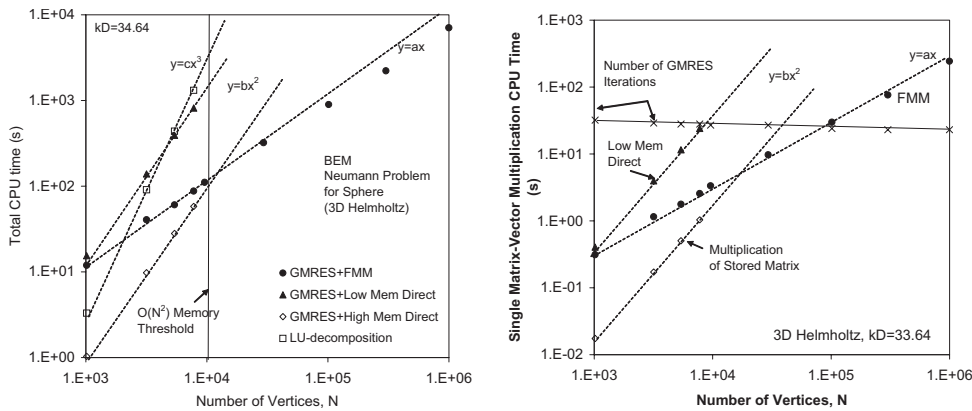


Figure 4: *Left*: CPU time for computation of scattering off a sphere in a domain of size $kD = 34.64$ as a function of the degrees of freedom. *Right*: Dependence of the matrix vector multiplication time for the Helmholtz equation on the number of degrees of freedom for the case on the left. The crosses show the number of iterations.



Figure 5: An example of computation of sound scattering from bunny model using the BEM/FMM. The sound pressure for different frequencies at some moment of time is shown on the bottom pictures.

- [2] Colton, D. and Kress, R. 1998 *Inverse Acoustic and Electromagnetic Scattering Theory*. 2nd. ed. Berlin: Springer..
- [3] M.A. Epton and B. Dembart, Multipole translation theory for the three-dimensional Laplace and Helmholtz equations, *SIAM J. Sci. Comput.*, 16(4), 1995, 865-897.
- [4] Greengard, L. (1988). *The Rapid Evaluation of Potential Fields in Particle Systems*. (MIT Press, Cambridge, MA).
- [5] Gumerov, N.A., and Duraiswami, R. (2003). "Recursions for the computation of multipole translation and rotation coefficients for the 3-D Helmholtz equation," *SIAM J. Sci. Stat. Comput.* 25(4), 1344-1381, 2003.
- [6] Gumerov, N.A. and Duraiswami, R. (2005). "Computation of scattering from clusters of spheres using the fast multipole method," *J. Acoust. Soc. Am.*, 117 (4), Pt. 1, 1744-1761.
- [7] Gumerov, N.A. and Duraiswami, R. (2005) *Fast Multipole Methods for the Helmholtz Equation in Three Dimensions*. (Elsevier, Oxford, UK).
- [8] Gumerov, N.A. and Duraiswami, R. (2005) "Comparison of the efficiency of translation operators used in the fast multipole method for the 3D Laplace equation, Technical Report UMIACS-TR-#2005-09, University of Maryland.
- [9] N. Nishimura, Fast multipole accelerated boundary integral equation methods, *Appl Mech* .55 (2002) 299-324.
- [10] Ramaswamy D, Ye W, Wang X, and White J (1999), Fast algorithms for 3-D simulation, *J. Modeling Simulation of Microsystems*, 1, 77-82.
- [11] Rokhlin, V. (1993). "Diagonal forms of translation operators for the Helmholtz equation in three dimensions," *Appl. and Comp. Harmonic Analysis*, 1, 82-93.
- [12] Saad, Y.(1993). "A flexible inner-outer preconditioned GMRES algorithm," *SIAM J. Sci. Comput.* 14(2), 461-469.
- [13] Sakuma, T. and Yasuda, Y. (2002). Fast multipole boundary element method for large-scale steady-state sound field analysis, part i: Setup and validation. *Acustica/Acta Acustica*, 88:513-525.

An iterative boundary element method for the determination of a spacewise dependent heat source

T. Johansson¹ and D. Lesnic²

Department of Applied Mathematics, University of Leeds, LS2 9JT Leeds, UK

e-mail: ¹amt02tj@maths.leeds.ac.uk ²amt5ld@maths.leeds.ac.uk

Keywords: Boundary element method, discrepancy principle, heat source, inverse problem, iterative regularization, parabolic heat equation

Abstract. This paper investigates the inverse problem of determining a spacewise dependent heat source in the parabolic heat equation using the usual conditions of the direct problem and information from a supplementary temperature measurement at a given single instant of time. The spacewise dependent temperature measurement ensures that the inverse problem has a unique solution, but this solution is unstable, hence the problem is ill-posed. For this inverse problem, we propose an iterative algorithm based on a sequence of well-posed direct problems which are solved at each iteration step using the boundary element method (BEM). The instability is overcome by stopping the iterations at the first iteration for which the discrepancy principle is satisfied. Numerical results are presented for a typical benchmark test example which has the input measured data perturbed by increasing amounts of random noise. Provided that the iterative algorithm is stopped once this discrepancy principle is satisfied then a stable numerical solution is obtained. Furthermore, as the amount of noise included in the input data decreases the stable numerical solution approaches more accurately the available analytical solution. Work in progress involves a rigorous mathematical analysis of the procedure including proof of convergence and stability. Further work will be concerned with developing a similar approach for solving a more severe inverse problem in which measurements of the temperature in the solution domain at two different instants are used to determine both the spacewise dependent source and the initial temperature.

Introduction

The inverse problem of determining an unknown inhomogeneous spacewise dependent heat source function in the heat conduction equation has been considered in a few theoretical papers concerned with the existence and uniqueness of the solution, notably in [1, 2] and [3]. However, as yet no numerical algorithms have been attempted under such rigorous mathematical back-up. In this paper, the determination of the unknown heat source is sought from the usual conditions of the direct problem and a temperature measurement along the domain at a given single instant of time. Although sufficient conditions for the solvability of the inverse problem are provided, the problem is still ill-posed since small errors, inherently present in any practical measurement, give rise to unbounded and highly oscillatory solutions. Therefore, in this paper, in order to overcome the instability of the solution, an iterative regularizing algorithm is proposed which recasts the inverse problem into a sequence of well-posed direct problems. These direct problems are solved numerically at each iteration step using the BEM until a prescribed stopping criterion is satisfied.

Formulation of the Inverse Problem

Let $T > 0$ and $\ell > 0$ be fixed numbers. Let $L^2((0, \ell))$ be the space of square integrable real-valued functions on the interval $(0, \ell)$ with the usual norm. The space $H^k((0, \ell))$, where $k = 1, 2, \dots$, denotes the standard Sobolev space on $(0, \ell)$, i.e., the space of functions with generalized derivatives of order $\leq k$ in $L^2((0, \ell))$. By $H_0^1((0, \ell))$ we mean the subspace of functions u in $H^1((0, \ell))$ with $u(0) = u(\ell) = 0$.

We consider the following inverse problem: Find the temperature u and the heat source f which satisfy the heat conduction equation with a space-dependent heat source, namely

$$u_t(x, t) = u_{xx}(x, t) + f(x), \quad \text{for } (x, t) \in (0, \ell) \times (0, T), \quad (1)$$

subject to the Dirichlet boundary conditions

$$u(0, t) = h_0(t), \quad u(\ell, t) = h_\ell(t), \quad \text{for } t \in (0, T), \quad (2)$$

the initial condition

$$u(x, 0) = \psi_0(x), \quad \text{for } x \in (0, \ell), \quad (3)$$

and the overspecified (upper-base) condition

$$u(x, T) = \psi_T(x), \quad \text{for } x \in (0, \ell). \quad (4)$$

Under suitable conditions, this inverse problem has a unique solution. Indeed, let the following consistency condition be satisfied, $h_j(0) = \psi_0(j)$ and $h_j(T) = \psi_T(j)$, for $j = 0, \ell$. Using the trace theorem, it is sufficient to consider the case when $h_0 = h_\ell = 0$ which will be assumed in the remainder of the paper. Then uniqueness follows from the following theorem, see [4].

Theorem 2.1. *Let $h_0 = h_\ell = 0$ and assume that $\psi_0, \psi_T \in H_0^1((0, \ell)) \cap H^2((0, \ell))$. Then the inverse problem (1)–(4) has a unique solution among sources $f \in L^2((0, \ell))$ and temperatures u with*

$$\int_0^T \left(\|u_t(\cdot, t)\|_{L^2((0, \ell))}^2 + \|u(\cdot, t)\|_{H^2((0, \ell))}^2 \right) dt < \infty.$$

There also exist uniqueness results in Hölder spaces, see [3].

In order to overcome the instability of the inverse problem (1)–(4) with respect to noise in the data (1), we develop an iterative BEM regularizing algorithm, as described in the next section.

An Iterative Algorithm for Finding the Source Term

The procedure for the stable reconstruction of the solution u and source term f in (1)–(4) runs as follows:

- (i) Choose a function $f_0 \in L^2((0, \ell))$. Let u_0 be the solution to (1)–(3) with $f = f_0$.
- (ii) Assume that f_k and u_k have been constructed. Let v_k solve (1)–(3) with $f(x) = u_k(x, T) - \psi_T(x)$ and $\psi_0 = 0$.
- (iii) Let

$$f_{k+1}(x) = f_k(x) - \gamma v_k(x, T),$$

where $\gamma > 0$, and let u_{k+1} solve (1)–(3) with $f = f_{k+1}$.

The procedure continues by repeating the last two steps until a desired level of accuracy is achieved.

Well-Posedness of the Problems in the Iterative Procedure

Here, we discuss the well-posedness of the problems used in the iterative procedure given in the previous section. The space $L^2(0, T; X)$, where X is a Hilbert space, denotes the space of measurable functions $u : (0, T) \rightarrow X$, such that

$$\int_0^T \|u(t)\|_X^2 dt < \infty.$$

By $C([0, T]; X)$ we mean functions u such that the mapping $u(\cdot, t) : [0, T] \rightarrow X$ is continuous. A proof of the following lemma is given in Chapter 3 of [5].

Lemma 4.1. *Let $h_0 = h_\ell = 0$. Suppose that ψ_0 and f belong to $L^2((0, \ell))$. Then (1) has a unique solution $u \in L^2(0, T; H_0^1((0, \ell))) \cap C([0, T]; H_0^1((0, \ell)))$ in the distributional sense which satisfies (3), and*

$$\|u\|_{L^2(0, T; H_0^1((0, \ell)))} \leq C(\|f\|_{L^2((0, \ell))} + \|\psi_0\|_{L^2((0, \ell))}).$$

Note that the boundary condition is satisfied since $u(\cdot, t) \in H_0^1((0, \ell))$ for $t \in (0, T)$. Moreover, the restriction $u(x, t_0)$ is well-defined for $0 \leq t_0 \leq T$, since $u \in C([0, T]; H_0^1((0, \ell)))$, so especially $u(x, T)$ is well-defined. We have thereby shown that the problems used in the iterative procedure given in the previous section are well-posed and the restriction of solutions are well-defined.

A Stopping Rule

The procedure proposed in this paper is a regularization method and it therefore works with inexact data. More precisely, consider the case when there is some error in ψ_T in (4), namely

$$\|\psi_T - \psi_T^\delta\|_{L^2((0, \ell))} \leq \delta, \tag{5}$$

with $\delta > 0$. The elements u_k^δ and f_k^δ , are obtained by using the procedure of Section “An Iterative Algorithm for Finding the Source Term” with data ψ_0 and ψ_T^δ .

Given the noise levels, we can use the discrepancy principle of [6], to obtain a stopping criterion for ceasing the iterations of Steps (ii) and (iii) of the iterative algorithm of Section “An Iterative Algorithm for Finding the Source Term”. This suggests choosing the stopping index $k = k(\delta, \gamma)$ as the smallest index for which

$$\|u_k^\delta(\cdot, T) - \psi_T^\delta\|_{L^2((0, \ell))} \approx \delta. \tag{6}$$

The Boundary Element Method (BEM)

By applying Green’s formula we can recast eq (1) in the integral form

$$\begin{aligned} \eta(x)u(x, t) &= \int_0^t \left[G(x, t, \xi, \tau) \frac{\partial u}{\partial n(\xi)}(\xi, \tau) - u(\xi, \tau) \frac{\partial G}{\partial n(\xi)}(x, t, \xi, \tau) \right]_{\xi=0}^{\xi=\ell} d\tau \\ &+ \int_0^\ell G(x, t, y, 0)u(y, 0) dy + \int_0^\ell f(y) \int_0^t G(x, t, \xi, \tau) d\tau dy, \end{aligned} \tag{7}$$

for $(x, t) \in [0, \ell] \times (0, T]$, where $\eta(0) = \eta(\ell) = 1/2$, $\eta(x) = 1$ for $x \in (0, \ell)$, n is the outward unit normal to the space boundary $\{0, \ell\} \times [0, T]$, i.e., $n(0) = -1$ and $n(\ell) = 1$, and G is the fundamental solution of the one-dimensional heat equation, namely,

$$G(x, t, y, \tau) = \frac{H(t - \tau)}{\sqrt{4\pi(t - \tau)}} e^{-(x-y)^2/(4(t-\tau))},$$

where H is the Heaviside function.

Then the BEM, see [7], based on the boundary integral eq (7) is employed for solving the direct well-posed problems at each iteration of the recursive algorithm described in Section “An Iterative Algorithm for Finding the Source Term”.

Numerical Results and Discussion

In this section, we present and discuss the numerical results obtained by the iterative algorithm proposed in Section “An Iterative Algorithm for Finding the Source Term” numerically implemented using recursively the BEM described in the previous section for a typically benchmark test example which has the analytical solution

$$u(x, t) = (2 - e^{-\pi^2 t}) \sin(\pi x) \quad \text{for } x \in [0, 1] \times [0, 1], \tag{8}$$

$$f(x) = 2\pi^2 \sin(\pi x) \quad \text{for } x \in [0, 1]. \tag{9}$$

This analytical solution satisfies eq (1) and generates the input data (2)–(4) as given by

$$u(0, t) = 0 = h_0(t), \quad u(1, t) = 0 = h_1(t) \quad \text{for } t \in [0, 1], \quad (10)$$

$$u(x, 0) = \psi_0(x) = \sin(\pi x), \quad u(x, 1) = \psi_T(x) = (2 - e^{-\pi^2}) \sin(\pi x) \quad \text{for } x \in [0, 1]. \quad (11)$$

A BEM discretisation with 40 constant boundary elements uniformly distributed on each of the boundaries $\{0\} \times [0, 1]$, $\{1\} \times [0, 1]$ and $[0, 1] \times \{0\}$ was found to be sufficiently large to ensure that any further increase in this discretisation did not significantly affect the accuracy of the numerical solution of the direct problem (1)–(3) if $f(x)$ was known. The supplementary condition (4) was imposed also at 40 internal nodes uniformly located on $[0, 1] \times \{1\}$. An arbitrary initial guess such as $f_0 = 0$ was chosen to initiate the iterative algorithm. The measured data ψ_T in (11) was perturbed by $p \in \{1, 3, 5\}\%$ random Gaussian noise with mean zero and standard deviation $\sigma = (2 - e^{-\pi^2})p$, such that

$$\|\psi_T - \psi_T^\delta\|_{L^2((0,1))} \leq \delta(p) = \begin{cases} 0.0079 & \text{for } p = 1\%, \\ 0.0240 & \text{for } p = 3\%, \\ 0.0402 & \text{for } p = 5\%, \end{cases} \quad (12)$$

in eq (5). According to the discrepancy principle stopping criterion (6) we cease the iterations of the algorithm at the iteration number $k(p, \delta)$ given in Table 1. The corresponding errors in predicting the heat source i.e.

$$e(k) = \|u_k^\delta(\cdot, T) - \psi_T^\delta\|_{L^2((0,1))} \quad \text{and} \quad E(k) = \|f_k^\delta(\cdot, T) - f\|_{L^2((0,1))}, \quad (13)$$

are tabulated in Table 2.

$\begin{array}{c} p \\ \gamma \end{array}$	1%	3%	5%
1	648	539	482
2	323	268	240
3	214	178	159
10	62	52	46
100	2	2	2

Table 1. The stopping iteration given by (6), with δ given by (12).

$\begin{array}{c} p \\ \gamma \end{array}$	1%	3%	5%
1	0.0375	0.1149	0.1962
2	0.0372	0.1149	0.1956
3	0.0371	0.1144	0.1948
10	0.0366	0.1109	0.1941
100	0.0242	0.0615	0.0989

Table 2. The values of the errors $E(k)$ in predicting the heat source at the iteration number k given in Table 1.

The algorithm was found convergent for values of γ up to 200 after which the algorithm diverged. As expected, as δ increases, the attainability of the stopping criterion (6) becomes faster. These values can also be inferred from Fig. 1 which shows the errors $e(k)$ and $E(k)$ as a function of the number of iterations k for various amounts of noise $p \in \{1, 3, 5\}\%$ obtained for $\gamma = 1$. From this figure it can be seen that the error $e(k)$ decreases as k increases but the error $E(k)$ starts increasing once

$$k > \begin{cases} 795 & \text{for } p = 1, \\ 706 & \text{for } p = 3, \\ 662 & \text{for } p = 5. \end{cases} \quad (14)$$

Then based on (6) with δ given by (12), one obtains the values given in Table 1 above for $\gamma = 1$. Figure 2 shows the numerical solution for the source $f_k^\delta(x)$ at the discrepancy principle iteration k given in Table 1 for $\gamma = 1$, for various percentages of noise $p \in \{1, 3, 5\}\%$ in comparison with the exact solution (9). From Fig. 2 it can be seen that, as the amount of noise p decreases, the numerical solution approximates better the exact solution (9). Finally, we note that in the post-processing, from eq (7), we also obtain the numerical solution for the heat flux of $q_k = \partial_n u_k$ at the boundaries $\{0\} \times [0, 1]$ and $\{1\} \times [0, 1]$ and the interior solution $u_k(x, t)$.

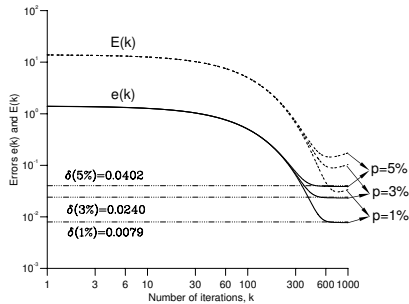


Figure 1. The errors e_k (—) and $E(k)$ (---) given by (13), as functions of the number of iterations k , for various amounts of noise $p \in \{1, 3, 5\}\%$ when $\gamma = 1$. The values of δ given by (12) are also shown (- · · · · -).

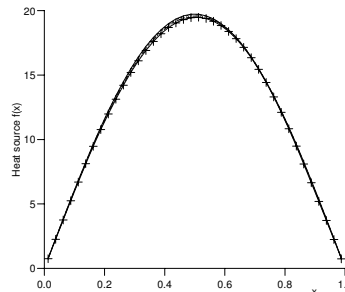


Figure 2. The analytical solution (9) (—) and the numerical solutions for the heat source, for various amounts of noise $p = 1\%$ (---), $p = 3\%$ (- · · · · -) and $p = 5\%$ (- + -), when $\gamma = 1$.

Acknowledgement

T. Johansson would like to acknowledge the grant and financial support from the Wenner-Gren foundations. Both authors would like to thank L. Elliott, A. Farcas and D. B. Ingham for their useful comments on this work.

References

[1] J. R. Cannon *SIAM Journal on Numerical Analysis*, **5**, 275–286 (1968).
 [2] A. I. Prilepko and V. V. Solov’ev *Differential Equations*, **23**, 1341–1349 (1988).
 [3] V. V. Solov’ev *Differential Equations*, **25**, 1114–1119 (1990).
 [4] W. Rundell *Applicable Analysis*, **10**, 231–242 (1980).
 [5] J.-L. Lions and E. Magenes *Non-homogeneous Boundary Value Problems and Applications*, Vol. I, Springer-Verlag (1972).
 [6] V. A. Morozov *Dokl. Akad. Nauk SSSR*, **167**, 510–512 (1966). English transl.: *Soviet Mathematics Doklady*, **7**, 414–417 (1966).
 [7] A. Farcas and D. Lesnic *Journal of Engineering Mathematics*, (2006), (in press).

Unsteady Panel Method for Oscillating Foils

Marco La Mantia¹ and Peter Dabnichki²

¹ Department of Engineering, Queen Mary, University of London, Mile End Road, London, E1 4NS, UK, m.lamantia@qmul.ac.uk

² Department of Engineering, Queen Mary, University of London, Mile End Road, London, E1 4NS, UK, p.dabnichki@qmul.ac.uk

Keywords: panel method, unsteady flows, flapping foils.

Abstract. The study is the first step in a wider investigation of biomimetic systems. A computer program based on a potential flow panel method was devised to evaluate the forces acting on a harmonically heaving and pitching two-dimensional rigid foil. A comparison with existing experimental data has been carried out and the initial results are encouraging but show the need of introducing inertia related effects. There was a very good agreement in the low range of the Strouhal number ($St \leq 0.25$) followed by sharp divergence in the higher range.

Introduction

Over millions of years in a vast and often hostile realm birds and fish have inevitably produced rather refined means of generating fast movement at low energy cost. Their flying and swimming capabilities are also far superior in many ways to those have been achieved by current science and technology. Aquatic and avian species instinctively use their streamlined bodies to exploit fluid mechanics principles, achieving high propulsive efficiency and manoeuvrability [1]. The idea of utilizing the thrust generated by flapping wings for the propulsion of man-made objects emerged from the observations of birds and fish behaviour. A number of theoretical and experimental studies [2,3,4,5] were performed over the past decades about this subject. The complex and multi-disciplinary character of the problem was underlined and key areas of interest identified, e.g. the effects of flow unsteadiness, wing flexibility and three-dimensionality. In any case, these issues have not been adequately investigated. Moreover, the existing studies focused either on aquatic or avian species. There have not been any published studies on biomimetic vehicles capable of both flying and submerging in water, i.e. machines able to fly in water. For example, the penguins, which are very special birds, have lost their ability to fly in the air but are capable of flying in the water faster than most fish swim. The possible technology exploitation of the penguins' swimming behaviour appears especially convenient for the development of a vehicle flying in water or another medium denser than air, e.g. an atmosphere denser than the terrestrial one. Such hybrid machine should be also able to change appropriately its shape and adapt itself autonomously to the variable environmental conditions. In others words, it could be called a smart structure.

The paper presents the first step of a project that focuses on a theoretical and computational analysis of a feasible design for a hybrid wing, i.e. for the flexible and flapping wing of a vehicle that could fly and submerge in water. In particular, a potential flow based panel method code was developed to study the unsteady motion of a two-dimensional rigid foil and the main aim is to compare the numerical results with existing experimental data [6,7].

Computational Method

An unsteady panel method program was developed to estimate the forces acting on a harmonically heaving and pitching two-dimensional rigid foil. A NACA 0012 symmetric foil was used according to [6,7]. For a foil of chord c , moving forward at an average, steady velocity Q , oscillating harmonically with a linear (heave) motion $z(t)$ transversely to the velocity Q and with an angular (pitch) motion $\gamma(t)$, which is also the instantaneous angle between Q and the chord, the following kinematic equations hold

$$z(t) = z_0 \sin(\omega t) \quad (1)$$

$$\gamma(t) = \gamma_0 \sin(\omega t + \psi) \quad (2)$$

where ψ is the phase angle between heave and pitch motions, z_0 the heave amplitude, γ_0 the pitch amplitude and ω the frequency of oscillation (in radians over second). The pitch axis was set at one third of the foil chord. The instantaneous angle of attack $\alpha(t)$ is defined as

$$\alpha(t) = \gamma(t) - \text{atan} \left(\frac{\dot{z}(t)}{Q} \right) \quad (3)$$

where $\dot{z}(t)$ is the time derivative of $z(t)$, i.e. the heave velocity.

The initial parameters of the above system are the heave amplitude z_0 , Strouhal number St , maximum angle of attack α_{max} and phase angle between heave and pitch ψ . The heave amplitude was set equal to three quarter of the foil chord. The Strouhal number indicates how often vortices are created in the foil's wake and how close they are: it is the product of the frequency of vortex formation behind the foil (in Hz) and the width of the wake (which is assumed equal to two times the heave amplitude), divided by the mean speed of the flow, i.e.

$$St = \frac{z_0 \omega}{\pi Q} \quad (4)$$

If Q , z_0 and St are fixed, it is then possible to compute the frequency of oscillation ω . Besides, the instantaneous angle of attack has not a simple relation to the so defined initial data. In general, for each Strouhal number St , when the maximum of the angle of attack α_{max} is fixed, there are two possible γ_0 , i.e. two possible angle of attack time paths: one corresponding to drag production and the other to thrust generation. The phase difference between the heaving and pitching motions ψ was assumed equal to 90 degrees, which corresponds to the optimum propulsion, as reported in [6,7]. For a visual explanation of foil motion kinematic parameters see Fig. 1 and 2.

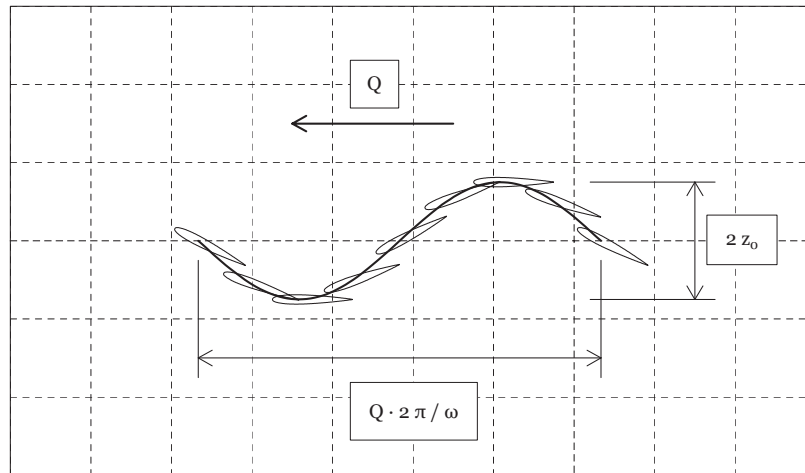


Fig. 1. Kinematic parameters of the foil motion: $c=0.1$ m, $Q=0.4$ m/s, $z_0=0.075$ m, $St=0.3$, $\psi=90$ deg, $\alpha_{max}=15$ deg, $\gamma_0=28.304$ deg (thrust generation) and $\omega=5.027$ rad/s.

According to [8], the foil is approximated by a finite number of panels N . A constant strength source σ and doublet μ are posed at the midpoint of each panel, which is also called panel's collocation point. A Dirichlet boundary condition is imposed, meaning that a potential function is specified inside the foil in order to meet

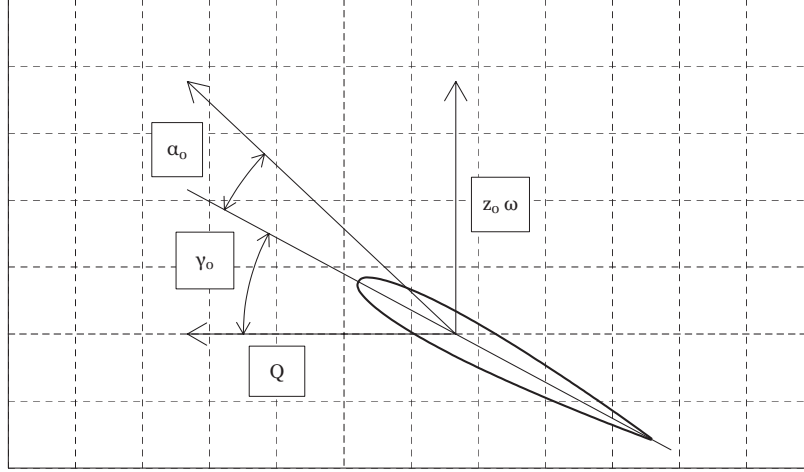


Fig. 2. The pitch amplitude γ_0 is assumed positive and the initial angle of attack α_0 is then negative and equal to -15° , if the other initial motion parameters are the same used in Fig. 1.

the zero normal flow condition. At each foil's collocation point the source strength is known, $\sigma = \bar{n} Q_k$, where \bar{n} is a unit vector normal to the foil's surface pointing into the body and Q_k is the fluid's kinematic velocity due to the motion of the foil. The governing integral equation was derived by using Laplace's equation and Green's third identity. In the body-fixed coordinate system, at time t , for each foil's collocation point it can be written as

$$\frac{1}{2\pi} \int_S [\sigma \ln r - \mu \frac{\partial}{\partial n} (\ln r)] dS - \frac{1}{2\pi} \int_{S_w} [\mu_w \frac{\partial}{\partial n} (\ln r)] dS_w = 0 \quad (5)$$

where S and S_w indicate the foil's and wake's surfaces, respectively. The discretized form of eq (5) is

$$\sum_{j=1}^N C_j \mu_j + \sum_{l=1}^M C_l \mu_{w1} + \sum_{j=1}^N B_j \sigma_j = 0 \quad (6)$$

where

$$C_j = -\frac{1}{2\pi} \int_{S_j} \frac{\partial}{\partial n} (\ln r) dS_j \quad (7)$$

and

$$B_j = \frac{1}{2\pi} \int_{S_j} \ln r dS_j \quad (8)$$

are the appropriate two-dimensional doublet and source influence coefficients of panel j at the considered collocation point, respectively. They are only dependent on the foil geometry, where r is the distance between the panel j and the respective collocation point and S_j is the length of panel j . M indicates the number of wake panels at time t , each with a constant strength doublet μ_w placed at the panel midpoint. At

each time step a new wake panel is added and its contribution evaluated. An unsteady Kutta condition, necessary to obtain a unique solution, is imposed at the foil trailing edge, at each time step, i.e.

$$(\mu_l - \mu_u + \mu_w)_t = 0 \quad (9)$$

where μ_l and μ_u are respectively the lower and upper surface doublet strengths at the foil trailing edge. The unknowns are then $N+1$, as the equations, since at time t the doublet strengths of the previously shed wake panels are already known. Besides, the wake influence coefficients C_l , which are defined as C_j and are only related to the foil and wake geometries, have to be calculated at each time step because the position of the shed wake panels changes with time. Moreover, at the first time step, the second addendum of eq (6) is null, i.e. the linear system is the same of the steady case.

The code is able to evaluate the flow potential function, which is related to μ , at each time step. It is then possible to calculate the velocities distribution over the foil in the body-fixed coordinate system, which is moving together with the foil. The calculation of the accelerations in the inertia frame of reference is the following step. Besides, the mass of the wing used in the experiments had to be estimated. According to [6,7], a 0.6 m wing span s and a 300 kg/m^3 wing average density (which is the wood mean density) were assumed. The calculated wing mass was then 0.15 kg. The foil wake had also to be carefully modelled. Since the foil is moving, the position of the wake collocation points in the body-fixed coordinate system has to be calculated at each time step starting from their position in the inertia frame of reference. In other words, it was imposed that the wake follows the foil's path.

Preliminary Results

The results attained to date are promising even though they are still not sufficiently close to the experimental ones. In Fig. 3 the instantaneous forces due to the foil motion, in the x and z directions of the inertia coordinate system (F_x and F_z) are shown as a function of the time t . In this case, if F_x is negative, there is thrust and, if F_z is positive, there is lift. It should be noted that, over one cycle, the maximum thrust is larger than the maximum drag. One thousand and two hundred time steps were generally used for the calculation, i.e. ten complete oscillations and one hundred and twenty time steps for each loop were performed.

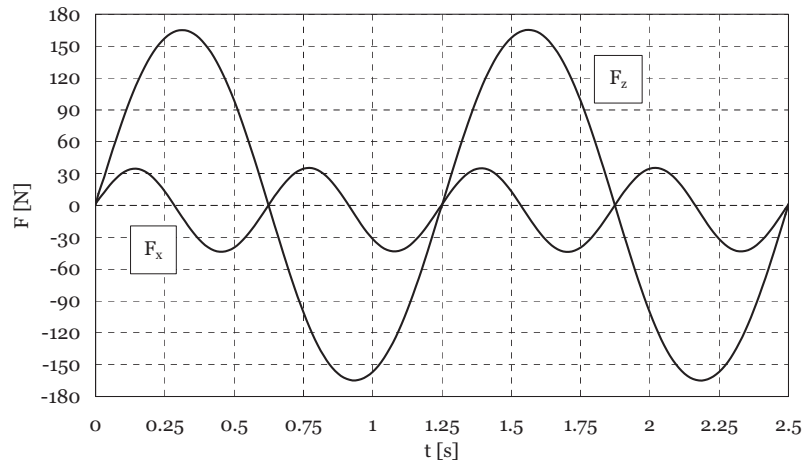


Fig. 3. The instantaneous forces F_x and F_z in the inertia coordinate system over two periods, i.e. from $t=0$ to $t=4\pi/\omega$ s. The motion parameters are the same used in Fig. 1 and 2.

In Fig. 4 a comparison with existing experimental data is displayed. The force coefficient in the x direction (CF_x) is plotted as a function of the Strouhal number St . CF_x is set to

$$CF_x = \frac{-\bar{F}_x}{\frac{1}{2}\rho c s Q^2} \tag{10}$$

where \bar{F}_x is the time-averaged force in the x direction of the inertia frame of reference and ρ is the water density (1000 kg/m^3). In this case, CF_x positive means thrust. For example, if $St=0.3$ and $N=200$, then CF_x equals to 0.93, which is larger than the values found in [6,7]. The computational curve trend is also steeper than the experimental ones. However, the force coefficient in the z direction is always close to zero, as expected.

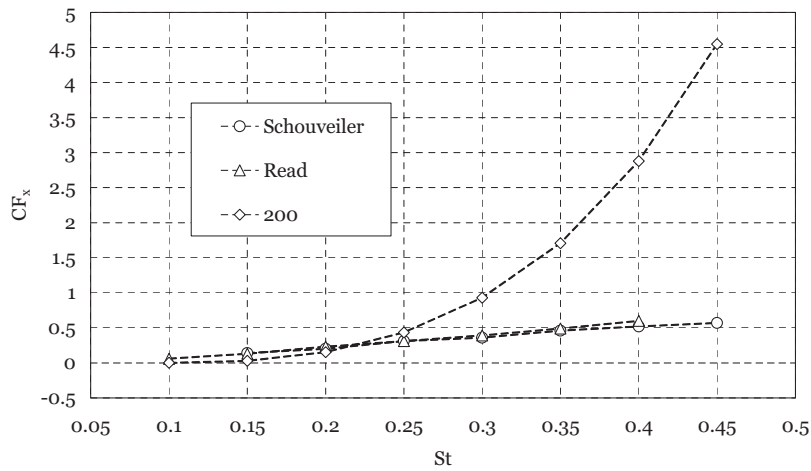


Fig. 4. ‘Read’ and ‘Schouveiler’ labels indicate the experimental data, from [6] and [7], respectively, and ‘200’ the computational results (200 denotes N). The motion parameters are $c=0.1 \text{ m}$, $s=0.6 \text{ m}$, $Q=0.4 \text{ m/s}$, $z_0=0.075 \text{ m}$, $\psi=90 \text{ deg}$ and $\alpha_{max}=15 \text{ deg}$.

Moreover, the considerable influence of the number of panels N on the results indicates that the developed code is still not stable: in the three central columns of Table 1 some computed values of CF_x are presented as a function of N (see the tags on the second row) and St (see the first column). The experimental data, as reported in [6] and [7], respectively, are displayed in the two last columns for comparison.

St	γ_0 [deg]	CF_x				
		100	200	400	Read	Schouveiler
0.20	17.14	0.08	0.15	0.24	0.23	0.20
0.30	28.30	0.47	0.93	1.46	0.39	0.36
0.40	37.74	1.45	2.88	4.55	0.60	0.52

Table 1. The influence of the number of the panels N on the force coefficient CF_x is shown as a function of the Strouhal number St . The displayed values of γ_0 correspond to thrust generation.

Conclusions and Future Work

The preliminary results of a potential flow panel method program able to evaluate the forces acting on a harmonically heaving and pitching two-dimensional rigid foil has been briefly presented together with a comparison with existing experimental data. They indicate that the developed code is still not stable and has to be improved in order to obtain more realistic results. The large influence of the number of panels on the computational results has especially to be better analyzed and then reduced. Moreover, since in the potential formulation the flow is assumed inviscid, incompressible and irrotational, the introduction of inertia related effects seems to be a suitable option to better represent the experimental conditions. In other words, as a first step, it is planned to evaluate the effect of the added mass (i.e. the mass of the fluid moving with the body while the body is in motion) because it could have a significant impact on the calculation of the forces. The movement of the surrounding water requires in fact an additional force over and above that necessary to accelerate the wing itself. The influence of the wake modelling and the NACA 0012 non-zero thickness trailing edge have also to be carefully investigated.

There is then the intention of estimating the forces acting on diverse foils, e.g. those that Bannasch [9] indicated as similar to penguins' flippers profiles. As a further step, the chordwise flexibility of the foil will be introduced in the program. Another, more distant aim is to obtain a three-dimensional version of the code.

References

- [1] M.S. Triantafyllou and G.S. Triantafyllou, G. S., *An Efficient Swimming Machine*, *Scientific American*, 272 (3), 64-70 (1995).
- [2] K.V. Rozhdestvensky and V.A. Ryzhov, *Aerohydrodynamics of Flapping-Wing Propulsors*, *Progress in Aerospace Science*, 39 (8), 585-633 (2003).
- [3] M.S. Triantafyllou, A.H. Techet and F.S. Hover, *Review of Experimental Work in Biomimetic Foils*, *IEEE Journal of Oceanic Engineering*, 29 (3), 585-594 (2004).
- [4] C.P. Ellington, *The Aerodynamics of Hovering Insect Flight*, *Philosophical Transactions of the Royal Society of London - Series B: Biological Sciences*, 305 (1122), 1-181 (1984).
- [5] S. Sunada and C.P. Ellington, *A New Method for Explaining the Generation of Aerodynamic Forces in Flapping Flight*, *Mathematical Methods in the Applied Sciences*, 24 (17-18), 1377-1386 (2001).
- [6] D.A. Read, F.S. Hover and M.S. Triantafyllou, *Forces on Oscillating Foils for Propulsion and Maneuvering*, *Journal of Fluids and Structures*, 17 (1), 163-183 (2003).
- [7] L. Schouveiler, F.S. Hover and M.S. Triantafyllou, *Performance of Flapping Foil Propulsion*, *Journal of Fluids and Structures*, 20 (7), 949-959 (2005).
- [8] J. Katz and A. Plotkin, *Low-Speed Aerodynamics – Second Edition*, Cambridge University Press (2001)
- [9] R. Bannasch, *Hydrodynamics of Penguins – An Experimental Approach*, in P. Dann, I. Norman and P. Reilly (Edited by), *The Penguins: Ecology and Management*, Surrey Beatty & Sons, 141-176 (1995)

Improving Secondary Recovery of an Oil Reservoir Using Hot Water

M. N. Mohamad Ibrahim¹ and S. Shuib²

¹School of Chemical Sciences, Universiti Sains Malaysia,
11800 Pulau Pinang, Malaysia, mnm@usm.my

²School of Mechanical Engineering, USM Engineering Campus, Universiti Sains Malaysia,
14300 Nibong Tebal, Pulau Pinang, Malaysia

Keywords: waterflooding; oil reservoir; oil viscosity; Taguchi method; productivity performance

Abstract. Waterflooding by far is the most dominant secondary recovery technique for an oil reservoir, which unable to produce through natural drive mechanisms. Its popularity is partly due to water ability in displacing the remaining oil and the general availability of water. Besides, injection of water into the system will help to maintain the reservoir pressure, as the productivity (flow rate) of a well in the presence of other wells is a function of the prevailing reservoir pressure. This paper try to investigate other factors that one should consider such as the effect of water temperature on its ability to displace oil. In this study, in addition to the reservoir pressure, other factors which are reservoir rock permeability, reservoir oil viscosity and the area of the reservoir will also be considered. A custom made Oil Reservoir Simulator based on BEM was used to obtain the flow rate of each individual well under study. Taguchi method, one of the most popular designs of experiment techniques, was used to rank factors (reservoir pressure, permeability, viscosity and area) that affect the flow rates of the wells. Numerical values obtained from the BEM analysis will be used as input data for the Taguchi statistical analysis. Results indicated that oil viscosity is the most important factor that affects the productivity performance of the oil well followed by the reservoir pressure, the rock permeability and area of the reservoir. Therefore, waterflooding project can be improved if hot water is used as the hot water helps reduces the oil viscosity and the same time maintain the reservoir pressure.

Taguchi Method

In this study, Taguchi Robust Design Technique (TRDT) was used to rank factors that may affect the productivity of oil reservoir. The use of Taguchi orthogonal array helps to determine the minimum number of simulation runs needed to produce the most favorable output for a given set of factors. These factors are rock permeability, reservoir oil viscosity, reservoir pressure and area of the reservoir. The comparison between full factorial design and Taguchi design is shown in Table 1. The orthogonal array L₉ was used to study the influence of these four factors. Each factor was considered at three levels. The factors involved and their levels are shown in Table 2. If full factorial experimental design were used, it would require 81 (3⁴) trials runs for all possible combinations of these factors to get the optimum result [1]. By using the Taguchi orthogonal array L₉ for experimental design, the number of trials runs was reduced to 9 simple and effective experiments.

Factors	Level	Total number of experiments	
		Factorial design	Taguchi design
2	2	4 (2^2)	4
3	2	8 (2^3)	4
4	2	16 (2^4)	8
7	2	128 (2^7)	8
15	2	32,768 (2^{15})	16
4	3	81 (3^4)	9

Table 1 : Comparisons of factorial design and Taguchi design

Column	Factors	Level Number		
		1	2	3
1	Permeability (md)	50	100	150
2	Viscosity (cp)	0.5	1.0	1.5
3	Reservoir Pressure (psi)	1,000	2,000	3,000
4	Reservoir Area (acre)	10	15	20

Table 2 : Design factors and their levels for orthogonal experiment

Table 3 illustrates the orthogonal array L_9 [1]. Since there were four of three levels factors, these factors were assigned to all four columns in the L_9 array. For example in trial number 1, the value for rock permeability, oil viscosity, reservoir pressure and reservoir area is 50 md, 0.5 cp, 1,000 psi and 10 acre respectively. For trial number 2, the value for permeability, viscosity, reservoir pressure and reservoir area is 100 md, 1.0 cp, 2,000 psi and 15 acre respectively. Nine trials simulation runs using the Boundary Element Oil Reservoir Simulation software with particular combination of factors levels in the array were carried out [2, 3, 4].

Trial Number	Column Number			
	1	2	3	4
1	1	1	1	1
2	1	2	2	2
3	1	3	3	3
4	2	1	2	3
5	2	2	3	1
6	2	3	1	2
7	3	1	3	2
8	3	2	1	3
9	3	3	2	1

Table 3 : L_9 (3^4) Orthogonal Array [1]

Results and Discussion

The results of the nine trial conditions are shown in Table 4. These simulation results are for the case of the following circular oil reservoir with single production well having the following properties:

$r_w = 0.25$ feet (well-bore radius),
 $\Phi = 15\%$ (porosity),
 $\rho = 62.4$ lb/ft³ (reservoir fluid density),
 $p_w = 100$ psi (well-bore pressure),
 $h = 35$ feet (reservoir thickness) and,
 $Scale = 1: 5,000$

In the Taguchi analysis, there are three of quality characteristics with respect to the target design, namely “smaller is better” and “bigger is better” [1]. In this study, the high value of oil production is desirable, therefore the “bigger is better” quality characteristic was chosen.

Trial Number	Total Oil Production in barrel per day (bbl/d)
1	2,105.9
2	2,222.9
3	2,261.9
4	8,891.5
5	6,785.6
6	1,403.9
7	20,356.9
8	3,158.8
9	4,445.8
Grand Average	5,737.02

Table 4 : Simulation results

Different factors affect the wells productivities to different degrees. The relative effect of the different factors can be obtained by the decomposition of total variation into its appropriate components, which is commonly called analysis of variance (ANOVA). ANOVA is also needed for estimating the error variance. The results of ANOVA are shown in Table 5. Data generated in Table 5 especially the Sum of Squares, Variance and Percent were obtained from TRDT educational software, Qualitek-4 [5].

Column	Factors	DOF	Sum of Squares	Variance	F	Percent
1	Permeability (md)	2	76126966.421	38063483.21	-	26.296
2	Viscosity (cp)	2	102756985.448	51378492.724	-	35.495
3	Reservoir Pressure (psi)	2	87515453.336	43757726.668	-	30.23
4	Reservoir Area (area)	2	23092672.93	11546336.465	-	7.976
All others/error		0	0			0
Total		8	289492096.277			100.00 %

Table 5 : ANOVA table

The review of the 'Percent' column in Table 5 showed that the oil viscosity factor contributed the highest percentage (35.5%) to the factor effects; followed by the reservoir pressure (30.2%), rock permeability (26.3%) and area of the reservoir (8.0%). Since the contribution of area of the reservoir was the smallest and less than 10% therefore it was considered insignificant. Thus, this factor was pooled (combined) with the error term. This process of disregarding the contribution of a selected factor and subsequently adjusting the contribution of the other factor is known as pooling. The new ANOVA after pooling is shown in Table 6. It was observed that as the smallest factor effect (reservoir area) was pooled, the percentage contributions of the remaining factors decreased slightly, but the ranking of factor effects still remained the same. In estimating the performance at optimum condition, only the significant factors were used. An examination of the average effects as shown in Table 7 indicates that level 1 of viscosity and level 3 of both permeability and pressure factors will be included in the optimum condition (after excluding area of the reservoir factor). This is due to the highest value of average effects for each factor. With this levels combination, one should get the total oil production as 20,357 bbl/d.

Column	Factors	DOF	Sum of Squares	Variance	F	Percent
1	Permeability (md)	2	76126966.421	38063483.21	3.296	18.319
2	Viscosity (cp)	2	102756985.448	51378492.724	4.449	27.518
3	Reservoir Pressure (psi)	2	87515453.336	43757726.668	3.789	22.253
4	Area Reservoir (acre)	(2)	(23092672.93)		POOLED	
All others/Error		2	23092691.07	11546345.535		31.91
Total		8				100.00 %

Table 6 : Pooled ANOVA table

Column	Factors	Level Number		
		1	2	3
1	Permeability (md)	2196.899	5693.666	9320.5
2	Viscosity (cp)	10451.433	4055.766	2703.866
3	Reservoir Pressure (psi)	2222.866	5186.733	9801.466
4	Reservoir Area (acre)	4445.766	7994.566	4770.733

Table 7 : The Average Effects of Factor for Each Level

Most data generated in Table 6 and Table 7 especially were obtained from TRDT educational software, Qualitek-4 [5]

Conclusions

Among four factors considered in this study, reservoir oil viscosity found to be the most influenced factor in producing oil from the reservoir. It's followed by the reservoir pressure, rock permeability and area of the reservoir. Designing an Enhance Oil Recovery technique that can improve the oil viscosity such as hot waterflooding/steam flooding would be a good idea in order to improve the productivity of the reservoir. Less viscous oil is easier to be displaced compared to more viscous fluid.

Further analysis shows that (by keeping the viscosity, reservoir pressure and rock permeability at their optimum levels), regardless of any area of the reservoir value used in the simulation runs, the oil productivity values are still the same. This proves that area reservoir has very small contribution towards the productivity of the reservoir.

Acknowledgements

The authors would like to express their appreciation to Universiti Sains Malaysia for financial support of this project through a research grant. The first author also would like to thank his beloved wife, Azah and his two princes Mohamad Aiman Hamzah and Ahmad Zaid for their supports, sacrifices and patience throughout this project.

References

- [1] R. K. Roy *A Primer on the Taguchi Method*, Van Nostrand Reinhold, New York, (1990).
- [2] M. N. Mohamad Ibrahim and D. T. Numbere *Boundary Element Analysis of The Productivity Of Complex Petroleum Well Configuration*, In C. S. Chen, C. A. Brebbia and D. Pepper (Eds), *Boundary Element Technology XIII*, WIT Press, Southampton, 25-34, (1999).
- [3] M. N. Mohamad Ibrahim and D. T. Numbere *Productivity Predictions for Oil Well Clusters Using A Boundary Element Method*, *J. of Physical Science*, Vol.11, 148-157, (2000).
- [4] M. N. Mohamad Ibrahim and D. T. Numbere *Boundary Shape Effects On the Productivity of Oil Well Clusters*, In *Boundary Element Technology XIV*, A. Kassab and C. A. Brebbia (Eds), WIT Press, Southampton, 293-299, (2001).
- [5] R. K. Roy *Design of Experiments Using the Taguchi Approach*, John Wiley and Sons Inc., New York, (2001).

Three-Dimensional Elastoplastic Analysis by Triple-Reciprocity Boundary Element Method

Yoshihiro OCHIAI¹

¹ Department of Mechanical Engineering, Kinki University, 3-4-1 Kowakae, Higashi-Osaka, 577-8502, Japan, Email: ochiai@mech.kindai.ac.jp

Key Words: Elastoplastic problem; Initial strain method; BEM

Abstract. In general, internal cells are required to solve elastoplastic problems using a conventional boundary element method (BEM). However, in this case, the merit of BEM, which is ease of data preparation, is lost. Triple-reciprocity BEM can be used to solve two-dimensional elastoplasticity problems with a small plastic deformation. In this study, it is shown that three-dimensional elastoplastic problems can be solved, without the use of internal cells, by the triple-reciprocity BEM. An initial strain formulation is adopted and the initial strain distribution is interpolated using boundary integral equations. A new computer program was developed and applied to solving several problems.

1. Introduction

The finite element method (FEM) requires several repetition of remeshing for large-plastic-deformation analysis. Elastoplastic problems can be solved by a conventional boundary element method (BEM) using internal cells for domain integrals [1, 2]. In this case, however, the merit of BEM, which is ease of data preparation, is lost. On the other hand, several countermeasures have been considered. Ochiai and Kobayashi proposed the triple-reciprocity BEM without the use of internal cells for elastoplastic problems [3]. By this method, a highly accurate solution can be obtained using only fundamental solutions of a low order and by diminishing the need for data preparation. Ochiai and Kobayashi applied the triple-reciprocity BEM (improved multiple-reciprocity BEM) without internal cells to two-dimensional elastoplastic problems using an initial stress and strain formulations [3,4].

In this study, triple-reciprocity BEM is applied to three-dimensional elastoplastic problems. The initial strain formulation is adopted and the theory is expressed using a few fundamental solutions. In this method, only boundary elements are used. The arbitrary distributions of the initial strain for elastoplastic analysis are interpolated using boundary integral equations and internal points. This interpolation corresponds to a thin plate spline. In this method, strong singularities in the calculation of stresses at internal points become weak. A new computer program was developed and applied to several elastoplastic problems to clearly understand the theory.

2. Theory

2.1 Initial strain formulation To analyze the elastoplastic problems using the initial strain formulation, the following boundary integral equation must be solved [1,2].

$$c_{ij}(P, Q) \dot{u}_j(P) = \int_{\Gamma} [u_{ij}^{[1]}(P, Q) \dot{p}_j(Q) - p_{ij}(P, Q) \dot{u}_j(Q)] d\Gamma + \int_{\Omega} \sigma_{jki}^{[1]}(P, q) \dot{\varepsilon}_{ijk}^{[1]}(q) d\Omega \quad (1)$$

Here, $\dot{\varepsilon}_{ijk}^{[1]}$ is the initial strain rate and c_{ij} is the free coefficient. Moreover, u_j and p_j are the j -th components of the displacement rate and the surface traction rate, respectively. On the other hand, Γ and Ω are the boundary and the domain, respectively. As shown in eq (1), when there is an arbitrary initial strain rate, a domain integral becomes necessary. Denoting the distance between the observation point and the loading point by r , Kelvin's solution $u_{ij}^{[1]}$ and p_{ij} are given by

$$u_{ij}^{[1]} = \frac{1}{16\pi(1-\nu)Gr} \{ (3-4\nu)\delta_{ij} + r_{,i} r_{,j} \} \quad (2)$$

$$p_{ij} = \frac{1}{8\pi(1-\nu)Gr^2} \{ [(1-2\nu)\delta_{ij} + 3r_{,i} r_{,j}] \frac{\partial r}{\partial n} - (1-2\nu)(r_{,i} n_j - r_{,j} n_i) \} , \quad (3)$$

where ν is Poisson's ratio and G is the shear modulus. The i -th component of a unit normal vector is denoted by n_i . Moreover, let us set $r_{,i} = \partial r / \partial x_i$. The function $\sigma_{ijk}^{[1]}$ in eq (1) is given by [1]

$$\sigma^{[1]}_{jki} = \frac{-1}{8\pi(1-\nu)r^2} \{ (1-2\nu)(\delta_{ji}r_{,k} + \delta_{ki}r_{,j} - \delta_{jk}r_{,i}) + 3r_{,i}r_{,j}r_{,k} \} . \quad (4)$$

2.2 Interpolation of initial strain Interpolation using boundary integrals is introduced to avoid the domain integral in eq (1). The distribution of the initial strain $\dot{\epsilon}_{Ijk}^{[1]}$ in the case of a three-dimensional problem is interpolated using the integral equation to transform the domain integral into a boundary integral. The following equations are used for interpolation [5-8]:

$$\nabla^2 \dot{\epsilon}_{Ijk}^{[1]S} = -\dot{\epsilon}_{Ijk}^{[2]S} , \quad (5)$$

$$\nabla^2 \dot{\epsilon}_{Ijk}^{[2]S} = -\sum_{m=1}^M \dot{\epsilon}_{Ijk(m)}^{[3]PA} , \quad (6)$$

where $\nabla^2 = \partial^2 / \partial x^2 + \partial^2 / \partial y^2 + \partial^2 / \partial z^2$. From eqs (6) and (7), we obtain

$$\nabla^4 \dot{\epsilon}_{Ijk}^{[1]S} = \sum_{m=1}^M \dot{\epsilon}_{Ijk(m)}^{[3]PA} , \quad (7)$$

where the function $\dot{\epsilon}_{Ijk}^{[3]PA}$ expresses a state of a uniformly distributed polyharmonic function in a spherical region with radius A . We must emphasize that eqs (6) and (7) can be used for interpolating the complicated distribution of the initial strain $\dot{\epsilon}_{Ijk}^{[1]}$. These equations are the same as those used to generate a free-form surface using an integral equation [6]. In this method, each component of initial strain $\dot{\epsilon}_{Ijk}^{[1]}$ ($j, k=1,2,3$) is interpolated.

2.3 Representation of initial strain by integral equation The distribution of the initial strain is represented by an integral equation. The polyharmonic function $T^{[f]}$ and its normal derivatives are given by

$$T^{[f]} = \frac{r^{2f-3}}{4\pi(2f-2)!} \quad (8)$$

$$\frac{\partial T^{[f]}}{\partial n} = \frac{(2f-3)r^{2f-4}}{4\pi(2f-2)!} \frac{\partial r}{\partial n} \quad (9)$$

Figure 1 shows the shape of polyharmonic functions; the biharmonic function $T^{[2]}$ is not smooth at $r=0$. In the three-dimensional case, a smooth interpolation cannot be obtained using solely the biharmonic function $T^{[2]}$. In order to obtain a smooth interpolation, the polyharmonic function with volume distribution $T^{[2]A}$ is introduced. A polyharmonic function with volume distribution $T^{[f]A}$ is defined as [12]

$$T^{[f]A} = \int_0^A \left[\int_0^{2\pi} \left\{ \int_0^\pi T^{[f]} a^2 \sin \theta d\theta \right\} d\phi \right] da . \quad (10)$$

The function $T^{[f]A}$ can be easily obtained using the relationships $r^2 = R^2 + a^2 - 2aR \cos \theta$ and $dr = aR \sin \theta d\theta$. This function is written using r instead of R , similarly to eqs (8) and (9), though the function in eq (10) is a function of R . The newly defined function $T^{[f]A}$ can be explicitly shown as

$$T^{[f]A} = \frac{1}{2r(2f+1)!} \left\{ (2fA-r)(r+A)^{2f} + (2fA+r)(r-A)^{2f} \right\} \quad r > A \quad (11)$$

$$T^{[f]A} = \frac{1}{2r(2f+1)!} \left\{ (2fA-r)(A+r)^{2f} - (2fA+r)(A-r)^{2f} \right\} \quad r \leq A . \quad (12)$$

Denoting the number of points $\dot{\epsilon}_{Ijk}^{[3]P}$ as M , the curvature of the initial strain rate $\dot{\epsilon}_{Ijk}^{[2]S}$ is given by Green's second identity and eq (6) as [4-6]

$$c \dot{\epsilon}_{Ijk}^{[2]S}(P) = \int_{\Gamma} \left\{ T^{[1]}(P, Q) \frac{\partial \dot{\epsilon}_{Ijk}^{[2]S}(Q)}{\partial n} - \frac{\partial T^{[1]}(P, Q)}{\partial n} \dot{\epsilon}_{Ijk}^{[2]S}(Q) \right\} d\Gamma + \sum_{m=1}^M T^{[1]A}(P, q) \dot{\epsilon}_{Ijk(m)}^{[3]PA} . \quad (13)$$

The initial strain rate $\dot{\epsilon}_{ijk}^{[1]}$ is given by Green's theorem and eqs (5) and (6) as [4-6]

$$c\dot{\epsilon}_{ijk}^{[1]S}(P) = -\sum_{f=1}^2 (-1)^f \int_{\Gamma} \{T^{[f]}(P, Q) \frac{\partial \dot{\epsilon}_{ijk}^{[f]S}(Q)}{\partial n} - \frac{\partial T^{[f]}(P, Q)}{\partial n} \dot{\epsilon}_{ijk}^{[f]S}(Q)\} d\Gamma - \sum_{m=1}^M T^{[2]A}(P, q) \dot{\epsilon}_{ijk(m)}^{[3]PA}, \quad (14)$$

where $c=0.5$ on the smooth boundary and $c=1$ in the domain. It is assumed that $\dot{\epsilon}_{ijk}^{[2]S}(Q)$ is zero. For internal points, the next equation is obtained similarly to eq (14).

$$c\dot{\epsilon}_{ijk}^{[1]S}(p) = -\sum_{f=1}^2 (-1)^f \int_{\Gamma} \{T^{[f]}(p, Q) \frac{\partial \dot{\epsilon}_{ijk}^{[f]S}(Q)}{\partial n} - \frac{\partial T^{[f]}(p, Q)}{\partial n} \dot{\epsilon}_{ijk}^{[f]S}(Q)\} d\Gamma - \sum_{m=1}^M T^{[2]A}(p, q) \dot{\epsilon}_{ijk(m)}^{[3]PA}(q) \quad (15)$$

If the boundary is divided into N_0 constant elements, and N_1 internal points are used, the simultaneous linear algebraic equations with $(2N_0+N_1)$ as unknowns must be solved.

2.4 Triple-reciprocity boundary element method The function $\sigma_{jki}^{[f]}$ is defined as

$$\nabla^2 \sigma_{jki}^{[f+1]} = \sigma_{jki}^{[f]} \quad (16)$$

Using eqs (5), (6) and (16) and Green's second identity, eq (1) becomes

$$c_{ij}(P)\dot{u}_j(P) = \int_{\Gamma} [u_{ij}^{[1]}(P, Q)\dot{p}_j(Q) - p_{ij}(P, Q)\dot{u}_j(Q)] d\Gamma - \sum_{f=1}^2 (-1)^f \int_{\Gamma} \left\{ \frac{\partial \sigma_{jki}^{[f+1]}(P, Q)}{\partial n} \dot{\epsilon}_{ijk}^{[f]S}(Q) - \sigma_{jki}^{[f+1]}(P, Q) \frac{\partial \dot{\epsilon}_{ijk}^{[f]S}(Q)}{\partial n} \right\} d\Gamma + \sum_{m=1}^M \sigma_{jki}^{[3]A}(P, q) \dot{\epsilon}_{ijk(m)}^{[3]PA}(q). \quad (17)$$

$\sigma_{ijk}^{[f]}$ is obtained as [4]

$$\sigma_{ijk}^{[f]} = \frac{(2f-1)(2f-3)r^{2f-4}}{4\pi(1-\nu)(2f)!} \{ (2f-1-2f\nu)(\delta_{jk}r_{,i} + \delta_{ik}r_{,j}) - (1-2f\nu)\delta_{ij}r_{,k} - (2f-5)r_{,i}r_{,j}r_{,k} \}. \quad (18)$$

Moreover, the normal derivative $\partial\sigma_{ijk}^{[f]}/\partial n$ is given by

$$\begin{aligned} \frac{\partial \sigma_{ijk}^{[f]}}{\partial n} &= \frac{(2f-1)(2f-3)}{4\pi(1-\nu)(2f)!} r^{2f-5} [(2f-5)\{ (2f-1-2f\nu)(\delta_{jk}r_{,i} + \delta_{ik}r_{,j}) \\ &\quad - (1-2f\nu)\delta_{ij}r_{,k} - (2f-7)r_{,i}r_{,j}r_{,k} \}] \frac{\partial r}{\partial n} - (2f-5)(r_{,j}r_{,k}n_i + r_{,i}r_{,k}n_j + r_{,i}r_{,j}n_k) \\ &\quad + (2f-1-2f\nu)(\delta_{jk}n_i + \delta_{ik}n_j) - (1-2f\nu)\delta_{ij}n_k \end{aligned} \quad (19)$$

$$\begin{aligned} \sigma^{[3]A}_{ijk} &= \frac{A^3}{15120(1-\nu)r^4} \{ 18\nu\delta_{ij}r_{,k}r^2(35r^4 + 14A^2r^2 - A^4) \\ &\quad - (\delta_{jk}r_{,i} + \delta_{ik}r_{,j} + \delta_{ij}r_{,k})(105r^6 + 63A^2r^4 - 9A^4r^2 + A^6) - r_{,i}r_{,j}r_{,k}(105r^6 - 63A^2r^4 + 27A^4r^2 - 5A^6) \\ &\quad + 18(1-\nu)(\delta_{jk}r_{,i} + \delta_{ik}r_{,j})r^2(35r^4 + 14A^2r^2 - A^4) \} \quad r > A \end{aligned} \quad (20)$$

$$\begin{aligned} \sigma^{[3]A}_{ijk} &= \frac{r}{7560(1-\nu)} \{ 9\nu\delta_{ij}r_{,k}(-r^4 + 14A^2r^2 + 35A^4) - (\delta_{jk}r_{,i} + \delta_{ik}r_{,j} + \delta_{ij}r_{,k})(-r^4 + 18A^2r^2 + 63A^4) \\ &\quad - 4r_{,i}r_{,j}r_{,k}r^2(-r^2 + 9A^2) + 9(1-\nu)(\delta_{jk}r_{,i} + \delta_{ik}r_{,j})(-r^4 + 14A^2r^2 + 35A^4) \} \quad r \leq A. \end{aligned} \quad (21)$$

2.5 Internal stresses The internal stress is given by

$$\begin{aligned} \dot{\sigma}_{ij}(p) = & \int_{\Gamma} [-\sigma_{kij}^{[1]}(p, Q) \dot{p}_k(Q) - S_{kij}(p, Q) \dot{u}_k(Q)] d\Gamma \\ & - \sum_{f=1}^2 (-1)^f \int_{\Gamma} \left[\frac{\partial \sigma_{ijkl}^{[f+1]}(p, Q)}{\partial n} \dot{\varepsilon}_{ijkl}^{[f]S}(Q) - \sigma_{ijkl}^{[f+1]}(p, Q) \frac{\partial \dot{\varepsilon}_{ijkl}^{[f]S}(Q)}{\partial n} \right] d\Gamma \\ & + \sum_{m=1}^M \sigma_{ijkl}^{[3]A}(p, q) \dot{\varepsilon}_{ijkl(m)}^{[3]PA}(q) - \dot{\sigma}_{ij}^{[1]}(q). \end{aligned} \quad (22)$$

where

$$\begin{aligned} \sigma^{[f]ijkl} = & \frac{(2f-1)(2f-3)Gr^{2f-5}}{2\pi(1-\nu)(1-2\nu)(2f)!} < 2f\nu\{1+2(f-2)\nu\}\delta_{ij}\delta_{kl} + (1-2\nu)[(2f-1-2f\nu)(\delta_{ik}\delta_{jl} + \delta_{il}\delta_{jk}) \\ & + (2f-5)(f-1-f\nu)(\delta_{jl}r_{,i}r_{,k} + \delta_{jk}r_{,i}r_{,l} + \delta_{il}r_{,j}r_{,k} + \delta_{ik}r_{,j}r_{,l}) \\ & - (1-2f\nu)\{2(f-5)(\delta_{kl}r_{,i}r_{,j} + \delta_{ij}r_{,k}r_{,l}) + \delta_{ij}\delta_{kl}\} - (2f-5)(2f-7)r_{,i}r_{,j}r_{,k}r_{,l} > . \end{aligned} \quad (23)$$

$$\begin{aligned} \frac{\partial \sigma^{[f]ijkl}}{\partial n} = & \frac{(2f-1)(2f-3)(2f-5)G}{2\pi(1-\nu)(1-2\nu)(2f)!} r^{2f-6} \\ & \left[< 2f\nu\{1+2(f-2)\nu\}\delta_{ij}\delta_{kl} + (1-2\nu)[(2f-1-2f\nu)(\delta_{ik}\delta_{jl} + \delta_{il}\delta_{jk}) \right. \\ & + (2f-7)(f-1-f\nu)(\delta_{jl}r_{,i}r_{,k} + \delta_{jk}r_{,i}r_{,l} + \delta_{il}r_{,j}r_{,k} + \delta_{ik}r_{,j}r_{,l}) - (1-2f\nu)\{2(f-7)(\delta_{kl}r_{,i}r_{,j} \\ & + \delta_{ij}r_{,k}r_{,l}) + \delta_{ij}\delta_{kl}\} - (2f-7)(2f-9)r_{,i}r_{,j}r_{,k}r_{,l} > \frac{\partial r}{\partial n} + (1-2\nu) \left. \left[(f-1-f\nu)\{(\delta_{jl}n_k + \delta_{jk}n_l)r_{,i} \right. \right. \\ & + (\delta_{il}n_k + \delta_{ik}n_l)r_{,j} + (\delta_{jl}n_i + \delta_{il}n_j)r_{,k} + (\delta_{jk}n_i + \delta_{ik}n_j)r_{,l} \} \\ & - (1-2f\nu)\{(\delta_{ij}(r_{,i}n_k + r_{,k}n_l) + \delta_{kl}(r_{,j}n_i + r_{,i}n_j))\} \\ & \left. - (2f-7)\{(r_{,i}n_k + r_{,k}n_l)r_{,i}r_{,j} + (r_{,j}n_i + r_{,i}n_j)r_{,k}r_{,l}\} \right] \end{aligned} \quad (24)$$

$$\begin{aligned} \sigma^{[3]Aijkl} = & \frac{GA^3}{7560(1-\nu)(1-2\nu)r^5} \times [18\nu r^2 \delta_{kl} [28\nu^2 \delta_{ij} (5r^2 + A^2) + (1-2\nu)\{\delta_{ij}(35r^4 + 14A^2r^2 - A^4) \\ & + r_{,i}r_{,j}(35r^4 - 14A^2r^2 + 3A^4)\}] + (1-2\nu) \times [18\nu r^2 \delta_{ij} \{ \delta_{kl}(35r^4 + 14A^2r^2 - A^4) \\ & + r_{,k}r_{,l}(35r^4 - 14A^2r^2 + 3A^4) \} \\ & - (\delta_{ij}\delta_{kl} + \delta_{kj}\delta_{li} + \delta_{ki}\delta_{lj})(105r^6 + 63A^2r^4 - 9A^4r^2 + A^6) - (\delta_{ij}r_{,k}r_{,l} + \delta_{kj}r_{,i}r_{,l} + \delta_{ki}r_{,j}r_{,l} \\ & + \delta_{kl}r_{,i}r_{,j} + \delta_{il}r_{,k}r_{,j} + \delta_{jl}r_{,k}r_{,i})(105r^6 - 63A^2r^4 + 27A^4r^2 - 5A^6) \\ & - r_{,j}r_{,i}r_{,k}r_{,l}(-105r^6 + 189A^2r^4 - 135A^4r^2 + 35A^6) \\ & + 9(1-\nu)r^2\{2(\delta_{ki}\delta_{jl} + \delta_{kj}\delta_{il})(35r^4 + 14A^2r^2 - A^4) \\ & + (\delta_{ki}r_{,j}r_{,l} + \delta_{kj}r_{,i}r_{,l} + \delta_{il}r_{,j}r_{,k} + \delta_{ij}r_{,i}r_{,k})(35r^4 - 14A^2r^2 + 3A^4)\}] \quad r > A \end{aligned} \quad (25)$$

$$\begin{aligned} \sigma^{[3]Aijkl} = & \frac{G}{3780(1-\nu)(1-2\nu)} < 63\nu^2 \delta_{ij}\delta_{kl}(-r^4 + 10A^2r^2 + 15A^4) \\ & + (1-2\nu)[18\nu\{\delta_{ij}\delta_{kl}(-r^4 + 14A^2r^2 + 35A^4) + 2(\delta_{kl}r_{,i}r_{,j} + \delta_{ij}r_{,k}r_{,l})r^2(-r^2 + 7A^2)\} \\ & - (\delta_{ij}\delta_{kl} + \delta_{ik}\delta_{jl} + \delta_{il}\delta_{jk})(-r^4 + 18A^2r^2 + 63A^4) \\ & - 4(\delta_{kl}r_{,i}r_{,j} + \delta_{jl}r_{,i}r_{,k} + \delta_{jk}r_{,i}r_{,l} + \delta_{il}r_{,j}r_{,k} + \delta_{ik}r_{,j}r_{,l} + \delta_{ij}r_{,k}r_{,l}) \times r^2(-r^2 + 9A^2) \\ & + 8r_{,i}r_{,j}r_{,k}r_{,l}r^4 + 9(1-\nu)\{(\delta_{ik}\delta_{jl} + \delta_{ij}\delta_{jk})(-r^4 + 14A^2r^2 + 35A^4) \\ & + 2(\delta_{jl}r_{,i}r_{,k} + \delta_{jk}r_{,i}r_{,l} + \delta_{il}r_{,j}r_{,k} + \delta_{ik}r_{,j}r_{,l})r^2(-r^2 + 7A^2)\}] > \quad r \leq A \end{aligned} \quad (26)$$

2.6 Initial strain An iterative process is used for elastoplastic analysis. The load at first yield F_s is obtained. Denoting the final load as F_o and the number of iterations as N , incremental load $(F_o - F_s)/N$ is added gradually. It is assumed that σ_o^k corresponds to the uniaxial yield stress at load step k . The uniaxial

yield stress at the next load step $k+1$ is obtained by

$$\sigma_0^{k+1} = \sigma_0^k + H d\varepsilon_e^P \quad (27)$$

where H is strain hardening and $d\varepsilon_e^P$ is the equivalent plastic strain increment. The von Mises yield criterion is considered. The deviatoric stress tensor S_{ij} is obtained from the stress rate of eq (22), and the equivalent stress σ_e is calculated as follows:

$$\sigma_e = \sqrt{\frac{3}{2} S_{ij} S_{ij}} \quad (28)$$

The von Mises yield criterion can be defined as

$$\sigma_e - \sigma_0 = 0 \quad (29)$$

The plastic strain increment $d\varepsilon_{ij}^P$ is determined by using the following Prandtl-Reuss equation:

$$d\varepsilon_{ij}^P = S_{ij} d\lambda \quad (30)$$

where $d\lambda$ is a proportionality factor. Using eq (30), the provisional plastic strain increment $d\varepsilon_{ij}^P$ is calculated. Using the initial strain rate on the boundary and at internal points, the initial strain rate is interpolated using eqs (5) and (6). The displacement rate and traction rate are obtained by eq (17), and the strain rate is obtained by eq (22). The initial strain rate is converged by iterating the above process. Afterwards, the next load increment is added.

3. Numerical examples

In order to ensure the accuracy of the present method, the stress in a thick cylinder, which is made of an elastoplastic material, subjected to internal pressure is obtained. It is assumed that the inner and outer radii are 10 and 30 mm. The von Mises yield criterion is used, and the cylinder is restricted in the z direction. Young's modulus $E = 210$ GPa and Poisson's ratio $\nu = 0.30$ are assumed. Internal pressure $p_0 = 1.2$ GPa, yield stress $\sigma_y = 1.2$ GPa and strain hardening $H = 0.1E$ are assumed. The numbers of discretized boundary elements and internal points are 680 and 315, as shown in Fig. 1. Internal points are used to interpolate the distribution of initial strain. Figure 3 shows the circumferential and radial stress distributions. Boundary element results are shown with FEM solutions in Fig. 2. The stress distributions agree well with the FEM solutions.

4. Conclusion

It was shown that three-dimensional elastoplastic analysis can be carried out, without the use of internal cells, using the triple-reciprocity boundary element method. The fundamental solutions for this analysis were shown. In this method, the strong singularity that appears in the calculation of internal stress by the conventional boundary element method becomes weak. Using numerical examples, the effectiveness and accuracy of this method were demonstrated. In this method, the merit of BEM, which is ease of data preparation, is not lost because internal cells are not necessary.

References

- [1] Telles, J. C. F., The Boundary Element Method Applied to Inelastic Problems, Springer-Verlag, Berlin, 1983.
- [2] Brebbia, C. A., Telles, J. C. F. and Wrobel, L. C., Boundary Element Techniques-Theory and Applications in Engineering, Springer-Verlag, Berlin, pp. 252-266, 1984.
- [3] Ochiai, Y. and Kobayashi, T., Initial Stress Formulation for Elastoplastic Analysis by Improved Multiple-Reciprocity Boundary Element Method, Engineering Analysis with Boundary Elements, Vol. 23, pp. 167-173, 1999.
- [4] Ochiai, Y. and Kobayashi, T., Initial Strain Formulation without Internal Cells for Elastoplastic Analysis by Triple-Reciprocity BEM, International Journal for Numerical Methods in Engineering, Vol. 50, pp. 1877-1892, (2001).
- [5] Y. Ochiai and V. Sladek, Numerical Treatment of Domain Integrals without Internal Cells in Three-Dimensional BIEM Formulations, CMES (Computer Modeling in Engineering & Sciences), Vol. 6,

No. 6, pp. 525-536, 2004.

[6] Ochiai, Y. and Yasutomi, Z., Improved Method of Generating a Free-Form Surface Using Integral Equations, Computer-Aided Geometric Design, Vol. 17, No. 3, pp. 233-245, (2000).

[7] Ochiai, Y., Nishitani, H. and Sekiya, T., Stress Analysis with Arbitrary Body Force by Boundary Element Method, Engineering Analysis with Boundary Elements, Vol. 17, pp. 295-302, 1996.

[8] Ochiai, Y., Multidimensional Numerical Integration for Meshless BEM, Engineering Analysis with Boundary Elements, Vol. 27, No. 3, pp. 241-249, 2003.

[9] Nayak, G.C. and Zienkiewicz, O. C., International Journal for Numerical Method in Engineering, 5, (1972), 113.

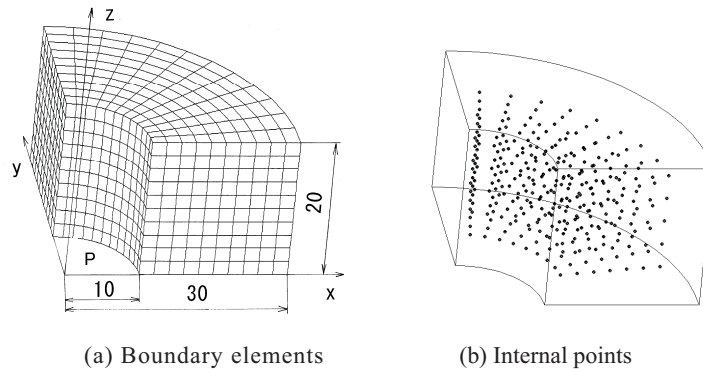


Fig.1 Boundary elements and internal points in quarter-region (Number of boundary elements: 680)

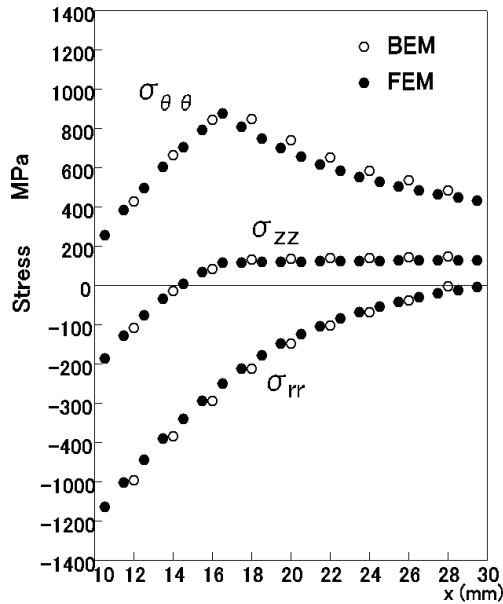


Fig.2 Stress distribution in hollow cylinder with internal pressure

Boundary element analysis of cracked sheets repaired with adhesively bonded anisotropic patches

Useche, J., Sollero, P., Albuquerque E., L.
Universidade Estadual de Campinas
Faculdade de Engenharia Mecânica
CEP 13083-970, Campinas, S.P, Brasil
sollero@fem.unicamp.br

Keywords: cracked sheet, anisotropic repair, adhesive patch, boundary element method, dual reciprocity boundary element method

Abstract

A boundary element formulation for the analysis of isotropic cracked sheets, repaired with adhesively bonded anisotropic patches is presented. The sheet and the patch were modeled using the direct boundary element method. The crack in the isotropic sheet was modeled using the dual boundary element method. The interaction between the isotropic sheet and the patch was modeled considering shear body forces uniformly distributed on the interaction zone using a linear elastic relationship. Two different techniques were used in the present boundary element implementation to treat domain integrals that arise in the formulation due to shear interaction forces. These techniques were the cell domain integration and the dual reciprocity boundary element method.

1. Introduction

Adhesively bonded patches are extensively used in aircraft structure repairs to increase the life of cracked structures and avoid high expenses due the change of cracked components by new ones. When a crack is detected by a non-destructive technique, in aeronautical applications, it is necessary to drill the crack tip region to decrease the stress concentration and then apply a layer of adhesive patch on this region to avoid the crack growth. The patch transfers the load from the cracked structure, avoiding crack opening and a new crack propagation. The main advantages of bonded patches repairs when compared to other types of repairs such as riveted repairs, are the homogeneous load transfer between the cracked plate and the repair and the absence of bolt

holes which are stress concentrators.

Many authors have studied the behavior of adhesively patched sheets. In general, the sheet, the patch, and the adhesive layer are considered to be thin. Thus, the whole component does not bend out of its plane, and the problem can be solved using the two-dimensional elasticity theory. Early works analyzing isotropic patches in structures were presented by Ratwani [1], and Erdogan and Arin [2] in the seventies. These works have presented the study of bonded repairs in infinite plates with cracks. They used analytical solutions for the deformation and compatibility of displacements between the cracked plate and the repair.

Michell and Wooley [3] used the finite element method (FEM) to study the reinforcement of plates induced by the application of repairs. They used two-dimensional finite elements with constant stresses and the plate and the repair were coupled through nodes where conditions of displacement compatibility were imposed. They also analyzed the presence of a crack in the plate. However, they haven't considered the stress singularity in the crack tip and haven't evaluated stress intensity factors.

Jones and Callinan [4,5,6] used the FEM for the analysis of metallic plates repaired with a layer of composite material. They developed a stiffness matrix to couple the plate, the adhesive layer, and the composite repair. Special singular elements were used in the tip of the crack.

Young, Cartwright and Rooke [7] modeled the cracked plate and the repair using the boundary element method (BEM). Shear stresses in the adhesive layer as well as body forces acting on the plate and on the repair were modeled. A special Green function for domains with cracks are used to model straight cracks, which limits the applicability of the model.

Tam and Sherk [8] studied the problem of cracked plates repaired by bonded composite materials. A spring model was used to couple the cracked plate model with the repair model.

The repair was modeled using the FEM and the crack using the BEM. Young et al. [9] modeled the interaction force between the plate and the repair by discretizing the bonded repaired area using internal cells in the boundary element formulation.

Salgado and Aliabadi [10] used the dual boundary element method (DBEM) to model the metallic cracked plate and the direct boundary element method to model the repair. The distributed force between the plate and the repair was considered through the dual reciprocity boundary element method (DRBEM). This formulation was applied by Salgado and Aliabadi [11] to the analysis of metallic thin plates reinforced with bonded isotropic repairs. The reinforced plate was modeled using the BEM. Shear stresses in the adhesive layer were modeled as action-reaction body forces exchanged between the plate and the repair. Widagdo and Aliabadi [14,15] presented a DBEM formulation for composite repair patches adhesively bonded and mechanically fastened to metallic cracked sheets.

In this work, the sheet and the patch were modeled using the BEM and the crack in the isotropic sheet was modeled using the DBEM. The interaction between the isotropic sheet and the patch was modeled considering shear body forces uniformly distributed on the interaction zone using a linear elastic relationship. Two different techniques were used to treat domain integrals that arise in the formulation because of interaction shear forces: the cell domain integration method and the DRBEM.

2. Problem description

Figure 1 presents a finite isotropic sheet, containing an inner crack and an adhesive patch. In this case, the interaction forces can be treated as unknown body forces exchanged by the sheet and the patch over the attachment subregion. This interaction occurs in the region of the attachment. If the sheet and the patch remain flat after deformation, two-dimensional elasticity theory can be used to study the problem. In this case, displacements at the sheet and at the patch have to be compatible with the shear deformation of the adhesive layer connecting them.

3. DBEM for cracked repaired sheets

When the sheet is deformed due to applied loads on its boundaries, interaction forces occur between the sheet and patch the repair. Considering that the structure remains flat after the deformation, the two-dimensional elasticity theory can be used to model this problem. In this two-dimensional case, interaction forces on the sheet and on the patch can be treated as unknown body forces (action-reaction pair). As shown by Salgado [11], the boundary integral equation for displacement of a source point \mathbf{x}' on the sheet is given by (see figure 1):

$$c_{ij}^S(\mathbf{x}')u_j^S(\mathbf{x}') + \int_{\Gamma} T_{ij}^{*S}(\mathbf{x}', \mathbf{x})u_j^S(\mathbf{x}')d\Gamma = \int_{\Gamma} U_{ij}^{*S}(\mathbf{x}', \mathbf{x})t_j^S(\mathbf{x}')d\Gamma + \frac{1}{h_S} \int_{\Gamma} U_{ij}^{*S}(\mathbf{x}', \mathbf{x})b_j^S(\mathbf{x}')d\Omega_R \quad i, j = 1, 2 \quad (1)$$

where c_{ij}^S is a coefficient which depends on the position of the source point in relation to the boundary of the sheet Γ_S ; U_{ij}^{*S} and T_{ij}^{*S} are the Kelvin's fundamental solutions for bidimensional elastic media; u_j^S and t_j^S are displacement and traction vectors at the boundary of the sheet; b_j are the interaction forces exchanged between the sheet and the patch on the region of the patch, Ω_R ; and h_S is the thickness of the sheet.

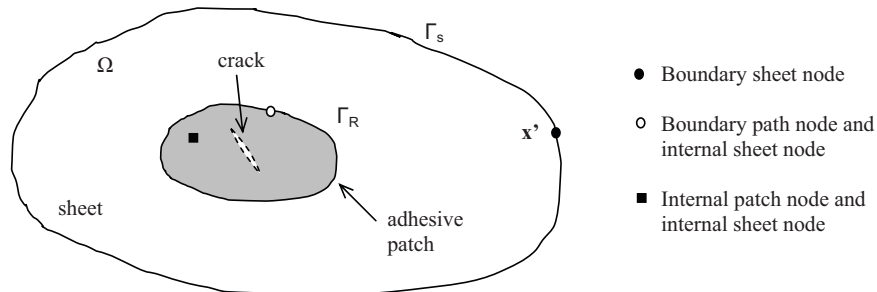


Figure 1. Sheet with patch repair

In a similar way, the displacement of a source point \mathbf{x}' on the repair is given by:

$$c_{ij}^R(\mathbf{x}')u_j^R(\mathbf{x}') + \int_{\Gamma} T_{ij}^{*R}(\mathbf{x}', \mathbf{x})u_j^R(\mathbf{x}')d\Gamma = \int_{\Gamma} U_{ij}^{*R}(\mathbf{x}', \mathbf{x})t_j^R(\mathbf{x}')d\Gamma + \frac{1}{h_R} \int_{\Gamma} U_{ij}^{*R}(\mathbf{x}', \mathbf{x})b_j^R(\mathbf{x}')d\Omega_R \quad i, j = 1, 2 \quad (2)$$

Similar to the sheet, c_{ij}^R is a coefficient which depends on the position of the source point in relation to the boundary of the repair Γ_R ; U_{ij}^{*R} and T_{ij}^{*R} are the Kelvin's fundamental solution for bidimensional elastic media; u_j^R and t_j^R are displacement and traction vectors at the boundary repair, b_j are the interaction forces exchanged between the sheet and the patch on the region of the patch, Ω_R ; and h_R is the thickness of the sheet. In this work, Kelvin's fundamental solution for bidimensional elastic media, U_{ij}^{*R} , was used to model the mechanical response of the isotropic sheet. A fundamental solution for anisotropic elastic media was used to model the mechanical patch response.

The crack in the isotropic sheet was modeled using the DBEM. The traction equation is used in a crack face and the displacement equation in the other face. The traction equation is given by:

$$\frac{1}{2}t_j^S(\mathbf{x}') + n_i(\mathbf{x}') \int_{\Gamma} S_{ijk}^{*S}(\mathbf{x}', \mathbf{x})u_j^S(\mathbf{x}')d\Gamma = n_i(\mathbf{x}') \int_{\Gamma} D_{ijk}^{*S}(\mathbf{x}', \mathbf{x})t_j^S(\mathbf{x}')d\Gamma + \frac{1}{h_S} \int_{\Gamma} D_{ij}^{*S}(\mathbf{x}', \mathbf{x})b_j^S(\mathbf{x}')d\Omega_R \quad i, j = 1, 2 \quad (3)$$

where $S_{ijk}^{*S}(\mathbf{x}', \mathbf{x})$ and $D_{ijk}^{*S}(\mathbf{x}', \mathbf{x})$ are linear combinations of derivatives of $T_{ij}^{*S}(\mathbf{x}', \mathbf{x})$ and $U_{ij}^{*S}(\mathbf{x}', \mathbf{x})$, respectively, and n_i is a unit vector outward to the boundary in the collocation point.

Now, consider a uniform shear deformation through the adhesive thickness, as proposed by Salgado [10], and neglect shear deformations in the sheet and in the patch. Differences Δu_j between the displacements u_j of a point \mathbf{x}' ($\mathbf{x}' \in \Omega_R$) on the sheet and u_j^R of corresponding points on the patch, can be written as:

$$u_j^S(\mathbf{x}') - u_j^R(\mathbf{x}') = \frac{h_A}{G_A} b_j(\mathbf{x}') \quad j = 1, 2 \quad (4)$$

where h_A is the thickness of the adhesive layer, G_A is the transversal stiffness modulus of the adhesive material, τ_j is the shear stress in the adhesive, which has the same meaning of the interaction force b_j .

4. Domain integral computation

As can be seen, equations (1) and (2) require to calculate domain integrals. Two different techniques were used to treat domain integrals that arise in the formulation due to shear interaction forces. These techniques were the cell domain integration method and the DRBEM. In the cell method, the domain is subdivided, so that:

$$\int_{\Gamma} U_{ij}^*(\mathbf{x}', \mathbf{x}) b_j(\mathbf{x}) d\Omega_R \cong \sum_{i=1}^{ncells} \int_{\Omega_i} U_{ij}^*(\mathbf{x}', \mathbf{x}) b_j(\mathbf{x}) d\Omega_i \quad (5)$$

and the integration is carried out on each cell. In the DRBEM, interaction forces are approximated as a sum of unknown coefficients α^d multiplied by approximating functions $f^d(\mathbf{x}^d, \mathbf{x})$, so that:

$$b_j(\mathbf{x}) = \sum_{d=1}^D \alpha_j f^d(\mathbf{x}^d, \mathbf{x}) \quad (6)$$

The approximating function used in this work is $f^d(\mathbf{x}^d, \mathbf{x}) = 1 - r$ in the sheet formulation. For the anisotropic patch, an approximation function given by Albuquerque and Sollero [12] was used. Then, equation (5) can be expressed as:

$$\int_{\Omega_R} U_{ij}^{*S}(\mathbf{x}', \mathbf{x}) b_j(\mathbf{x}) d\Omega_R = -\frac{1}{h_S} \sum_{d=1}^D \alpha_k \left[c_{ij}(\mathbf{x}^d) \hat{u}_{kj}^d(\mathbf{x}^d) + \int_{\Gamma_R} T_{ij}^{*S}(\mathbf{x}', \mathbf{x}) \hat{t}_{kj}^d d\Gamma_R - \int_{\Gamma_R} U_{ij}^{*S}(\mathbf{x}', \mathbf{x}) \hat{t}_{kj}^d d\Gamma_R \right] \quad (7)$$

where \hat{u}_{kj}^d and \hat{t}_{kj}^d are particular solutions for displacements and tractions corresponding to a predefined function $f^d(\mathbf{x}^d, \mathbf{x}) = 1 - r$ for the sheet. A similar approach was used to model body forces in the patch.

4.1 Matrix formulation

In a matrix form, the equation for isotropic sheet (including traction equation) can be write as:

$$\begin{bmatrix} \mathbf{H}_{ext}^S & \mathbf{0} \\ \mathbf{H}_{int}^S & \mathbf{I} \end{bmatrix} \begin{Bmatrix} \mathbf{u}_{ext}^S \\ \mathbf{u}_{int}^S \end{Bmatrix} - \begin{bmatrix} \mathbf{G}_{ext}^S & \mathbf{0} \\ \mathbf{G}_{int}^S & \mathbf{0} \end{bmatrix} \begin{Bmatrix} \mathbf{t}_{ext}^S \\ \mathbf{0} \end{Bmatrix} = \begin{bmatrix} \mathbf{A}_{ext}^S & \mathbf{0} \\ \mathbf{A}_{int}^S & \mathbf{0} \end{bmatrix} \begin{Bmatrix} \boldsymbol{\alpha}^S \\ \mathbf{0} \end{Bmatrix} \quad (8)$$

where subindex “*ext*” and “*int*” identify boundary and domain collocation and field points on sheet. In compact form, we have:

$$\mathbf{H}^S \mathbf{u}^S - \mathbf{G}^S \mathbf{t}^S = \mathbf{A}^S \boldsymbol{\alpha}^S \quad (9)$$

In a similar way, equations for the repair can be written as:

$$\begin{bmatrix} \mathbf{H}_{ext}^R & \mathbf{0} \\ \mathbf{H}_{int}^R & \mathbf{I} \end{bmatrix} \begin{Bmatrix} \mathbf{u}_{ext}^R \\ \mathbf{u}_{int}^R \end{Bmatrix} - \begin{bmatrix} \mathbf{G}_{ext}^R & \mathbf{0} \\ \mathbf{G}_{int}^R & \mathbf{0} \end{bmatrix} \begin{Bmatrix} \mathbf{t}_{ext}^R \\ \mathbf{0} \end{Bmatrix} = \begin{bmatrix} \mathbf{A}_{ext}^R & \mathbf{0} \\ \mathbf{A}_{int}^R & \mathbf{0} \end{bmatrix} \begin{Bmatrix} \boldsymbol{\alpha}^R \\ \mathbf{0} \end{Bmatrix} \quad (10)$$

where subindex “*ext*” and “*int*” identify boundary and domain collocation and field points on the patch. Similarly in a compact form, we have:

$$\mathbf{H}^R \mathbf{u}^R - \mathbf{G}^R \mathbf{t}^R = \mathbf{A}^R \boldsymbol{\alpha}^R \quad (11)$$

In the general case, when the sheet and the patch are made of different materials, the coupling equation (4) can be written for the sheet and the repair, as:

$$\begin{aligned} k^{-1} \left[(\mathbf{F}^{-1})^S \mathbf{u}^S - (\mathbf{F}^{-1})^S \mathbf{u}^R \right] &= \boldsymbol{\alpha}^S \\ k^{-1} \left[(\mathbf{F}^{-1})^R \mathbf{u}^S - (\mathbf{F}^{-1})^R \mathbf{u}^R \right] &= \boldsymbol{\alpha}^R \end{aligned} \quad (12)$$

The constant k contains the mechanical properties of adhesive layer. Introducing these equations in (9) and (11) we obtain the coupling equation system for the problem of repaired sheet:

$$\begin{bmatrix} (\mathbf{H} - \mathbf{A}\mathbf{F}^{-1})^S & (\mathbf{A}\mathbf{F}^{-1})^S \\ (\mathbf{H} - \mathbf{A}\mathbf{F}^{-1})^R & (\mathbf{A}\mathbf{F}^{-1})^R \end{bmatrix} \begin{Bmatrix} \mathbf{u}^S \\ \mathbf{u}^R \end{Bmatrix} = \begin{bmatrix} \mathbf{G}^S & \mathbf{0} \\ \mathbf{0} & \mathbf{G}^R \end{bmatrix} \begin{Bmatrix} \mathbf{q}^S \\ \mathbf{q}^R \end{Bmatrix} \quad (13)$$

5. Applications

5.1 A circular composite patch over an uncracked square sheet. A square sheet whose edge length is 200 mm is subjected to a uniform constant tension of 1 GPa towards the y axis, as shown in the figure 2. A central crack of length $2a = 30$ mm in the sheet is considered. The sheet has a thickness of 1.5 mm. A circular repair of radius equal to 30 mm and thickness of 1.5

mm is bonded at the center of the sheet using an adhesive with 0.15 mm of thickness and shear modulus $G = 0.6$ GPa. Properties of the sheet and the patch are given in table 1.

Sheet	Patch
Young modulus (E) = 72400 Mpa	$E_1 = 25000$ MPa
Poisson's ratio(ν) = 0.3	$E_2 = 208000$ MPa
	$G_{12} = 72400$ MPa
	$\nu_{12} = 0.02$

Table 1. Mechanical properties of the sheet and the composite patch

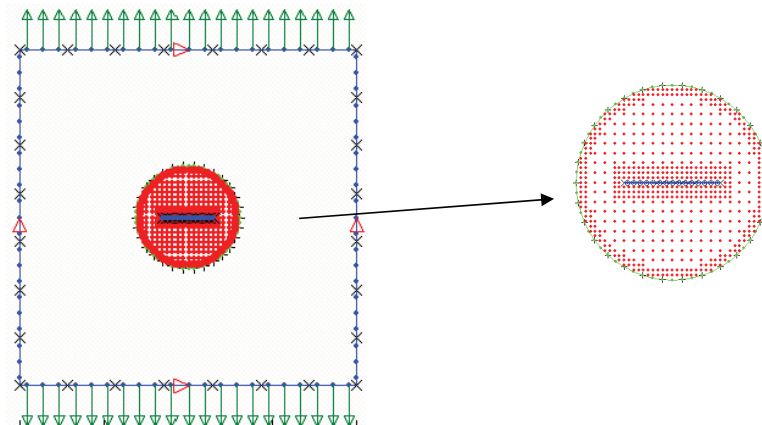


Figure 2. Boundary elements and internal cells (and DRBEM points) for the cracked plate and the patch.

The problem was analyzed using the method of cells and the DRBEM. The mesh comprises of 28 discontinuous quadratic elements on the edge of the plate and on the edge of the repair, as shown in figure 2. The shear stress distribution in the adhesive layer obtained using the DRBEM is shown in figure 3.

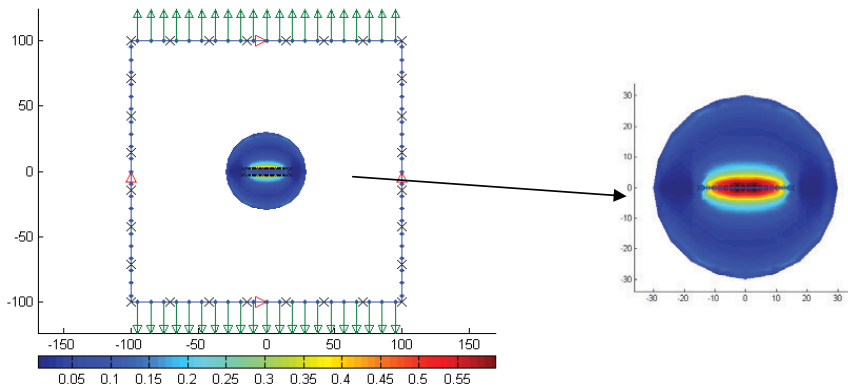


Figure 3. Normalized shear stress distribution in the adhesive

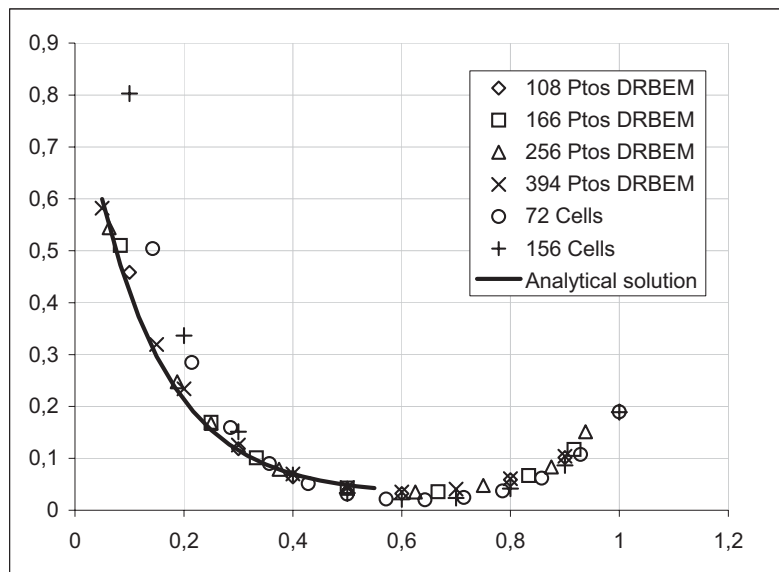


Figure 4. Shear stress in the adhesive layer at $x = 0$ and $0 \leq y/R \leq 1$.

The shear distribution obtained in the model with cells is similar and will not be shown here. As

can be seen in figure 4 the convergence of the solution is obtained as the number of internal points increases. Further refinement in the boundary mesh hasn't significantly affected the results. Obtained results are compared with analytical solution given by Rose [13] for a cracked isotropic sheet repaired with an orthotropic patch. It can be seen that good agreement was obtained even for relatively coarse internal points grids when the DRBEM were used. Slowest convergence to Rose's solution was found with cell method.

6. Conclusions

A new boundary element formulation for modelling cracked sheets repaired with composite patches was developed. The cracked sheet was modeled with the DBEM and the patch was modeled with the BEM. The interaction between the isotropic sheet and the patch was modeled considering shear body forces uniformly distributed on the interaction zone using a linear elastic relationship. The cell domain integration and the dual reciprocity have been used to treat the domain integrals that arise in the formulation due to shear interaction forces. DRBEM method showed faster convergence to analytical solution than the cell method. It can be concluded that the new formulation can be used with reasonable accuracy to study the mechanical behaviour of adhesively bonded repairs.

References

1. Ratawani, M. N. Analysis of cracked adhesively bonded laminate structures. *AIAA Journal* 1979; 17: 988-994.
2. Erdogan, F. and Arin, K. A sandwich plate with a part-through and debonding crack. *Engineering Fracture Mechanics* 1972; 4: 449-458.
3. Mitchell, R. A., Wooley, R. M., Chwiruth, D. J. Analysis of composite reinforced cutouts and cracks *AIAA Journal* 1975; 13: 744-749.
4. Jones R. and Callinan, R. J. On the use of special crack tip elements in cracked elastic sheets. *International Journal of Fracture* 1977; 3: 51-64.
5. Jones R. and Callinan, R. J. Finite element analysis of patched cracks. *Journal of Structural Mechanics* 1979; 2: 107-130.
6. Jones R. and Callinan, R. J. A design study in crack patching. *Fibre Science and Technology* 1981; 14: 99-111.
7. Young, A., Cartwright, D. J, Rooke, D. P. The boundary element method for analyzing repairs paletes on cracked finite sheets. *Proceedings of the 4rd International conference on numerical methods in fracture mechanics*, Owen D.R.J. and Luxmoore A.R. (edts). San Antonio EUA 1988; 463-479.

8. Tarn, J. G. and Shek, K. L. Analysis of cracked plates with a bonded patch. *Engineering Fracture Mechanics* 1991; 40: 1055-1065.
9. Young, A. Influence of tapering on the stresses in repair patches. *Proceedings of the 3rd International conference on numerical methods in fracture mechanics*, Owen D.R.J. and Luxmoore A.R. (eds). San Antonio, EUA 1987; 741-752.
10. Salgado, N. E. and Aliabadi, M. H. Dual reciprocity method for the analysis of adhesively patched sheets. *Communications in Numerical Methods in Engineering* 1997; 13: 397-405.
11. Salgado, N. K. and Aliabadi, M. H. The boundary element analysis of cracked stiffened sheets, reinforced by adhesively bonded patches. *International journal for numerical methods in engineering* 1998; 42: 195-217.
12. Albuquerque, E. L. and Sollero, P., Aliabadi, M.H., The boundary element method applied to time dependent problems in anisotropic materials. *International Journal of Solid and Structures* 2002; 39: 1405-1422.
13. Rose, L.R., An application of the inclusion analogy for bonded reinforcements. *Int. J. Solid Structures* 1981; 17: 827-838.
14. Widagdo, D. and Aliabadi, M.H., Boundary element analysis composite repair patches. In *Advances in Boundary Element Techniques II*, Denda, M., Aliabadi, M.H., Charafi, A. (Eds.), New Jersey, 2001; 327-335.
15. Widagdo D., Aliabadi M.H., Boundary element analysis of cracked panels repaired by mechanically fastened composite patches. *Engineering Analysis with Boundary Elements* 2001; 25: 339-345.

Dynamic Analysis of Piezoelectric Structures by the Dual Reciprocity Boundary Element Method

Grzegorz Działkiewicz, Piotr Fedelinski

Silesian University of Technology,
Department for Strength of Materials and Computational Mechanics,
44-100 Gliwice, Konarskiego 18A, Poland,
email: Grzegorz.Działkiewicz@polsl.pl, Piotr.Fedelinski@polsl.pl

Keywords: piezoelectric material, coupled fields, eigenvalue problem, dynamics, boundary element method, dual reciprocity method.

Abstract. The aim of the present work is to show the formulation and application of the dual reciprocity boundary element method (BEM) to free vibrations of two-dimensional piezoelectric structures. The piezoelectric materials are modelled as homogenous, linear – elastic, transversal isotropic and dielectric. The static fundamental solutions, which are required in the proposed approach, are derived using the Stroh formalism. The domain inertial integral is transformed to the equivalent boundary integral using the dual reciprocity method (DRM). The developed method is used to compute frequencies and mode shapes of natural vibrations of two-dimensional piezoelectric structures. The boundary conditions are imposed using the condensation method. The numerical results are compared with the available analytical solutions given in the literature.

Introduction

In piezoelectric materials, mechanical and electric fields are coupled, namely, they produce an electric field when deformed or conversely, they deform when subjected to an electric field. Dynamic analysis of piezoelectric materials requires the solution of coupled electric and mechanical partial differential equations of motion [1]. These equations, particularly for piezoelectric structures with arbitrary geometries and boundary conditions, are usually solved by numerical methods. One of the versatile computer methods, which is intensively applied in piezoelectricity in the last decade, is the boundary element method (BEM). In this paper the BEM [2] is implemented to solve a free vibration problem of the linear piezoelectricity.

The most popular piezoelectric materials are ceramics. These piezoelectrics are solids, which belong to the hexagonal symmetry class of the crystals [1]. Piezoceramics have anisotropic physical properties (both mechanical and electrical), therefore in the present work homogeneous, transversal isotropic, linear elastic and dielectric model of the piezoelectric material is considered. The anisotropy of the material increases the number of the material constants, and derivation of the fundamental solutions becomes difficult.

The Stroh formalism [3, 4, 5] is a powerful and elegant analytic technique for the anisotropic elasticity, which is expanded to the linear piezoelectricity in this work. For the free vibration problem or transient analysis, derivation of the dynamic fundamental solution is much more complicated [6]. The dual reciprocity boundary element method allows the use of the static fundamental solution for dynamic problems [2, 7, 8]. The dual reciprocity formulation is derived from the reciprocal relation between a static state and a dynamic state in which the inertia forces are treated as body forces. This method is used to transform the domain integral, which depends on inertia, into the boundary integral. After discretization the system matrices are independent of time.

A numerical example is presented and it shows that the dual reciprocity boundary element method allows to analyze efficiently the free vibration problem of linear piezoelectricity.

The dual reciprocity BEM formulation of linear piezoelectricity

The coupled field equations of piezoelectricity are given by the following system of partial differential equations [1, 7]:

$$\begin{aligned} C_{ijkl}u_{k,li} + e_{lij}\phi_{,li} &= \rho\ddot{u}_j - b_j \\ e_{ikl}u_{k,li} - \varepsilon_{il}\phi_{,li} &= 0 \end{aligned} \quad (1)$$

The tensors C_{ijkl} , e_{lij} , ε_{il} denote elastic moduli, measured in a constant electric field, piezoelectric constants and dielectric constants, measured at constant strains, respectively; u_k is the displacement vector, ϕ denotes the electric potential; b_j is the body force vector per unit volume and ρ denotes the density. Double dots denote the second derivative with respect to time. In equations (1) the intrinsic electric charge q is neglected.

To get the classical boundary-initial value problem formulation, equations (1) must be completed with the boundary and initial conditions. The boundary conditions are both mechanical and electric and they are related to the parts of the boundary where displacements, tractions, potentials and charge flux densities are prescribed. The coupled field equations with boundary and initial conditions formulate the direct problem of linear piezoelectricity.

The boundary-initial value problem of linear piezoelectricity can be formulated in a much more convenient form using generalized quantities. The following vectors are introduced:

$$U_K = \begin{Bmatrix} u_k \\ \phi \end{Bmatrix}; T_J = \begin{Bmatrix} t_j \\ q \end{Bmatrix}; B_J = \begin{Bmatrix} b_j \\ 0 \end{Bmatrix}, \quad (4)$$

where U_K , T_J and B_J are the generalized displacement, traction and body force vector, respectively. Then, the coupled field equations are given by the operator equation:

$$L_{JK}U_K = D_{JK}U_K - B_J, \quad (5)$$

where L_{JK} is the 2D elliptic operator of static piezoelectricity and D_{JK} is a differential operator.

In the present work homogeneous, transversal isotropic, linear elastic and dielectric model of the piezoelectric material is chosen. For this model, the operator L_{JK} , for the two - dimensional case, has a form:

$$L_{JK} = \begin{bmatrix} c_{11}\partial_{11} + c_{33}\partial_{22} & (c_{12} + c_{13})\partial_{12} & (e_{21} + e_{13})\partial_{12} \\ & c_{33}\partial_{11} + c_{22}\partial_{22} & e_{13}\partial_{11} + e_{22}\partial_{22} \\ sym & & -\varepsilon_{11}\partial_{11} - \varepsilon_{22}\partial_{22} \end{bmatrix}, \quad (6)$$

where ∂_{ij} is a differential operator, which denotes differentiation with respect to the spatial coordinates. The coefficients c_{ij} , e_{ij} and ε_{ij} are the values of the elastic, piezoelectric and dielectric constants, respectively.

The next step in the BEM formulation is application of a reciprocity relation. This process is well known [2, 7]. The system of equations (5) is weighted with a test function and integrated by parts.

When the test function is chosen as a fundamental solution of the static piezoelectric operator L_{JK} and a limiting process to the boundary is done, the boundary integral formula is given by:

$$c_{KJ}J_J + \int_{\Gamma} T_{KJ}U_J d\Gamma = \int_{\Gamma} U_{KJ}T_J d\Gamma - \int_{\Omega} U_{KJ}D_{JL}U_L d\Omega, \quad (7)$$

where c_{KJ} denotes a free term coefficient at the source point, U_{MJ} is the test function – the fundamental solution, and T_{MJ} depends on the derivative of the fundamental solution and Ω denotes the region which is occupied by the piezoelectric body. In this equation the generalized body force vector is neglected.

To obtain the fundamental solutions, the Stroh formalism is used [3, 4, 9].

The domain integral in equation (7), which describes the inertia effect, will be transformed into the boundary integral using the reciprocal theorem between two static states [2, 7].

Let the generalized accelerations be approximated using a sum of functions multiplied by unknown coefficients:

$$D_{JL}U_L \approx \sum_{m=1}^M F_{JN}^m \alpha_N^m. \quad (8)$$

In the above equation unknown coefficients depend on time, but functions F are time independent. The functions F are related to the inhomogeneous differential equation of static piezoelectricity:

$$L_{JK}U_{KN}^m = F_{JN}^m. \quad (9)$$

Weighting the equation above with the static fundamental solution U_{LJ} one can obtain:

$$\int_{\Omega} U_{LJ} F_{JN}^m d\Omega = -c_{LK}U_{KN}^m - \int_{\Gamma} T_{LJ}U_{JN}^m d\Gamma + \int_{\Gamma} U_{LJ}T_{JN}^m d\Gamma. \quad (10)$$

Using this new reciprocal relation and approximation of the generalized acceleration field leads to the dual reciprocity formulation of the dynamic piezoelectricity [7]:

$$c_{KJ}U_J + \int_{\Gamma} T_{KJ}U_J d\Gamma = \int_{\Gamma} U_{KJ}T_J d\Gamma + \sum_{m=1}^M \left(c_{KJ}U_{JN}^m + \int_{\Gamma} T_{KJ}U_{JN}^m d\Gamma - \int_{\Gamma} U_{KJ}T_{JN}^m d\Gamma \right) \alpha_N^m. \quad (11)$$

To solve approximately the boundary integral equation, the boundary element method is applied.

The operator D_{JK} shows that the electric potential has no influence on the inertia term, hence the approximation of the generalized acceleration field, has a special form [7].

The discretized equation (11) is applied to all boundary nodes, and it leads to the following linear system of equations:

$$HU - GT = (H\hat{U} - G\hat{T})\alpha, \quad (12)$$

where \hat{U} and \hat{T} denote the nodal values of the particular solution of equation (9), H and G denote the standard BEM matrices. The vectors U and T contain discretized values of the boundary generalized displacements and tractions. Next, one can obtain the following system of linear ordinary differential equations:

$$M\ddot{U} + HU = GT. \quad (13)$$

The mass matrix M is equal to:

$$M = \rho(G\hat{T} - H\hat{U})F_*^{-1}, \quad (14)$$

where matrix F_*^{-1} is the modified inverse of matrix F .

The present system of equations, with the boundary and initial conditions is an approximated discrete form of the boundary-initial value problem of linear piezoelectricity.

The Stroh formalism

Since piezoelectric materials are anisotropic, the fundamental solutions are rather complicated, even for the transversal isotropic model of the material [7]. To obtain the fundamental solutions, the Stroh formalism is used. The Stroh formalism is a powerful and elegant analytic technique for the anisotropic elasticity [4, 5], which is expanded to the linear piezoelectricity in this case [3, 9]. The formalism requires the solution of the special eigenvalue problem with respect to the material constants of the piezoelectric material.

In the Stroh formalism it is assumed that the field of the generalized displacements has a form [3, 4, 9, 10]:

$$U = af(z), \quad (15)$$

where a is the unknown vector and $f(z)$ is an analytic complex function and z is a complex variable:

$$z = x_1 + px_2, \quad (16)$$

where x_1 and x_2 are the coordinates, p denotes the unknown complex constant. Introducing equations (15) into the coupled field equations (1) for a static case, the quadratic eigenvalue problem is obtained:

$$\{Q + p(R + R^T) + p^2T\}a = 0, \quad (17)$$

where the matrices Q , R and T depend only on the material constants. The above equation can be transformed into the standard eigenvalue problem.

It is known, that the eigenvalue problem (17), in a two – dimensional case, gives three pairs of complex conjugate eigenvalues and corresponding eigenvectors.

For piezoelectric materials eigenvalues are distinct, so it can be written that the solution (15) is equal to:

$$U = \sum_{j=1}^3 \left\{ a_j f_j(z_j) + \bar{a}_j f_{j+3}(\bar{z}_j) \right\}, \quad (18)$$

where functions f_1, \dots, f_6 have arguments in the form:

$$z_j = x_1 + p_j x_2. \quad (19)$$

Most often functions f have the same form, but with a different complex coefficient vector.

Now, the fundamental solution can be obtained. The complex function f_j will have a form [3]:

$$f(z_j) = \ln(z_j - s_j), \quad (20)$$

where:

$$s_j = x_1^0 + p_j x_2^0. \quad (21)$$

The Green functions (the fundamental solutions) of piezoelectric elliptic operator L_{JK} (6) is then given by:

$$\begin{aligned} U_{KL} &= \frac{-1}{\pi} \operatorname{Re} \left[\sum_{j=1}^3 A_{LJ} V_{JK} \ln(z_j - s_j) \right], \\ T_{KL} &= \frac{1}{\pi} \operatorname{Re} \left[\sum_{j=1}^3 B_{LJ} \frac{p_j n_1 - n_2}{z_j - s_j} V_{JK} \right], \end{aligned} \quad (22)$$

where matrices A , B and V depend on the eigenvectors of eigenvalue problem given by (17).

Particular solutions

The dual reciprocity method requires the solution of the inhomogeneous partial differential equation of the static piezoelectricity (9). The procedure, which leads to the solution, is quite difficult for piezoelectric materials because the anisotropy introduces many material constants. An alternative is to assume a particular solution and find the corresponding functions.

In this formulation the particular solution is assumed as a radial basis function with a constant term [7]:

$$U_{KN}^m = \delta_{KN} (r^3 + r^2 + C), \quad (23)$$

where δ_{KN} is a Kronecker isotropic tensor. To obtain the corresponding traction field and an "artificial" body force term, the derivatives of the assumed particular solution are calculated:

$$\begin{aligned} U_{KN,j}^m &= \delta_{KN} (3r^2 + 2r) r_j \\ U_{KN,ji}^m &= \delta_{KN} [(3r + 2)\delta_{ji} + 3r r_j r_i] \end{aligned} \quad (24)$$

Then the traction field and body force field are described by the following equations:

$$\begin{aligned} T_{jN}^m &= C_{iJKI} U_{KN,j}^m n_i \\ F_{jN}^m &= C_{iJKI} U_{KN,ji}^m \end{aligned} \quad (25)$$

The eigenvalue problem formulation

When the boundary conditions are known, the matrix equation of motion can be written in the form [8]:

$$\begin{bmatrix} M_{uu} & M_{ut} \\ M_{tu} & M_{tt} \end{bmatrix} \begin{bmatrix} \ddot{U}_u \\ \ddot{U}_t \end{bmatrix} + \begin{bmatrix} H_{uu} & H_{ut} \\ H_{tu} & H_{tt} \end{bmatrix} \begin{bmatrix} T_u \\ T_t \end{bmatrix} = \begin{bmatrix} G_{uu} & G_{ut} \\ G_{tu} & G_{tt} \end{bmatrix} \begin{bmatrix} T_u \\ T_t \end{bmatrix}, \quad (26)$$

where the subscript u is related to the part of the boundary, where the generalized displacements are prescribed and t corresponds to the part of the boundary, where the generalized tractions are known, hence the generalized displacements are unknown on this part of the boundary. Eliminating the unknown generalized tractions and assuming that the known generalized tractions are equal to zero, the following system of equations can be obtained:

$$M_{red} \ddot{U}_t + H_{red} U_t = 0, \tag{27}$$

where:

$$M_{red} = M_{tt} - G_{tu} G_{uu}^{-1} M_{ut}, \quad H_{red} = H_{tt} - G_{tu} G_{uu}^{-1} H_{ut}. \tag{28}$$

In the free vibration problem it is assumed that the solution of the equation of motion are harmonic functions, then the generalized eigenvalue problem is described by the equation:

$$H_{red} X = \omega^2 M_{red} X, \tag{29}$$

where X is an amplitude and ω is an angular frequency. From the formulation of the dynamic problem of linear piezoelectricity it is known that the electric potential does not influence the inertia term. The process of eliminating the electric degrees of freedom is equivalent to the Guyan reduction method, which is exact in this formulation. The two - step condensation process reduces number of degrees of freedom. The above equation can be transformed into the standard eigenvalue problem.

Numerical examples

The eigenvalue problem for the rectangular piezoelectric plate made of PZT-4 ceramic [10] is considered. The length of the plate is equal to $L=0.04$ m, and height is equal to $H=0.01$ m, as shown in Figure 1.

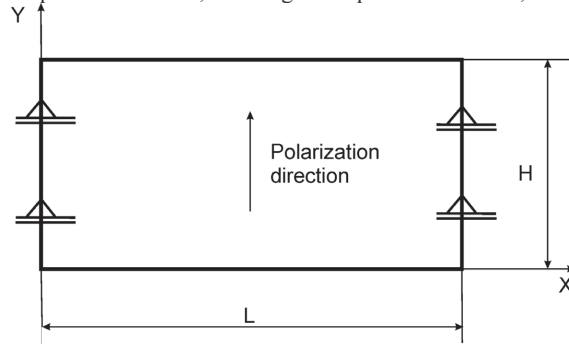


Figure 1: Piezoelectric strip

The piezoelectric plate is simply supported – the nodes on the vertical edges can only move in the horizontal direction. The edges are electrically grounded to zero potential – this boundary condition is called the closed condition. To discretize the boundary of the plate 100 constant boundary elements are applied. When only the boundary is discretized, the inertia is modelled inaccurately [8]. The internal nodes are necessary to improve the accuracy of the solution.

The results of the eigenfrequencies analysis for the smallest 5 thickness modes using 114 internal nodes are given in Table 1. In this table a comparison between the obtained results and analytical [10] is presented. A good agreement between both formulations can be observed. The eigenfrequencies are scaled [10].

mode	$\bar{\omega}_0$ analytical	$\bar{\omega}_0$ BEM	relative error [%]
1	2.26	2.31	2.21
2	10.09	9.88	2.08
3	24.09	24.10	0.04
4	41.66	41.83	0.41
5	49.51	50.00	0.99

Table 1: Comparison between analytical and BEM solution

When on the bottom and top edges of the plate the charge flux density is equal to zero – the boundary conditions are called open [11]. The influence of the boundary conditions on normalized eigenfrequencies are given in Table 2 and for the same mode, the eigenfrequencies for the open circuit are bigger.

mode	$\bar{\omega}_c$ closed ($\varphi=0$)	$\bar{\omega}_o$ open ($q=0$)
1	2.31	2.38
2	9.88	10.77
3	24.10	28.40
4	41.83	44.21
5	50.00	54.08

Table 2: Comparison between open and closed boundary condition

Summary

In this paper, the dual reciprocity BEM for the free vibration problem of linear piezoelectricity is considered. The results confirm that the present formulation allows to solve the eigenvalue problem of linear piezoelectricity with different electric boundary conditions. The two step condensation method reduces degrees of freedom. This is an important property of the present method, because an accurate analysis requires many internal degrees of freedom, which allows to avoid complex eigenfrequencies.

Acknowledgement

The scientific research is financed by the Ministry of Education and Science of Poland in years 2005-2006 as the grant No. 4-T07A-051-28.

References

- [1] H.F. Tiersten: *Linear piezoelectric plate vibrations*. Plenum Press, New York (1969).
- [2] C.A. Brebbia and J. Dominguez: *Boundary elements. An introductory course*. Computational Mechanics Publications. McGraw – Hill Book Company, Southampton – Boston (1992).
- [3] E. Pan: A BEM analysis of fracture mechanics in 2D anisotropic piezoelectric solids. *Engineering Analysis with Boundary Elements*, **23**, 67-76 (1999).
- [4] T.C.T. Ting and Y.M. Wang: The Stroh formalism for anisotropic materials that possess an almost extraordinary degenerate matrix N. *International Journal of Solids and Structures*, **34**, 401-413 (1997).
- [5] T.C.T. Ting: *Anisotropic elasticity. Theory and applications*. Oxford University Press, New York – Oxford (1996).
- [6] M. Denda, Y. Araki and Y.K. Yong: Time-harmonic BEM for 2-D piezoelectricity applied to eigenvalue problems. *International Journal of Solids and Structures*, **41**, 7241-7265 (2004).
- [7] L. Gaul and M. Kogl: A boundary element method for transient piezoelectric analysis. *Engineering Analysis with Boundary Elements*, **24**, 591-598 (2000).
- [8] L. Gaul and M. Kogl: Free vibration analysis of anisotropic solids with the boundary element method. *Engineering Analysis with Boundary Elements*, **27**, 107-144 (2003).
- [9] G. Dziatkiewicz and P. Fedelinski: Boundary element method for solving direct and inverse problems of piezoelectricity. In: *10th International Conference on "Numerical Methods in Continuum Mechanics" NMCM 2005*, University of Zilina, Zilina, 27-28, CD-ROM Proceedings (2005).
- [10] S.S. Vel, R.C. Mever and R.C. Batra: Analytical solution for the cylindrical bending vibration of piezoelectric composite plates. *International Journal of Solids and Structures*, **41**, 1625-1643 (2004).
- [11] P. Heyliger and S. Brooks: Free vibration of piezoelectric laminates in cylindrical bending. *International Journal of Solids and Structures*, **32**, 2945-2960 (1995).

Local Radial Basis Function Collocation Method for Heat Transfer and Fluid Flow Problems

Božidar Šarler

University of Nova Gorica, Laboratory for Multiphase Processes, Vipavska 13, SI-5000 Nova Gorica, Slovenia, email: bozidar.sarler@p-ng.si

Keywords: Mesh-free methods, local radial basis function collocation method, multiquadrics, porous media flow, Navier-Stokes equations, mass conservation, energy conservation, natural convection.

Abstract. This paper formulates a local version of the classical meshless radial basis function collocation (Kansa) method. The formulation copes with the general transport equation, applicable in solution of a broad spectra of scientific and engineering problems. The method is structured on multiquadrics radial basis functions. Instead of globally, the collocation is made locally over a set of overlapping domains of influence and the time-stepping can be performed in an implicit or explicit way. Only small systems of linear equations with the dimension of the number of the nodes included in the domain of influence have to be solved for each node. The computational effort thus grows roughly linearly with the number of the nodes. The developed approach overcomes the principal large-scale problem bottleneck of the original Kansa method. Formulations for solving the steady Darcy natural convection in porous media and natural convection in Newtonian fluids are described.

Introduction

A common complication in the polygon-based (FVM, FEM, BEM) numerical methods is the need to create a polygonisation, either in the domain and/or on its boundary. This type of meshing is often the most time consuming part of the solution process and is far from being fully automated. In recent years, a new class of methods is in development which do not require polygonisation but use only a set of nodes to approximate the solution. The rapid development of these types of meshfree (meshless, polygon-free, mesh-reduction) methods and their classification is elaborated in the very recent monographs [1,2,3,4,5]. A broad class of meshfree methods in development today are based on Radial Basis Functions (RBFs) [6]. The RBF collocation method or Kansa method [7] is the simplest of them. This method has been further upgraded to symmetric collocation [8], to modified collocation [9], and to indirect collocation [10]. The method has been already used in a broad spectrum of computational fluid dynamics problems [11] such as the solution of Navier-Stokes equations or porous media flow [12] and the solution of solid-liquid phase change problems [13]. In contrast to advantages over mesh generation, all the listed methods unfortunately fail to perform for large problems, because they produce fully populated matrices, sensitive to the choice of the free parameters in RBFs. One of the possibilities for mitigating this problem is to employ the domain decomposition [14]. However, the domain decomposition re-introduces some sort of meshing which is not attractive. The concept of local uncoupled collocation in the context of RBF-based solution of transport phenomena has been introduced in [15,16]. For interpolation of the function value in a certain node the authors use only data in the (neighbouring) nodes that fall into the domain of influence of this node. The procedure results in solving a matrix of the size of the number of the nodes in the domain of influence for each nodal point. This paper formulates a meshless two time-level uncoupled radial basis function collocation method for transport phenomena. Its implicit variant overcomes the inherent instability problems encountered in explicit timestepping, used in our previous research.

Governing Equations

Consider a general transport equation defined on fixed domain Ω with boundary Γ , standing for a reasonably broad spectra of mass, energy, momentum and species transfer problems

$$\frac{\partial}{\partial t}[\rho \mathbf{A}(\Phi)] + \nabla \cdot [\rho \mathbf{v} \mathbf{A}(\Phi)] = -\nabla \cdot (-\mathbf{D} \nabla \Phi) + S, \quad (1)$$

with ρ , Φ , t , \mathbf{v} , \mathbf{D} , and S standing for density, transport variable, time, velocity, diffusion tensor and source, respectively. Scalar function \mathbf{A} stands for possible more involved constitutive relations between conserved and diffused quantities. The solution of the governing equation for the transport variable at the final time $t_0 + \Delta t$ is sought, where t_0 represents the initial time and Δt the positive time increment. The solution is constructed by the initial and boundary conditions that follow. The initial value of the transport variable $\Phi(\mathbf{p}, t)$ at point with position vector \mathbf{p} and time t_0 is defined through the known function Φ_0

$$\Phi(\mathbf{p}, t) = \Phi_0(\mathbf{p}); \mathbf{p} \in \Omega + \Gamma. \quad (2)$$

The boundary Γ is divided into not necessarily connected parts $\Gamma = \Gamma_D \cup \Gamma_N \cup \Gamma_R$ with Dirichlet, Neumann and Robin type boundary conditions, respectively. These boundary conditions are at the boundary point \mathbf{p} with normal \mathbf{n}_Γ and time $t_0 \leq t \leq t_0 + \Delta t$ defined through known functions Φ_Γ^D , Φ_Γ^R , $\Phi_{\Gamma_{ref}}^R$

$$\Phi = \Phi_\Gamma^D; \mathbf{p} \in \Gamma_D, \quad \frac{\partial}{\partial n_\Gamma} \Phi = \Phi_\Gamma^N; \mathbf{p} \in \Gamma_N, \quad \frac{\partial}{\partial n_\Gamma} \Phi = \Phi_\Gamma^R (\Phi - \Phi_{\Gamma_{ref}}^R); \mathbf{p} \in \Gamma_R, \quad (3,4,5)$$

Solution Procedure

The involved parameters of the governing equation and boundary conditions are assumed to depend on the transport variable, space and time. The solution procedure thus involves iteration process. Let us assume the two-level time discretisation with the implicitness parameter \mathcal{G} . For $\mathcal{G} = 1$, the scheme is fully implicit and for $\mathcal{G} = 0$, the scheme is fully explicit. The discretisation in time can respectively be written as

$$\frac{\rho \mathbf{A} - \rho_0 \mathbf{A}_0}{\Delta t} + \mathcal{G} \nabla \cdot [\rho \mathbf{v} \mathbf{A}(\Phi)] + (1 - \mathcal{G}) \nabla \cdot [\rho_0 \mathbf{v}_0 \mathbf{A}(\Phi_0)] = -\mathcal{G} \nabla \cdot (-\mathbf{D} \nabla \Phi) - (1 - \mathcal{G}) \nabla \cdot (-\mathbf{D}_0 \nabla \Phi_0) + \mathcal{G} S + (1 - \mathcal{G}) S_0 \quad (6)$$

The nonlinearity of the functions $\mathbf{A}(\Phi)$ and $S(\Phi)$ is treated by the Taylor expansion

$$\mathbf{A}(\Phi) \approx \bar{\mathbf{A}} + \frac{d\bar{\mathbf{A}}}{d\Phi}(\Phi - \bar{\Phi}), \quad S(\Phi) \approx \bar{S} + \frac{d\bar{S}}{d\Phi}(\Phi - \bar{\Phi}). \quad (7,8)$$

The unknown Φ can be calculated from the equation

$$\begin{aligned} & \Phi \left(\frac{\rho}{\Delta t} \frac{d\bar{\mathbf{A}}}{d\Phi} - \mathcal{G} \frac{d\bar{S}}{d\Phi} \right) + \mathcal{G} \nabla \cdot \left(\rho \mathbf{v} \frac{d\bar{\mathbf{A}}}{d\Phi} \Phi \right) - \mathcal{G} (\nabla \cdot \mathbf{D}) \cdot \nabla \Phi - \mathcal{G} \mathbf{D} : [(\nabla^2 \Phi) \mathbf{I}] \\ & = \frac{\rho_0}{\Delta t} \mathbf{A}_0 - \frac{\rho}{\Delta t} \bar{\mathbf{A}} + \frac{\rho}{\Delta t} \frac{d\bar{\mathbf{A}}}{d\Phi} \bar{\Phi} + \mathcal{G} \bar{S} - \mathcal{G} \frac{d\bar{S}}{d\Phi} \bar{\Phi} - \mathcal{G} \nabla \cdot \left[\rho \mathbf{v} \left(\bar{\mathbf{A}} - \frac{d\bar{\mathbf{A}}}{d\Phi} \bar{\Phi} \right) \right] \\ & - (1 - \mathcal{G}) \nabla \cdot (\rho_0 \mathbf{v}_0 \mathbf{A}_0) + (1 - \mathcal{G}) (\nabla \cdot \mathbf{D}_0) \cdot \nabla \Phi_0 + (1 - \mathcal{G}) \mathbf{D}_0 : [(\nabla^2 \Phi_0) \mathbf{I}] + (1 - \mathcal{G}) S_0 \end{aligned} \quad (9)$$

Let us for brevity assume the diffusion tensor to be in the isotropic form $D\mathbf{I}$ with the scalar D (depending on Φ in general) and identity tensor \mathbf{I} in the continuation. The value of the transport variable Φ_n is solved in a set of nodes $\mathbf{p}_n; n = 1, 2, \dots, N$ of which N_Ω belong to the domain and N_Γ to the boundary. The iterations over one timestep are completed

$$\max |\Phi_n - \bar{\Phi}_n| \leq \Phi_{irr}, \quad \max |\Phi_n - \Phi_0| \leq \Phi_{ste}, \quad (10,11)$$

when the equation (10) is satisfied, and the steady-state is achieved when the equation (11) is achieved. The representation of the transport variable over a sub-set of ${}_j N$ arbitrarily spaced nodes ${}_j \mathbf{p}_n; n = 1, 2, \dots, {}_j N$ that fall into subdomain ${}_j \omega$ is made in the following way

$$\Phi(\mathbf{p}) \approx {}_j \psi_k(\mathbf{p}) {}_j \alpha_k, \quad (12)$$

where ${}_l\psi_k$ stands for the shape functions, ${}_l\alpha_k$ for the coefficients of the shape functions, and ${}_lN$ is the number of the shape functions. The Einstein summation convention is used in this text, i.e. any index which is repeated twice in a product is summed-up. An underlined index is not summed-up. Index l runs from 1 to N , and indices k , m and n from 1 to ${}_lN$. The left lower index on entries of expression (12) represents the domain of influence (subdomain) ${}_l\omega$ on which the coefficients ${}_l\alpha_k$ are determined. The domains of influence ${}_l\omega$ can in general be contiguous (overlapping) or non-contiguous (non-overlapping). Each of the domains of influence ${}_l\omega$ includes ${}_lN$ nodes of which ${}_lN_\Omega$ can in general be in the domain and ${}_lN_\Gamma$ on the boundary, i.e. ${}_lN = {}_lN_\Omega + {}_lN_\Gamma$. The domain of influence of the node ${}_l\mathbf{p}$ is defined with the nodes having the nearest ${}_lN-1$ distances to the node ${}_l\mathbf{p}$ in uniform gridpoint arrangements. The coefficients can be calculated from the subdomain nodes in two distinct ways. The first way is collocation (interpolation) and the second way is approximation by the least squares method. Only the simpler collocation version for calculation of the coefficients is considered in this text. Let us assume the known function values ${}_l\Phi_n$ in the nodes ${}_l\mathbf{p}_n$ of the subdomain ${}_l\omega$. The central node of subdomain ${}_l\omega$ is denoted ${}_l\mathbf{p}$. The collocation implies

$$\Phi({}_l\mathbf{p}_n) = {}_l\psi_k({}_l\mathbf{p}_n) {}_l\alpha_k. \quad (13)$$

For the coefficients to be computable, the number of the shape functions has to match the number of the collocation points ${}_lK = {}_lN$, and the collocation matrix has to be non-singular. The system of equations (13) can be written in a matrix-vector notation

$${}_l\underline{\Psi} {}_l\boldsymbol{\alpha} = {}_l\mathbf{\Phi}; \quad {}_l\underline{\Psi}_{kn} = {}_l\psi_k({}_l\mathbf{p}_n), \quad {}_l\mathbf{\Phi}_n = \Phi({}_l\mathbf{p}_n). \quad (14)$$

The coefficients ${}_l\boldsymbol{\alpha}$ can be computed by inverting the system (14)

$${}_l\boldsymbol{\alpha} = {}_l\underline{\Psi}^{-1} {}_l\mathbf{\Phi}. \quad (15)$$

By taking into account the expressions for the calculation of the coefficients ${}_l\boldsymbol{\alpha}$, the collocation representation of transport variable $\Phi(\mathbf{p})$ on subdomain ${}_l\omega$ can be expressed as

$$\Phi(\mathbf{p}) \approx {}_l\psi_k(\mathbf{p}) {}_l\underline{\Psi}_{kn}^{-1} {}_l\mathbf{\Phi}_n = {}_l\underline{\Psi}_n(\mathbf{p}) {}_l\mathbf{\Phi}_n. \quad (16)$$

Let us introduce a two dimensional Cartesian coordinate system with base vectors $\mathbf{i}_\zeta; \zeta = x, y$ and coordinates $p_\zeta; \zeta = x, y$, i.e. $\mathbf{p} = \mathbf{i}_x p_x + \mathbf{i}_y p_y$. The first partial spatial derivatives of $\Phi(\mathbf{p})$ on subdomain ${}_l\omega$ can be expressed as

$$\frac{\partial}{\partial p_\zeta} \Phi(\mathbf{p}) \approx \frac{\partial}{\partial p_\zeta} {}_l\psi_k(\mathbf{p}) {}_l\underline{\Psi}_{kn}^{-1} {}_l\mathbf{\Phi}_n = {}_l\underline{\Psi}_{,\zeta n}(\mathbf{p}) {}_l\mathbf{\Phi}_n; \quad \zeta = x, y. \quad (17)$$

The second partial spatial derivatives of $\Phi(\mathbf{p})$ on subdomain ${}_l\omega$ can be expressed as

$$\frac{\partial^2}{\partial p_\zeta \partial p_\xi} \Phi(\mathbf{p}) \approx \frac{\partial^2}{\partial p_\zeta \partial p_\xi} {}_l\psi_k(\mathbf{p}) {}_l\underline{\Psi}_{kn}^{-1} {}_l\mathbf{\Phi}_n = {}_l\underline{\Psi}_{,\zeta\xi n}(\mathbf{p}) {}_l\mathbf{\Phi}_n; \quad \zeta, \xi = x, y. \quad (18)$$

The radial basis functions, such as multiquadrics, can be used for the shape functions

$${}_l\psi_k(\mathbf{p}) = \left[1 + {}_l c {}_l r_k^2(\mathbf{p}) / {}_l r_0^2 \right]^{1/2}; \quad {}_l r_k^2 = (\mathbf{p} - {}_l\mathbf{p}_k) \cdot (\mathbf{p} - {}_l\mathbf{p}_k), \quad (19)$$

where ${}_l c$ represents the dimensionless shape parameter. The scaling parameter ${}_l r_0^2$ is set to the maximum nodal distance in the domain of influence

$${}_l r_0^2 = \max {}_l r_n^2({}_l\mathbf{p}_k). \quad (20)$$

Let us introduce domain, Dirichlet, Neumann, and Robin boundary indicators for this purpose. These indicators are defined as

$$\Upsilon_{\Omega_m} = \begin{cases} 1; \mathbf{p}_n \in \Omega \\ 0; \mathbf{p}_n \notin \Omega \end{cases}, \quad \Upsilon_{\Gamma_n}^D = \begin{cases} 1; \mathbf{p}_n \in \Gamma^D \\ 0; \mathbf{p}_n \notin \Gamma^D \end{cases}, \quad \Upsilon_{\Gamma_n}^N = \begin{cases} 1; \mathbf{p}_n \in \Gamma^N \\ 0; \mathbf{p}_n \notin \Gamma^N \end{cases}, \quad \Upsilon_{\Gamma_n}^R = \begin{cases} 1; \mathbf{p}_n \in \Gamma^R \\ 0; \mathbf{p}_n \notin \Gamma^R \end{cases}. \quad (21)$$

The unknown values of the transport variable are for each l calculated from the system of linear equations

$$\begin{aligned} & \Upsilon_{\Omega_m} \left[- \left(\frac{\rho}{\Delta t} \frac{d\bar{A}}{d\Phi} - \mathcal{G} \frac{d\bar{S}}{d\Phi} \right) \right] \Psi_k(\mathbf{l}, \mathbf{p}_n) + \mathcal{G}_{\mathbf{l}} \Psi_{,xx}(\mathbf{l}, \mathbf{p}_n) \rho_{\mathbf{k}} v_{x\mathbf{k}} \frac{d\bar{A}}{d\Phi_{\mathbf{k}}} + \mathcal{G}_{\mathbf{l}} \Psi_{,yy}(\mathbf{l}, \mathbf{p}_n) \rho_{\mathbf{k}} v_{y\mathbf{k}} \frac{d\bar{A}}{d\Phi_{\mathbf{k}}} \\ & - \mathcal{G}_{\mathbf{l}} \Psi_{,xm}(\mathbf{l}, \mathbf{p}_n) D_m \Psi_{,xx}(\mathbf{l}, \mathbf{p}_n) - \mathcal{G}_{\mathbf{l}} \Psi_{,ym}(\mathbf{l}, \mathbf{p}_n) D_m \Psi_{,yy}(\mathbf{l}, \mathbf{p}_n) \\ & - \mathcal{G} D_{\mathbf{k}} \Psi_{,xx}(\mathbf{l}, \mathbf{p}_n) - \mathcal{G} D_{\mathbf{k}} \Psi_{,yy}(\mathbf{l}, \mathbf{p}_n) \left] \Phi_k - \Upsilon_{\Gamma_n}^R \mathcal{G}_{\mathbf{l}} \Phi_{\Gamma_n}^R \Psi_k(\mathbf{l}, \mathbf{p}_n) \Phi_k \right. \\ & \left. + \Upsilon_{\Gamma_n}^D \mathcal{G}_{\mathbf{l}} \Psi_k(\mathbf{l}, \mathbf{p}_n) \Phi_k + \Upsilon_{\Gamma_n}^N \mathcal{G} \frac{\partial}{\partial n_{\Gamma}} \Psi_k(\mathbf{l}, \mathbf{p}_n) \Phi_k + \Upsilon_{\Gamma_n}^R \mathcal{G} \frac{\partial}{\partial n_{\Gamma}} \Psi_k(\mathbf{l}, \mathbf{p}_n) \Phi_k \right. \\ & = \Upsilon_{\Omega_m} \left[\left(\frac{\rho_0}{\Delta t} \mathbf{A}_0 - \frac{\rho}{\Delta t} \bar{\mathbf{A}} + \frac{\rho}{\Delta t} \frac{d\bar{\mathbf{A}}}{d\Phi} \bar{\Phi} + \mathcal{G} \bar{S} - \mathcal{G} \frac{d\bar{S}}{d\Phi} \bar{\Phi} \right) \right. \\ & \left. - \mathcal{G}_{\mathbf{l}} \Psi_{,xx}(\mathbf{l}, \mathbf{p}_n) \rho_{\mathbf{k}} v_{x\mathbf{k}} \left(\bar{\mathbf{A}} - \frac{d\bar{\mathbf{A}}}{d\Phi} \bar{\Phi} \right)_{\mathbf{k}} - \mathcal{G}_{\mathbf{l}} \Psi_{,yy}(\mathbf{l}, \mathbf{p}_n) \rho_{\mathbf{k}} v_{y\mathbf{k}} \left(\bar{\mathbf{A}} - \frac{d\bar{\mathbf{A}}}{d\Phi} \bar{\Phi} \right)_{\mathbf{k}} \right] \Phi_k \\ & + \Upsilon_{\Gamma_n}^D \mathcal{G}_{\mathbf{l}} \Phi_n^D + \Upsilon_{\Gamma_n}^N \mathcal{G}_{\mathbf{l}} \Phi_n^N - \Upsilon_{\Gamma_n}^R \mathcal{G}_{\mathbf{l}} \Phi_{\Gamma_n}^R \Phi_{\Gamma_{ref}^R} \\ & - (1 - \mathcal{G}) \left[\mathcal{G}_{\mathbf{l}} \Psi_{,xx}(\mathbf{l}, \mathbf{p}_n) \rho_{0\mathbf{k}} v_{0x\mathbf{k}} \mathbf{A}_{0\mathbf{k}} + \mathcal{G}_{\mathbf{l}} \Psi_{,yy}(\mathbf{l}, \mathbf{p}_n) \rho_{0\mathbf{k}} v_{0y\mathbf{k}} \mathbf{A}_{0\mathbf{k}} \right] \\ & + (1 - \mathcal{G}) \left[\mathcal{G}_{\mathbf{l}} \Psi_{,xm}(\mathbf{l}, \mathbf{p}_n) D_{0m} \Psi_{,xx}(\mathbf{l}, \mathbf{p}_n) + \mathcal{G}_{\mathbf{l}} \Psi_{,ym}(\mathbf{l}, \mathbf{p}_n) D_{0m} \Psi_{,yy}(\mathbf{l}, \mathbf{p}_n) \right. \\ & \left. + D_{0\mathbf{k}} \Psi_{,xx}(\mathbf{l}, \mathbf{p}_n) + D_{0\mathbf{k}} \Psi_{,yy}(\mathbf{l}, \mathbf{p}_n) \right] \Phi_{0\mathbf{k}} + (1 - \mathcal{G}) S_{0m} \end{aligned} \quad (22)$$

The solution procedure requires the following steps: **Step 1:** The matrices ${}_{\mathbf{l}}\Psi_k(\mathbf{l}, \mathbf{p}_n)$, ${}_{\mathbf{l}}\Psi_{k,\gamma\zeta}(\mathbf{l}, \mathbf{p}_n)$, ${}_{\mathbf{l}}\Psi_{k,\gamma\zeta\zeta}(\mathbf{l}, \mathbf{p}_n)$ are pre-calculated. **Step 2:** The initial conditions are set in the domain and boundary nodes and the unknowns ${}_{\mathbf{l}}\Phi_k$ are calculated from the square systems of linear equations (22) of the size ${}_{\mathbf{l}}N$. **Step 3:** The field of Φ_n at time $t_0 + \Delta t$ is set from calculated central node values $\Phi_n = {}_{\mathbf{l}}\Phi_n(\mathbf{l}, \mathbf{p})$. **Step 4:** Timestep iteration and steady-state checks (10,11) are performed. **Step 5:** New timestep values of the present timestep are set to the old timestep values of the next timestep and the new timestep is attempted.

Example of Solution Procedure for Darcy Porous Media Flow and Navier - Stokes equations.

The solution of Darcy porous media flow (DP) and Navier - Stokes (NS) flow in the context of developed method for steady natural convection is represented in the following form. Governing equations are: mass conservation, DP or NS momentum conservation, and energy conservation:

$$\nabla \cdot \mathbf{v} = 0, \quad \text{DP: } 0 = -\nabla P - \frac{\mu}{K} \mathbf{v} + \mathbf{f}, \quad \text{NS: } \nabla \cdot (\rho \mathbf{v} \mathbf{v}) = -\nabla P + \mu \nabla^2 \mathbf{v} + \mathbf{f}, \quad \rho c_p \mathbf{\bar{\nu}} \cdot (\mathbf{v} T) = k \nabla^2 T \quad (23)$$

with \mathbf{v} representing velocity, μ viscosity, k permeability and \mathbf{f} the Bussinesq body force $\mathbf{f} = \tilde{n} \mathbf{a} [1 - \beta(T - T_{ref})]$, and c_p for heat capacity with T and T_{ref} standing for temperature and reference temperature, \mathbf{a} for acceleration and β for thermal expansion. Boundary conditions are in the case of DF of the impermeable type $\mathbf{v} \cdot \mathbf{n}_{\Gamma} = 0$; $\mathbf{p} \in \Gamma$, and in the case of NS equations of the impermeable and no-slip type $\mathbf{v} \cdot \mathbf{n}^{\Gamma} = 0$; $\mathbf{p} \in \Gamma$. The boundary conditions for the energy equation are of the Dirichlet and Neumann

type $T = T_r$; $\mathbf{p} \in \Gamma_D$, $-k \frac{\partial T}{\partial n_\Gamma} = F_r$; $\mathbf{p} \in \Gamma_N$. The Pressure is calculated from the pressure Poisson equation, for $t \rightarrow \infty$:

$$\text{DP: } \frac{\partial P^{j+1}}{\partial t} + \nabla^2 P^{j+1} = \nabla \cdot \left(-\frac{\mu}{K} \mathbf{v}^j + \mathbf{f}^j \right), \quad \text{NS: } \frac{\partial P^{j+1}}{\partial t} + \nabla^2 P^{j+1} = \nabla \cdot \left(-\nabla \cdot (\rho \mathbf{v}^j \mathbf{v}^j) + \mu \nabla^2 \mathbf{v} + \mathbf{f} \right) \quad (24)$$

with the pressure Poisson boundary conditions:

$$\text{DP: } \frac{\partial P^{j+1}}{\partial n_\Gamma} = \mathbf{f}^j \cdot \mathbf{n}_\Gamma; \quad \mathbf{p} \in \Gamma, \quad \text{NS: } \frac{\partial P^{j+1}}{\partial n_\Gamma} = (-\nabla \cdot (\rho \mathbf{v}^j \mathbf{v}^j) + \mu \nabla^2 \mathbf{v}^j + \mathbf{f}^j) \cdot \mathbf{n}_\Gamma; \quad \mathbf{p} \in \Gamma, \quad (25)$$

Where the pressure needs to be defined at least in one domain or boundary point: $P_m^{j+1} = P_{ref}$; $\mathbf{p} = \mathbf{p}_{ref}$. Velocity is calculated as:

$$\text{DP: } \hat{\mathbf{v}}^{j+1} = \frac{K}{\mu} (-\nabla P^{j+1} + \mathbf{f}^j), \quad \text{NS: } \nabla^2 \hat{\mathbf{v}}^{j+1} = \frac{1}{\mu} (\nabla P^{j+1} + \nabla \cdot (\rho \mathbf{v}^j \mathbf{v}^j) - \mathbf{f}^j). \quad (26)$$

Since the velocity $\hat{\mathbf{v}}^{j+1}$ does not correspond to the mass conservation (in general) it is corrected by the velocity correction $\nabla \cdot \mathbf{v}^{j+1} = \nabla \cdot (\hat{\mathbf{v}}^{j+1} + \check{\mathbf{v}}^{j+1}) = 0$. The velocity correction is assumed to be a function of the pressure correction

$$\text{DP: } c_{rel}^P \frac{\mu}{K} \check{\mathbf{v}}^{j+1} = -\nabla \check{P}^{j+1}, \quad \nabla^2 \check{P}^{j+1} = c_{rel}^P \frac{\mu}{K} \nabla \cdot \hat{\mathbf{v}}^{j+1}, \quad \text{NS: } c_{rel}^P \frac{\rho}{\Delta t} \check{\mathbf{v}}^{j+1} = -\nabla \check{P}^{j+1}, \quad \nabla^2 \check{P}^{j+1} = c_{rel}^P \frac{\rho}{\Delta t} \nabla \cdot \hat{\mathbf{v}}^{j+1} \quad (27)$$

and the respective pressure correction Poisson equation is formulated, with the boundary conditions $\partial \check{P}^{j+1} / \partial n_\Gamma = 0$; $\mathbf{p} \in \Gamma$. The Pressure correction is calculated from the pressure correction Poisson equation, for $t \rightarrow \infty$:

$$\text{DP: } \frac{\partial \check{P}^{j+1}}{\partial t} + \nabla^2 \check{P}^{j+1} = \nabla \cdot \left(-\frac{\mu}{K} \mathbf{v}^j + \mathbf{f}^j \right), \quad \text{NS: } \frac{\partial \check{P}^{j+1}}{\partial t} + \nabla^2 \check{P}^{j+1} = \nabla \cdot \left(-\nabla \cdot (\rho \mathbf{v}^j \mathbf{v}^j) + \mu \nabla^2 \mathbf{v}^j + \mathbf{f}^j \right). \quad (28)$$

The steady-state temperature field is calculated from the diffusion equation for $t \rightarrow \infty$

$$\rho c_p \frac{\partial T^{j+1}}{\partial t} - k \nabla^2 T^{j+1} = -\rho c_p \nabla \cdot (\mathbf{v}^{j+1} T^{j+1}), \quad (29)$$

and the body force is updated as $\mathbf{f}^{j+1} = \rho \mathbf{a} [1 - \beta (T^{j+1} - T_{ref})]$. Iteration $j + 2$ is attempted next.

Conclusions

This paper represents a new simple meshfree formulation for solving a wide range of nonlinear transport phenomena. The time-marching might be performed in an implicit or explicit two time-level way. The governing equation is solved in its strong form. No polygonisation and no integration is needed. The developments are almost independent on the problem dimension. The complicated geometry is easy to cope with. The method appears efficient, because it does not require a solution of a large system of equations like the original Kansa method. Instead, small systems of linear equations have to be solved in each timestep for each node and associated domain of influence, probably representing the most natural and automatic domain decomposition. This feature of the developed method represents its principal difference from the other related local approaches [17], where the resultant matrix is large and sparse. The method requires the same computational effort for any timestep parameter \mathcal{G} . The fully explicit version of the represented method has been already used in temperature field model of the DC casting [18] and twin-roll casting of aluminium alloys [19]. Several other numerical examples will be shown at the conference.

References

- [1] S.N. Atluri and S. Shen, *The Meshless Method*, Tech Science Press, Forsyth (2002).
- [2] G.R. Liu, *Mesh Free Methods*, CRC Press, Boca Raton (2003).

- [3] S.N. Atluri, *The Meshless Method for Domain and BIE Discretisations*, Tech Science Press, Forsyth (2004).
- [4] G.R. Liu and Y.T. Gu, *An Introduction to Meshfree Methods and Their Programming*, Springer-Verlag, Berlin (2005).
- [5] B. Šarler, Chapter 9: Meshless Methods, In: *Advanced Numerical Methods in Heat Transfer*, (Edited by Nowak, A.J.), Silesian Technical University Press, Gliwice, 225-247 (2004).
- [6] M.D. Buhmann, *Radial Basis Function: Theory and Implementations*, Cambridge University Press, Cambridge (2003).
- [7] E.J. Kansa, Multiquadrics – a scattered data approximation scheme with applications to computational fluid dynamics-II. Solutions to parabolic, hyperbolic and elliptic partial differential equations, *Computers and Mathematics with Application*, **19**, 147-161 (1990).
- [8] G.E. Fasshauer, Solving partial differential equations by collocation with radial basis functions, (Edited by A.L. Mehaute, C. Rabut and L.L. Schumaker), *Surface Fitting and Multiresolution Methods*, 131-138 (1997).
- [9] W. Chen, New RBF collocation schemes and kernel RBFs with applications, *Lecture Notes in Computational Science and Engineering*, **26**, 75-86 (2002).
- [10] N. Mai-Duy and T. Tran-Cong, Indirect RBFN method with thin plate splines for numerical solution of differential equations, *Computer Modeling in Engineering & Sciences*, **4**, 85-102 (2003).
- [11] B. Šarler, A radial basis function collocation approach in computational fluid dynamics, *Computer Modeling in Engineering & Sciences*, **7**, 185-194 (2005).
- [12] B. Šarler, J. Perko and C.S. Chen, Radial basis function collocation method solution of natural convection in porous media, *Int.J.Numer.Methods Heat & Fluid Flow*, **14**, 187-212 (2004).
- [13] I. Kovačević, A. Poredoš and B. Šarler, Solving the Stefan problem by the RBFCM, *Numer.Heat Transfer, Part B: Fundamentals* **44**, 1-24 (2003).
- [14] N. Mai-Duy and T. Tran-Cong, Mesh-free radial basis function network methods with domain decomposition for approximation of functions and numerical solution of Poisson's equations, *Engineering Analysis with Boundary Elements* **26**, 133-156 (2002).
- [15] B. Šarler and R.Vertnik, Meshfree explicit local radial basis function collocation method for diffusion problems, *Computers and Mathematics with Applications* (2005), in print.
- [16] R. Vertnik and B.Šarler, Meshless local radial basis function collocation method for convective-diffusive solid-liquid phase change problems, *Int.J.Numer.Methods Heat & Fluid Flow* (2005), in print.
- [17] A.I. Tolstykh and D.A. Shirobokov, Using radial basis functions in a “finite difference mode”, *Computer Modeling in Engineering & Sciences*, **7**, 207-222 (2005).
- [18] R. Vertnik, M.Založnik and B. Šarler, Solution of transient direct chill aluminium casting problem with simultaneous material and interphase moving boundaries by a meshless method, *Engineering Analysis with Boundary Elements* (2006), in print.
- [18] B. Šarler, S.Šaletić and R. Vertnik, Solution of the thermal model of the twin-roll casting process by the meshless local radial basis function collocation technique, (Edited by M. Papadrakakis, E. Oñate, B. Schrefler), *Computational Methods for Coupled Problems in Science and Engineering*, CIMNE, Barcelona, 101-110 (2005).

Dual Reciprocity Boundary Element Analysis of Steady-state Heat Conduction in Nonlinear Anisotropic Materials

Krishna M. Singh¹ and Masataka Tanaka²

¹Dept. of Mechanical & Ind. Engg., IIT Roorkee, Roorkee – 247667, India. E-mail: singhfme@iitr.ernet.in

²Dept. of Mechanical Systems Engg., Shinshu University, 4-17-1 Wakasato, Nagano 380-8553, Japan.

E-mail: dtanaka@gipwc.shinshu-u.ac.jp

Keywords: Anisotropic heat conduction; Boundary element method; Dual reciprocity method; Nonlinear conduction

Abstract This paper presents a dual reciprocity boundary element formulation for heat conduction in a nonlinear anisotropic medium with temperature dependent thermal conductivity based on the Fundamental solution of Laplace equation. The radial basis interpolation has also been used for approximation of the spatial derivatives of the temperature involved in the source term. The choice of approximation for the second order derivative of the temperature leads to two formulations whose performance has been investigated in conjunction with a set of higher order radial basis functions. Boundary element results have been compared with the finite element solution to assess the performance of the dual reciprocity formulations and radial basis functions.

1 Introduction

Most of the commonly used anisotropic materials exhibit a strong temperature dependence for material properties. Hence, the thermo-mechanical simulation of these systems in design analysis must be based on nonlinear material models. These nonlinear models result in nonlinear partial differential systems which must be solved numerically. The finite element techniques have been most commonly used for numerical simulation of these nonlinear anisotropic problems. In contrast, boundary element methods have been mostly applied to nonlinear isotropic problems and linear anisotropic problems.

In the case of isotropic problems, boundary element techniques have emerged as a powerful alternative to the finite element techniques. Although these techniques were initially thought as a viable alternative only for linear homogeneous problems, the introduction of the dual reciprocity method (DRM) by Nardini and Brebbia [1] in 1982 has significantly altered this view. Since then the dual reciprocity boundary element method has been applied to a variety of linear and nonlinear problems [2, 3, 4].

Boundary element research related to anisotropic problems has been mostly focused on linear elasticity and coupled linear thermo-elastic problems [2, 5]. Heat conduction analysis in the coupled problems has been performed with a formulation based on the use of anisotropic fundamental solution [5, 6]. This formulation, though very elegant, is limited to linear homogeneous anisotropic problem. For non-homogeneous and/or nonlinear anisotropic problems, one has to resort to the dual reciprocity method to handle the volume integrals arising from the source term introduced to model the problem using the fundamental solution of the linear homogeneous operator. We can devise an even simpler approach by casting the governing equation as Poisson equation in which the source term includes the effects of anisotropy, inhomogeneity and nonlinearity. The dual reciprocity method can then be used to model the effect of the source term. This approach was initially used by Partridge [7, 8] for linear orthotropic heat conduction. Building on this approach, Singh *et al.* [9] have recently developed and applied the dual reciprocity formulation to the steady state heat conduction in linear homogeneous anisotropic medium. Objective of the present work is to extend this approach further and develop boundary element formulations for heat conduction in nonlinear homogeneous anisotropic medium. In the sequel, we present the dual reciprocity formulation proposed in this work, numerical results and conclusions.

2 Dual reciprocity boundary element formulation

The steady state heat conduction in a homogeneous anisotropic domain Ω with temperature dependent thermal conductivity is governed by the field equation

$$[\lambda_{ij}(u)u_{,j}]_{,i} + q_g = 0 \quad \text{in } \bar{\Omega}, \quad (1)$$

with associated boundary conditions. In the preceding equation, q_g is the heat generation, and λ_{ij} is the conductivity tensor which is assumed to symmetric and positive definite so that eq. (1) is elliptic. In the preceding equation as well as the rest of the paper, standard summation convention holds for repeated indices unless otherwise specified, and the comma operator denotes partial differentiation with respect the coordinate variable specified by the following index.

For dual reciprocity formulation, we first transform eq. (1) into a Poisson equation. For this purpose, we introduce a modified conductivity tensor k_{ij} given by

$$k_{ij}(u) = (\lambda_{ij}(u) - \lambda_0 \delta_{ij}) / \lambda_0, \quad (2)$$

where λ_0 is a scalar constant, and δ_{ij} denotes Kronecker delta function. Using eq. (2), we can rewrite eq. (1) as Poisson equation

$$\nabla^2 u = b(\mathbf{x}, u) \quad \text{where} \quad b(\mathbf{x}, u) = -q_g / \lambda_0 - [k_{ij}(u)u_{,j}]_{,i}. \quad (3)$$

We can now use the standard product-type approximation for b using radial basis functions $f^j(\mathbf{x})$ given by [4]

$$b(\mathbf{x}, u) \approx \sum_{j=1}^{N+L} f^j(\mathbf{x}) \alpha^j, \quad (4)$$

where α^j are unknown coefficients, and N and L denote the number of boundary and internal collocation points, respectively. Functions $f^j(\mathbf{x})$ are so chosen that we can easily find $\hat{u}^j(\mathbf{x})$ satisfying $\nabla^2 \hat{u}^j = f^j$. Use of approximation (4) in conjunction with direct boundary element formulation transforms eq. (3) into the following boundary integral equation:

$$c_i u_i + \int_{\Gamma} (q^* u - u^* q^I) d\Gamma = \sum_{j=1}^{N+L} \left[c_i \hat{u}_i^j + \int_{\Gamma} (q^* \hat{u}^j - u^* \hat{q}^j) d\Gamma \right] \alpha^j, \quad (5)$$

where $q^I = \partial u / \partial n$, and $\hat{q}^j = \partial \hat{u}^j / \partial n$. Use of the standard boundary element discretization procedure [4] leads to the following algebraic system:

$$\mathbf{H} \mathbf{u} - \mathbf{G} \mathbf{q}^I = (\mathbf{H} \hat{\mathbf{U}} - \mathbf{G} \hat{\mathbf{Q}}) \mathbf{F}^{-1} \mathbf{b}. \quad (6)$$

where \mathbf{H} and \mathbf{G} are the global matrices of boundary integrals with kernels q^* and u^* , respectively; \mathbf{u} , \mathbf{q}^I and \mathbf{b} denote global nodal vectors of u , q^I and b ; \mathbf{F} , $\hat{\mathbf{U}}$ and $\hat{\mathbf{Q}}$ are the coordinate function matrices with their columns as the nodal vectors $\mathbf{f}^j \hat{\mathbf{u}}^j$ and $\hat{\mathbf{q}}^j$ respectively.

We need to substitute the expressions for \mathbf{b} and \mathbf{q}^I in terms of \mathbf{u} and \mathbf{q} to obtain the final algebraic system. To express \mathbf{b} in matrix form, we introduce diagonal matrices \mathbf{R}^{rs} and \mathbf{S}^{rs} defined as

$$R_{ij}^{rs} = k_{rs}(u_i) \delta_{ij}, \quad S_{ij}^{rs} = \frac{\partial k_{rs}}{\partial x_r} \delta_{ij} = \left(\frac{\partial k_{rs}}{\partial u} \frac{\partial u}{\partial x_r} \right) (\mathbf{x}_i) \delta_{ij}. \quad (7)$$

Using the preceding definitions, \mathbf{b} can be expressed as

$$\mathbf{b} = -\mathbf{q}_g / \lambda_0 - (\mathbf{S}^{rs} \mathbf{u}_{,s} + \mathbf{R}^{rs} \mathbf{u}_{,rs}). \quad (8)$$

To obtain an expression for the derivatives of \mathbf{u} involved in the definition of \mathbf{b} , we can again use the approximation similar to eq. (4) for u and thereby obtain [4]

$$\mathbf{u} = \mathbf{F} \boldsymbol{\beta} \quad \implies \boldsymbol{\beta} = \mathbf{F}^{-1} \mathbf{u}, \quad (9)$$

where $\beta \neq \alpha$. Differentiation of the preceding equation and substitution for β yields

$$\mathbf{u}_{,r} = \mathbf{F}_{,r} \mathbf{F}^{-1} \mathbf{u}, \quad \mathbf{u}_{,rs} = \mathbf{F}_{,rs} \mathbf{F}^{-1} \mathbf{u}. \tag{10}$$

An alternative expression for the second derivatives can be obtained by using the radial basis approximation for the first derivative which can be expressed as

$$\mathbf{u}_{,r} = \mathbf{F} \boldsymbol{\gamma} \quad (\boldsymbol{\gamma} \neq \beta \neq \boldsymbol{\alpha}) \quad \implies \quad \mathbf{u}_{,rs} = \mathbf{F}_{,s} \mathbf{F}^{-1} \mathbf{F}_{,r} \mathbf{F}^{-1} \mathbf{u}. \tag{11}$$

Substituting expressions for derivatives of \mathbf{u} into eq. (8), we obtain

$$\mathbf{b} = -\frac{\mathbf{q}\mathbf{g}}{\lambda_0} - \left(\mathbf{S}^{rs} \mathbf{F}_{,s} + \mathbf{R}^{rs} \mathbf{F}_{,rs}'' \right) \mathbf{F}^{-1} \mathbf{u}. \tag{12}$$

In the preceding equation, and $\mathbf{F}_{,rs}''$ is either $\mathbf{F}_{,rs}$ or $\mathbf{F}_{,s} \mathbf{F}^{-1} \mathbf{F}_{,r}$ depending on whether eq. (10) or eq. (11) has been used for the second derivative.

Let us note that the heat flux for an anisotropic medium is given by

$$q = \lambda_{ij} u_{,j} n_i = \lambda_0 k_{ij} u_{,j} n_i + \lambda_0 u_{,i} n_i \quad \implies \quad q^I = \frac{q}{\lambda_0} - k_{ij} u_{,j} n_i. \tag{13}$$

Let us introduce diagonal matrices \mathbf{A}^s defined by $A_{ij}^s = (k_{rs} n_r)(\mathbf{x}_i) \delta_{ij}$, which leads to

$$\mathbf{q}^I = \frac{\mathbf{q}}{\lambda_0} - \mathbf{A}^s \mathbf{F}_{,s} \mathbf{F}^{-1} \mathbf{u}. \tag{14}$$

Substituting eq. (12) and eq. (14) into eq. (6), we obtain the following nonlinear algebraic equation:

$$\boldsymbol{\Phi}(\mathbf{z}) \equiv \mathbf{H} \mathbf{u} + \mathbf{M}(\mathbf{u}) \mathbf{u} - \frac{1}{\lambda_0} \mathbf{G} \mathbf{q} - \frac{1}{\lambda_0} \mathbf{C} \mathbf{q} \mathbf{g} = 0, \tag{15}$$

where $\boldsymbol{\Phi}(\mathbf{z})$ denotes the system of equations with \mathbf{z} representing the nodal unknowns (u or q), $\mathbf{C} = (\mathbf{G} \hat{\mathbf{Q}} - \mathbf{H} \hat{\mathbf{U}}) \mathbf{F}^{-1}$, and matrix \mathbf{M} is given by

$$\mathbf{M} = \mathbf{G} \mathbf{A}^s \mathbf{F}_{,s} \mathbf{F}^{-1} - \mathbf{C} (\mathbf{S}^{rs} \mathbf{F}_{,s} + \mathbf{R}^{rs} \mathbf{F}_{,rs}'') \mathbf{F}^{-1}. \tag{16}$$

We would use the term DRM1 to denote the dual reciprocity formulation based on the first order derivatives of \mathbf{F} , and DRM2 to denote that based on second order derivatives of \mathbf{F} for the approximation of $\mathbf{u}_{,rs}$. Further, we have employed the following set of radial basis functions in numerical experiments:

Type description	Abbreviation	$f^j(\mathbf{x})$
<u>Polynomials</u>		
Second order	RB2	$1 + r + r^2$
Third order	RB3	$1 + r + r^2 + r^3$
<u>Thin-plate splines</u>		
Second order (augmented)	TP2	$r^2 \log r + r + 1$
Fourth order	TP3	$r^4 \log r$
Fourth order(augmented)	TP4	$r^4 \log r + r^3 + r^2 + r + 1$
CS-RBF of Wendland [10]	CSR	$(1 - r)_+^4 (4r + 1)$

3 Numerical results

To assess the performance of the dual reciprocity formulation for nonlinear anisotropic heat conduction problems, we have applied it to a set of test problems. We include herein the results with two representative problems. The first one is essentially an isotropic problem with known exact solution which has been modeled as an orthotropic problem for initial testing. The second one is an anisotropic problem.

All the computations have been performed in double precision arithmetic using a nonlinear solver based on globally convergent Newton's method [11] and LAPACK routines [12] for linear algebra. Initial guess has been provided by the solution of the linearized system. For convergence check, we have used the tolerances FTOL = 10^{-14} for function values, and XTOL = 10^{-12} for incremental correction of the solution vector. Quadratic boundary elements, with partially discontinuous elements at the corners, have been used for the discretization of the boundary.

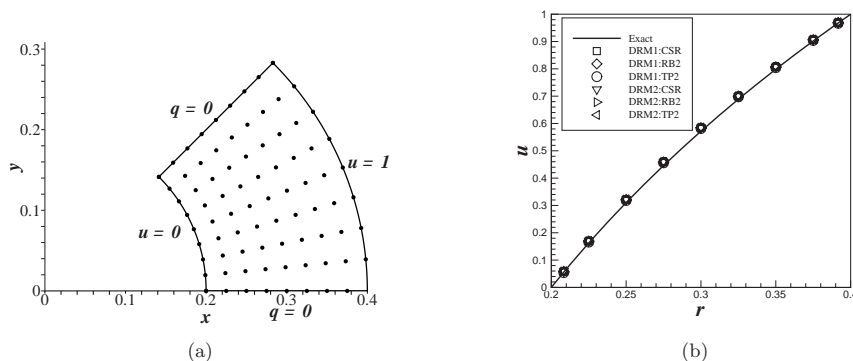


Figure 1: Isotropic nonlinear problem in a thick cylinder: (a) geometry, boundary conditions and discretization; (b) temperatures along x -axis obtained with DRM1 and DRM2. (For clarity, results with only three RBFs are included; results with others are very similar.)

Table 1: Isotropic nonlinear problem: Heat flux values at $\theta = 22.5^\circ$. At inner surface ($r = 0.2$), $q_{\text{exact}} = -6.8419$; at outer surface ($r = 0.4$), $q_{\text{exact}} = 3.6598$. Figures in the parentheses denote the relative error.

RBF	At inner surface ($r = 0.2$)		At outer surface ($r = 0.4$)	
	DRM1	DRM2	DRM1	DRM2
CSR	-7.213 (5.43%)	-7.213 (5.43%)	3.607 (1.45%)	3.607 (1.45%)
RB2	-7.213 (5.43%)	-7.214 (5.44%)	3.607 (1.45%)	3.608 (1.42%)
TP2	-7.218 (5.49%)	-7.214 (5.43%)	3.606 (1.46%)	3.608 (1.41%)
TP3	-7.215 (5.45%)	-7.213 (5.43%)	3.606 (1.48%)	3.607 (1.45%)
TP4	-7.213 (5.43%)	-7.214 (5.43%)	3.607 (1.45%)	3.608 (1.42%)

3.1 Nonlinear isotropic conduction in a thick cylinder

Let us consider a long thick-walled circular cylinder made of a homogeneous isotropic material. The inner and outer surfaces are held at constant temperatures of 0 and 100 degrees respectively. For the thermal analysis, we have selected an angular sector of 45° . Figure 1(a) shows the geometry, boundary conditions (in non-dimensional form) and discretization of the problem domain. This problem has been modeled as an *orthotropic* heat conduction problem. The variation of the thermal conductivity tensor with temperature is given by

$$\lambda_{ij} = (a_i + b_i u + c_i u^2) \delta_{ij}, \quad (17)$$

where $a_i = 1$, $b_i = -0.10326$, $c_i = 3.39 \times 10^{-4}$ for $i = 1, 2$. Exact solution can be easily obtained using Kirchhoff transform.

Numerical temperature values obtained by using either of the dual reciprocity formulations (DRM1 or DRM2) and any of the radial basis functions are almost identical and very accurate as can be seen from Figure 1(b). Heat flux values at inner and outer surfaces are presented in Table 1. Flux results are also very accurate. These are within 5.5% and 1.4% of the exact values at the inner and outer surfaces respectively.

3.2 Nonlinear anisotropic problem

We again consider the heat conduction problem on the annular sector shown in Figure 1(a). However, the material is anisotropic and the variation of the thermal conductivity tensor with temperature is

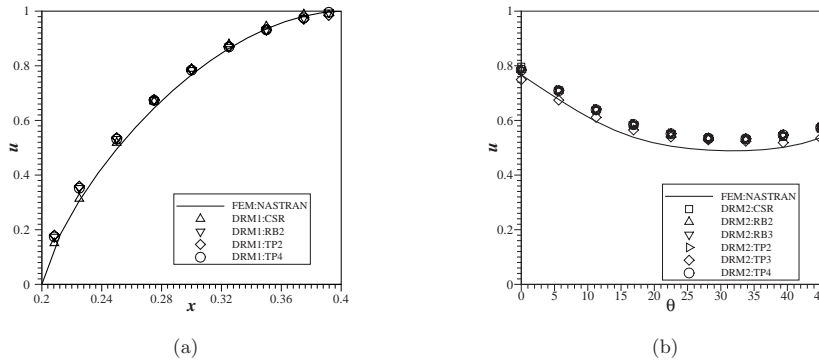


Figure 2: Nonlinear anisotropic problem: (a) temperatures on boundary along x -axis, (b) temperatures at interior points along $r = 0.3$.

given by

$$\lambda_{ij} = k_{ij}^0(a + bu), \quad (18)$$

where $a = 1$, $b_1 = -0.3$, $k_{11}^0 = 45$, $k_{12}^0 = 25$, and $k_{22}^0 = 35$. DRM results have been compared with the finite element results obtained using NASTRAN with 256 linear quadrilateral elements.

Figure 2 presents temperature results. Excellent agreement with the finite element solution can be observed for the results obtained with either of the dual reciprocity formulations (DRM1 or DRM2) and any of the radial basis functions. Flux values along the outer boundary ($r = 0.4$) (not included here due to space constraints) show that (a) results with DRM1 are more accurate than those with DRM2, (b) there is considerable scatter in the results obtained with the radial basis functions CSR, TP2 and TP3, and (c) the results with rest of the radial basis functions show excellent agreement with the finite element solution.

The preceding examples clearly demonstrate that both the dual reciprocity formulations can be used for accurate simulation of nonlinear anisotropic problems. Of the two formulations considered herein, DRM1 seems to yield more accurate results than DRM2. Amongst the radial basis functions, RB2 and TP4 seem to be the most robust choices.

4 Conclusions

We have presented a dual reciprocity boundary element formulation for heat conduction in a nonlinear anisotropic medium with temperature dependent thermal conductivity. Heat conduction equation has been re-cast into a Poisson equation with a nonlinear source term. Fundamental solution of Laplace equation has been used for boundary element formulation in conjunction with the dual reciprocity approximation of the nonlinear source term. The derivatives of the temperature occurring in the source term have also been approximated using radial basis interpolation. There are two options for the approximation of the second order derivative of the temperature — one based on the first order spatial derivatives and the other based on the second order derivatives of the radial basis functions. These choices result in two formulations denoted by DRM1 and DRM2 respectively. We have employed a set of higher order radial basis functions in view of the regularity requirements of the derivatives. Numerical experiments have been performed with an isotropic (modelled as orthotropic) nonlinear problem with exact solution and a nonlinear anisotropic problem. Boundary element results for these examples have been compared with the finite element solutions obtained with NASTRAN to assess the accuracy of the dual reciprocity formulations and the radial basis functions. Both the formulations yield very accurate results, with DRM1 being more accurate than DRM2. Amongst the radial basis

functions, the second order polynomial RB2 and the augmented thin-plate spline TP4 seem to be the most robust performers.

Acknowledgements

Part of this work was financially supported by the Ministry of Education, Science, Sports and Culture, Japan, Grant-in-Aid for Scientific Research (C), No. 16560066, 2005, granted to the author (MT). This financial support is gratefully acknowledged.

References

- [1] D. Nardini and C. A. Brebbia. A new approach to free vibration analysis using boundary elements. In C. A. Brebbia, editor, *Boundary Elements IV*, pages 312–326. Springer-Verlag, Berlin, 1982.
- [2] M. Kügl. *A Boundary Element Method for Dynamics Analysis of Anisotropic Elastic, Piezoelectric, and Thermoelastic Solids*. PhD thesis, University of Stuttgart, Stuttgart, Germany, 2000.
- [3] L. C. Wrobel and C. A. Brebbia. The dual reciprocity boundary element formulation for nonlinear diffusion problems. *Computer Methods in Applied Mechanics and Engineering*, 65:147–164, 1987.
- [4] P. W. Partridge, C. A. Brebbia, and L. C. Wrobel. *The Dual Reciprocity Boundary Element Method*. Computational Mechanics Publications, Southampton and Elsevier Applied Science, London, 1991.
- [5] M. Kügl and L. Gaul. Generalized body forces in multi-field problems with material anisotropy. In Y. F. Rashed and C. A. Brebbia, editors, *Transformation of Domain Effects to the Boundary*, chapter 6, pages 121–153. WIT Press, Southampton, 2003.
- [6] J. T. Katsikadelis. *Boundary Elements: Theory and Applications*. Elsevier Science Ltd., Oxford, UK, 2002.
- [7] P. W. Partridge. Radial basis approximation functions in the boundary element dual reciprocity method. In *BETECH99*. Computational Mechanics Publications, Southampton, 1999.
- [8] P. W. Partridge. Towards criterion for selecting approximation functions in the dual reciprocity boundary element method. *Engineering Analysis with Boundary Elements*, 24:519–529, 2000.
- [9] K. M. Singh, M. Tanaka, and K. Hara. Dual reciprocity boundary element analysis of anisotropic heat conduction. *Computer Methods in Applied Mechanics and Engineering*, 2005. (submitted).
- [10] H. Wendland. Piecewise polynomial, positive definite radial functions of minimal degree. *Advance in Computational Mathematics*, 4:389–396, 1995.
- [11] William H. Press, Saul A. Teukolsky, William T. Vetterling, and Brian P. Flannery. *Numerical Recipes in FORTRAN*. Cambridge University Press, Cambridge, 2nd edition, 1992.
- [12] E. Anderson, Z. Bai, C. Bischof, J. Demmel, J. Dongarra, J. Du Croz, A. Greenbaum, S. Hammarling, A. McKenney, S. Ostrouchov, and D. Sorensen. *LAPACK Users' Guide*. SIAM, Philadelphia, second edition, 1994.

Cracked Orthotropic Strip Dynamic Analysis by Displacement Discontinuity Method

P. H. Wen ¹, M. H. Aliabadi ², J. Sladek³ and V. Sladek ³

¹Department of Engineering, Queen Mary, London University, London, E1 4NS, UK

²Department of Aeronautics, Imperial College London, Prince Consort Road, South Kensington Campus, London, SW7 2BY, United Kingdom

³Institute of Construction and Architecture, Slovak Academy of Sciences, 845 03 Bratislava, Slovakia

Abstract An integral equation method, displacement discontinuity method, is presented for elastodynamic response of an orthotropic strip with straight cracks under impact loads. Dynamic Green's function for mode I displacement discontinuity is derived for an orthotropic strip using the Fourier transform method in the Laplace transform domain. The time domain dynamic stress intensity factors at the crack tip are obtained directly by these coefficients of the Chebyshev polynomials along with the Durbin's Laplace transform inversion method.

1 Introduction

Material anisotropy may occur in many engineering materials, such as fiber-reinforced composites and laminates, which are ideal for aircraft structural applications where high strength-to-weight and stiffness-to-weight ratios are required. Elastodynamic analysis for cracked anisotropic components is of particular interest to quantitative non-destructive material testing by ultrasonics. In advanced experimental solid mechanics, the measurement of travel time from crack tips can be used to detect the location of defects/ flaws in the components of structure. Although there are some closed form solutions for stationary and propagations cracks in isotropic material under dynamic loads [1] [2], there are very few closed form solutions for cracked anisotropic bodies. For the dynamic isotropy, most of these researches reduce the problems to a Fredholm integral equation in the Laplace transform domain and obtain the solution in time domain using different numerical Laplace inversion. For example, a closed form solution for semi-infinite crack under uniform dynamic load on the crack surfaces was presented in [2][3] for mixed modes of fracture.

In this paper, a Green's function for a discontinuity displacement in an orthotropic medium strip is derived in a form of the finite integral with boundary influence function

in the Laplace transform domain. As this Green's function is of hypersingularity in the sense of Hadamard finite-part integrals, the Chebyshev polynomials of the second kind need to be employed to evaluate the integral equation in the transformed domain. The transformed stress intensity factors are able to be determined directly from the coefficients of Chebyshev polynomials. The effect of elasticity waves on the normal stress and stress intensity factors is investigated for a straight cracked orthotropic strip.

2 Green's function in Laplace transform domain

Differential equations of equilibrium for two dimensional problem can be written as

$$\begin{aligned} c_{11} \frac{\partial^2 u}{\partial x^2} + \frac{\partial^2 u}{\partial y^2} + (1 + c_{12}) \frac{\partial^2 v}{\partial x \partial y} &= \frac{1}{c_s^2} \frac{\partial^2 u}{\partial t^2}, \\ \frac{\partial^2 v}{\partial x^2} + c_{22} \frac{\partial^2 v}{\partial y^2} + (1 + c_{12}) \frac{\partial^2 u}{\partial x \partial y} &= \frac{1}{c_s^2} \frac{\partial^2 v}{\partial t^2} \end{aligned} \quad (1)$$

where c_{11} , c_{12} and c_{22} are non-dimensional parameters, $c_s^2 (= \mu_{12}/\rho)$ represents the velocity of the in-plane shear wave propagating along the principal material axes and ρ is the mass density. Considering the conditions for opening mode displacement discontinuity along axis x at origin

$$\begin{aligned} v(x, 0, t) &= [v^+ - v^-]/2 = \delta(x)\delta(t), \quad \tau_{xy}(x, 0, t) = 0 \\ \sigma_{yy}(x, h, t) &= 0; \quad \tau_{xy}(x, h, t) = 0 \end{aligned} \quad (2)$$

where $[v^+ - v^-]$ presents the displacement discontinuity. Since only straight opening mode crack along the axis x is considered in this paper, the Green's function $Y(x, p) = \sigma_y^*(x, 0, p)$ can be presented as

$$\begin{aligned} Y(x, p) &= \frac{2\mu_{12}}{\pi} \lim_{y \rightarrow 0} \sum_{i=1}^4 \int_0^\infty \omega (c_{12} + c_{22} \lambda_i^0 \beta_i) A_i(\omega, p) e^{\lambda_i y} \cos(\omega x) d\omega \\ &= \frac{2\mu_{12}}{\pi} \lim_{y \rightarrow 0} \int_0^\infty f(y, \omega, p) \cos(\omega x) d\omega. \end{aligned} \quad (3)$$

where coefficients A_i are functions of material constants, Laplace transform parameter and thickness of the layer. The Green's function for stress $Y(x, p)$ can be defined as function $f(\omega, p)$ in the Fourier transform domain. As the function $f(\omega)$ has following behavior, for large value of ω , as

$$f(y, \omega, p) = \sum_{i=3}^4 \left[\omega f_i^0 + \frac{1}{\omega} f_i'(p) + O_i\left(\frac{1}{\omega^3}\right) \right] e^{\lambda_i^\infty y} \quad (4)$$

where f_i^0 is a constant defined by material properties only and is the same for static infinite orthotropic sheet, f_i' is the function of both material constants and Laplace transform parameter p . The summations of $f_3^0 + f_4^0$ and $f_3' + f_4'$ are derived in Appendix. In addition, λ_i^∞ denote the roots of following characteristic equations for large value of ω and can be presented as follows

$$\lambda_{1,2}^\infty = \omega \sqrt{\eta_{1,2}^\infty}, \quad \lambda_{3,4}^\infty = -\lambda_{1,2}^\infty \tag{5}$$

where material constants

$$\eta_{1,2}^\infty = \frac{1}{2c_{22}} \left[(c_{12}^2 + 2c_{12} - c_{11}c_{22}) \pm \sqrt{(c_{12}^2 + 2c_{12} - c_{11}c_{22})^2 - 4c_{22}c_{11}} \right]. \tag{6}$$

Thus, the normal stress caused by a displacement discontinuity at origin is given by

$$Y(x, p) = \frac{2\mu_{12}}{\pi} \int_0^{\omega_0} g(\omega) \cos(\omega x) d\omega - \frac{2\mu_{12}f_0}{\pi x^2} - \frac{2f_1\mu_{12}}{\pi} \text{Ci}(\omega_0 x) \tag{7}$$

where new function $g(\omega) = f(\omega) - \omega f_0$, $f_0 = f_3^0 + f_4^0$, $f_1 = f_3' + f_4'$ and Ci denotes cosine integral.

3 Stress intensity factor and example

Suppose there is opening discontinuity displacement defined as $\varphi(= \Delta \tilde{v} = [\tilde{v}^+ - \tilde{v}^-]/2)$ on the crack surfaces Γ in the region $-a \leq x \leq a$, where a is the half length of crack as shown in Figure 3. By using the superposition principle, the integral equation for stress σ_y in the transformed domain on the crack surface can be written as

$$\int_{-a}^a Y(\xi - \eta, p) \varphi(\eta) d\eta = -\tilde{\sigma}_0(\xi, p), \quad -a \leq \xi \leq a \tag{8}$$

where from $\tilde{\sigma}_0(\xi, p)$ is the transformed traction (compression) applied on the crack surface $-a \leq \xi \leq a$. It is worth to notice that the integral equation (8) has a singular kernel of the second degree of Hadamard's finite part, from the Green's function (7), and can be presented as

$$\int_{-a}^a \frac{\varphi(\eta)}{|\xi - \eta|^2} d\eta + \int_{-a}^a G(\xi - \eta) \varphi(\eta) d\eta = \frac{\pi \tilde{\sigma}_0(\xi, p)}{2f_0\mu_{12}} \tag{9}$$

where function $G(\xi - \eta)$ is of weak singular $\ln r$ as discussed in above section, i.e.

$$G(\eta) = -\frac{1}{f_0} \int_0^{\omega_0} g(\omega) \cos(\omega \eta) d\omega + \frac{f_1}{f_0} \text{Ci}(\omega_0 \eta). \tag{10}$$

Due to the integral formula derived by Kaya and Erdogan [4], integral equation (8) at collocation point ξ_i becomes

$$\sum_{k=0}^K c_k \left[-\pi(k+1)U_k(\xi_i/a) + \int_{-a}^a G(\xi_i - \eta) \sqrt{a^2 - \eta^2} U_k(\eta/a) d\eta \right] = \frac{\pi \tilde{\sigma}_0(\xi_i)}{2f_0\mu_{12}}$$

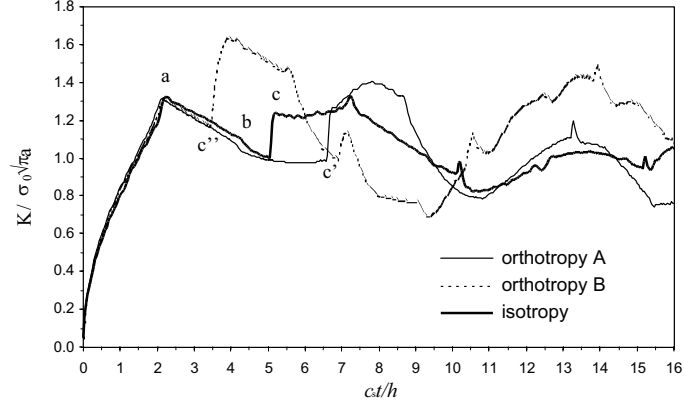


Figure 1: Dynamic stress intensity factors for $a = 5h$ for different medium under uniform load on the crack surface.

$$i = 0, 1, 2, \dots, K. \quad (11)$$

Finally stress intensity factors, in the Laplace transform domain, can also be determined straight away by displacement discontinuity as follows

$$\tilde{K}_I(\pm a, p_l) = 2f_0\mu_{12} \lim_{r \rightarrow 0} \sqrt{\frac{\pi}{2r}} \varphi(\pm a) = 2f_0\mu_{12} \sum_{k=0}^K c_k U_k(\pm 1), \quad l = 0, 1, 2, \dots, L \quad (12)$$

To demonstrate the accuracy of proposed method, an isolated crack of length $2a$ in an infinite strip of width $2h$ subjected uniform opening load $\sigma_0 H(t)$ on the surfaces is investigated. One orthotropic material and one isotropic material are considered and the material properties are listed in Table 1. The number of sample points in Laplace space

Table 1: Mechanical properties of composites

	Steel	E-glass-epoxy (A)	E-glass-epoxy (B)
c_{11}	3.5	8.38	2.29
c_{22}	3.5	2.29	8.38
c_{12}	1.5	0.52	0.52
μ_{12} (GPa)	76.92	5.5	5.5
c_R/c_s	0.9274	0.9725	0.9603

$L = 300$, constants in Durbin's inversion $\eta = 0.25$, $T = 20$ and the number of collocation point on the crack surface $K = 20$, the thickness of the layer is taken as $h = 5a$. For the opening-mode stress intensity factor $K_I(t)$, the coordinate of the first kink (a) is given by $c_s t/a = 2c_s/c_R$ which is the time required for stress surface waves to travel from one crack tip to the other tip. It is clear that the first kink is thus caused by the arrival of this surface wave. The second one (b) is due to the surface wave starting from one crack tip and travelling to the other and back. In general, there are many kinks generated by the different waves. Obversely the third kink (c) is due to the arrival of the reflected dilatation wave from the free boundary starting from the crack surface and the normalized time is $c_s t/a = 10/\sqrt{c_{11}} = 5.3452$. It is not difficult to identify each sharp kink in Figure 1 by considering the arrival times for the elastic waves.

4 Conclusions

This paper is an extension of application of DDM from elastostatic orthotropic cracked strip to elastodynamics. A Green's function of displacement discontinuity was deduced for an orthotropic strip in this paper. Integral equation method for cracked strip under impact load on the crack surface was shown to be efficient and accurate to the evaluation of dynamic stress intensity factor. The stress intensity factors were evaluated directly with high accuracy from the discontinuity of displacement on the crack surface by use of Chebyshev polynomials. In addition, due to the influence on the stress intensity factor by the elasticity waves is significant, the measurement of arrival time for elasticity waves can be used to detect the crack position in the structures by using strain gauges.

References

- [1] Chen, E.P., Sih. G.C., Transient response of crack to impact loads, *Elastodynamic Crack Problems*, Sih, G.C. Edit, Noordhoff, Leiden (1977).
- [2] Freund, L.B., *Dynamic Fracture Mechanics*, Cambridge University Press, New York (1990).
- [3] Kassir, M.K. and Bandyopadhyay, K.K., Impact response of a cracked orthotropic medium, *ASME, J. Appl. Mech.*, **50**, 630-636 (1983).
- [4] Kaya, M.K. and Erdogan, F., On the solution of integral equations with strong singular kernels, *Q. Appl. Math.*, **45**, 105-122 (1987).

NUMERICAL DETERMINATION OF THE MODE-I CRACK SIF IN GRADIENT ELASTIC MATERIALS VIA THE BEM

G.F. Karlis¹, S. V. Tsinopoulos² and D. Polyzos³

¹ Department of Mechanical and Aeronautical Engineering,
University of Patras, GR-26500 Patras, Greece
gkarlis@mech.upatras.gr

² Department of Civil Engineering,
University of Patras, GR-26500 Patras, Greece
stsinop@upatras.gr

³ Department of Mechanical and Aeronautical Engineering
University of Patras, GR-26500 Patras, Greece
and

Institute of Chemical Engineering and High Temperature Chemical Process, Patras, Greece
polyzos@mech.upatras.gr

Keywords: gradient elasticity, fracture mechanics, mode-I crack, BEM, variable-order element

Abstract. An advance Boundary Element Method (BEM) for solving mode-I fracture mechanics problems in gradient elastic materials is presented. The analysis is performed in the context of a simple gradient elastic theory, which can be considered as the simplest case of the general gradient elastic theory proposed by Mindlin. A new special, variable order discontinuous element is proposed for the treatment of singular fields around the tip of the crack and for the accurate evaluation of the Mode-I stress intensity factors (SIFs). The utilized gradient elastic BEM machinery is that recently proposed by Polyzos et al. (Part I) and Tsepoura et al. (Part II) in *Comp. Meth. Appl. Mech. Engng.*, Vol. 192, Issue 26-27, 2003. The crack profiles and the corresponding SIFs for different internal length scale parameters are obtained and their differences as they are compared to the corresponding ones taken classically are discussed.

Introduction

In classical elasticity theory all the fundamental quantities and material constants defined at any point of the analyzed elastic body are taken as mean values over very small volume elements the size of which must be sufficiently large in comparison with the material microstructure. Considering a very simple one dimensional example and taking Taylor expansions for displacements around the point of interest, Exadaktylos and Vardoulakis [1] explain that this assumption is possible only when displacements vary constantly or linearly throughout the aforementioned representative volume elements (RVEs). In cases where non-linear variations of displacements are observed, higher order Taylor expansion terms and thus higher order gradients of displacements should be taken into account. Making use of higher Taylor terms, however, some new internal length scale constants correlating the microscopic RVE with the macrostructure are introduced in the constitutive equations of the considered elastic continuum [2]. Thus, in fracture mechanics problems where near the tip of the crack abrupt changes of strains and stresses are observed, enhanced elastic theories that take into account higher order gradients of strains and stresses and introduce new internal length scale parameters to describe microstructural effects, should be applied. Among those who developed such theories one can mention Mindlin[2,3], Koiter[4], Kleinert[5,6] and Vardoulakis[7]. Mindlin's theory is the most general and comprehensive gradient elastic theory appearing to date in the literature. However, in order to make things simpler Mindlin proposed three simplified versions of his theory valid for long wave considerations, known as low frequency approximation Form I, II and III. In those three simplified gradient elastic theories, the potential energy density is considered to be a function of strains and the gradient of displacement gradient, strains and rotation gradient, respectively. Thus, beyond the classical Lamé constants λ, μ two new internal length scale parameters l_1 and l_2 are introduced in the constitutive equation of the considered material with microstructural effects. In case where $l_1=l_2$, the Form II of Mindlin's theory becomes identical to the gradient elastic one proposed by Aifantis[8]. The aforementioned simple gradient elastic theories have been successfully used in the past to eliminate

singularities or discontinuities of classical elasticity theory and to demonstrate their ability to capture size and edge effects, necking in bars, nano-structured materials behavior and wave dispersion in cases where this was not possible in the classical elasticity framework. In fracture mechanics, simple gradient elastic theories such those of Vardoulakis[7] and Aifantis[8] have been extensively used for understanding size-effect and crack-microdefect interaction phenomena in brittle materials and for the evaluation of more realistic fields and crack profiles near the tip of Mode-I[9,10,11], Mode-II[11,12] and Mode-III[13,14] cracks.

However, use of the gradient elastic theories in boundary value and fracture mechanics problems increases considerably the solution difficulties in comparison with the corresponding cases in classical elasticity. For this reason, the need of using numerical methods for the treatment of those problems is apparent. Shu et al.[15] and Amanatidou and Aravas[16] have used the finite element method (FEM) for solving two-dimensional elastostatic problems in the framework of the general theories of Mindlin. For the same purpose Tang et al.[17] proposed a Meshless Local Petrov-Galerkin (MLPG) methodology, while Polyzos et al.[18] and Tsepoura et al.[19,20] developed a boundary element method (BEM) for solving two and three dimensional elastostatic problems in the context of the simple strain-gradient theories of Vardoulakis[7] and Aifantis[8].

In the present work, the gradient elastic BEM proposed by Polyzos et al.[17] and Tsepoura et al.[18] is employed for the solution of a two dimensional Mode-I fracture mechanics problem. As it is explained in [10,12,13,14], near the tip of the crack displacements and strains are regular while double stresses and total stresses appear a singular behavior of order $r^{-1/2}$ and $r^{-3/2}$, respectively, with r being the distance from the tip. Adopting the idea of using variable-order boundary elements around the crack's tip for the evaluation of the corresponding SIF [21,22], a new special variable-order discontinuous element is proposed here for the treatment of singular fields around the tip of the crack. The paper is organized as follows: the constitutive equations, the classical as well as the non-classical boundary conditions and the integral representation of the considered gradient elastic fracture mechanics problem are presented in the next section. The proposed here new special variable-order discontinuous element is illustrated in the section after next. The numerical implementation of the problem and the solution procedure of the utilized BEM code are explained in brief in the forth section. Finally, the mode-I crack problem is solved and the obtained crack profiles as well as the corresponding SIFs are presented and discussed.

Integral Representation of the Problem

In this section the equation of equilibrium and the corresponding boundary conditions that should be satisfied by any linear elastic material described by the simple gradient elastostatic theory addressed in Polyzos et al. [18] are presented in brief.

Consider a linear gradient elastic body of volume V surrounded by a smooth surface S . The geometry of this body is described with the aid of the unit normal vector $\hat{\mathbf{n}}$ on S and a Cartesian coordinate system with its origin located interior to V . Considering isotropic materials properties the storage potential energy-density has the form [2]

$$W = \tilde{\boldsymbol{\tau}} : \tilde{\boldsymbol{\epsilon}} + \tilde{\boldsymbol{\mu}} : \nabla \tilde{\boldsymbol{\epsilon}} \quad (1)$$

where $\tilde{\boldsymbol{\tau}}$ is the Cauchy stress tensor being dual in energy with the macroscopic strain tensor $\tilde{\boldsymbol{\epsilon}}$, $\tilde{\boldsymbol{\mu}}$ is a third order tensor, called by Mindlin double stress tensor, which is dual to the strain gradient $\nabla \tilde{\boldsymbol{\epsilon}}$ while the two and three dots indicate inner product between tensors of second and third order, respectively. Considering zero body forces and taking the variation of the potential energy-density (1) over V and performing some algebra [18], one obtains the following gradient elastic equation of equilibrium

$$\nabla \cdot (\tilde{\boldsymbol{\tau}} - \nabla \cdot \tilde{\boldsymbol{\mu}}) = \mathbf{0} \quad (2)$$

accompanied by the classical boundary conditions

$$\mathbf{p}(\mathbf{x}) = \hat{\mathbf{n}} \cdot \tilde{\boldsymbol{\tau}} - (\hat{\mathbf{n}} \otimes \hat{\mathbf{n}}) : \frac{\partial \tilde{\boldsymbol{\mu}}}{\partial n} - \hat{\mathbf{n}} \cdot (\nabla_s \cdot \tilde{\boldsymbol{\mu}}) - \hat{\mathbf{n}} \cdot [\nabla_s \cdot (\tilde{\boldsymbol{\mu}})^{213}] + (\nabla_s \cdot \hat{\mathbf{n}})(\hat{\mathbf{n}} \otimes \hat{\mathbf{n}}) : \tilde{\boldsymbol{\mu}} - (\nabla_s \hat{\mathbf{n}}) : \tilde{\boldsymbol{\mu}} = \mathbf{p}_0 \quad (3)$$

$$\text{and/or } \mathbf{u}(\mathbf{x}) = \mathbf{u}_0$$

and the non-classical ones

$$\mathbf{R}(\mathbf{x}) = \hat{\mathbf{n}} \cdot \tilde{\boldsymbol{\mu}} \cdot \hat{\mathbf{n}} = \mathbf{R}_0 \text{ and/or } \mathbf{q}(\mathbf{x}) = \frac{\partial \mathbf{u}(\mathbf{x})}{\partial n} = \mathbf{q}_0 \quad (4)$$

where \mathbf{p}, \mathbf{R} represent the traction and double stresses traction vectors, respectively, \mathbf{u} stands for displacements, \mathbf{q} is the normal derivative of displacements, $\mathbf{u}_0, \mathbf{p}_0, \mathbf{R}_0, \mathbf{q}_0$ denote prescribed vectors and the symbols \otimes and ∇_s indicate dyadic product and surface gradient, respectively.

According to [18], strains e_{ij} , double stresses μ_{ijk} , relative stresses s_{ij} , Cauchy stresses τ_{ij} and total stresses σ_{ij} are given by the following relations:

$$\tilde{\boldsymbol{\sigma}} = \tilde{\boldsymbol{\tau}} + \tilde{\boldsymbol{s}} \quad (5)$$

$$\tilde{\boldsymbol{s}} = -\nabla \cdot \tilde{\boldsymbol{\mu}} = -g^2 \nabla^2 \tilde{\boldsymbol{\tau}} \quad (6)$$

$$\tilde{\boldsymbol{\mu}} = g^2 \nabla \tilde{\boldsymbol{\tau}}, \quad \tilde{\boldsymbol{\tau}} = 2\mu \tilde{\boldsymbol{e}} + \lambda (\nabla \cdot \tilde{\boldsymbol{u}}) \tilde{\mathbf{I}} \quad (7)$$

$$\tilde{\boldsymbol{\tau}} = 2\mu \tilde{\boldsymbol{e}} + \lambda (\nabla \cdot \tilde{\boldsymbol{u}}) \tilde{\mathbf{I}} \quad (8)$$

$$\tilde{\boldsymbol{e}} = \frac{1}{2} [\nabla \mathbf{u} + \mathbf{u} \nabla] \quad (9)$$

where g^2 is the volumetric strain energy gradient coefficient, the only constant that relates the microstructure with the macrostructure and $\tilde{\mathbf{I}}$ is the unit tensor.

Adopting the above simple strain gradient theory and inserting the constitutive eqs (5)-(9) into eq. (2) one obtains the equation of equilibrium of a gradient elastic continuum in terms of the displacement field \mathbf{u} in the form

$$\mu \nabla^2 \mathbf{u} + (\lambda + \mu) \nabla \nabla \cdot \mathbf{u} - g^2 \nabla^2 [\mu \nabla^2 \mathbf{u} + (\lambda + \mu) \nabla \nabla \cdot \mathbf{u}] = \mathbf{0} \quad (10)$$

As it is proved in [18], the integral representation of the above described problem is

$$\tilde{\mathbf{c}}(\mathbf{x}) \cdot \mathbf{u}(\mathbf{x}) + \int_S \left\{ \tilde{\mathbf{p}}^*(\mathbf{x}, \mathbf{y}) \cdot \mathbf{u}(\mathbf{y}) - \tilde{\mathbf{u}}^*(\mathbf{x}, \mathbf{y}) \cdot \mathbf{p}(\mathbf{y}) \right\} dS_y = \int_S \left\{ \frac{\partial \tilde{\mathbf{u}}^*(\mathbf{x}, \mathbf{y})}{\partial n_y} \cdot \mathbf{R}(\mathbf{y}) - \tilde{\mathbf{R}}^*(\mathbf{x}, \mathbf{y}) \cdot \mathbf{q}(\mathbf{y}) \right\} dS_y \quad (11)$$

where $\tilde{\mathbf{u}}^*(\mathbf{x}, \mathbf{y})$ is the fundamental solution of eq.(10) given in [18], $\tilde{\mathbf{p}}^*(\mathbf{x}, \mathbf{y}), \tilde{\mathbf{R}}^*(\mathbf{x}, \mathbf{y})$ are the fundamental traction and double stress traction tensors taken by inserting the fundamental displacement $\tilde{\mathbf{u}}^*(\mathbf{x}, \mathbf{y})$ in relations (3) and (7), respectively and $\tilde{\mathbf{c}}(\mathbf{x})$ is the well-known jump tensor being equal to $1/2 \tilde{\mathbf{I}}$ for $\mathbf{x} \in S$ and equal to $\tilde{\mathbf{I}}$ when $\mathbf{x} \in V \cap S$. All the kernels appearing in the integral eq (11) are given explicitly in [18].

Observing eq (11), one realizes that this equation contains four unknown vector fields, $\mathbf{u}(\mathbf{x}), \mathbf{p}(\mathbf{x}), \mathbf{R}(\mathbf{x})$ and $\mathbf{q}(\mathbf{x})$. Thus, after the satisfaction of the classical and non-classical boundary conditions, the evaluation of the unknown fields requires the existence of one more integral equation. This integral equation is obtained by applying the operator $\partial/\partial n_x$ on eq.(11) and has the form

$$\tilde{\mathbf{c}}(\mathbf{x}) \cdot \frac{\partial \mathbf{u}(\mathbf{x})}{\partial n_x} + \int_S \left\{ \frac{\partial \tilde{\mathbf{p}}^*(\mathbf{x}, \mathbf{y})}{\partial n_x} \cdot \mathbf{u}(\mathbf{y}) - \frac{\partial \tilde{\mathbf{u}}^*(\mathbf{x}, \mathbf{y})}{\partial n_x} \cdot \mathbf{p}(\mathbf{y}) \right\} dS_y = \int_S \left\{ \frac{\partial^2 \tilde{\mathbf{u}}^*(\mathbf{x}, \mathbf{y})}{\partial n_x \partial n_y} \cdot \mathbf{R}(\mathbf{y}) - \frac{\partial \tilde{\mathbf{R}}^*(\mathbf{x}, \mathbf{y})}{\partial n_x} \cdot \mathbf{q}(\mathbf{y}) \right\} dS_y \quad (12)$$

The kernels appearing in eq (12) are given explicitly in [18].

Integral eqs (11) and (12) accompanied by the classical and non-classical boundary conditions form the integral representation of any gradient elastic boundary value problem obeying to eqs (2)-(8).

Variable-order Discontinuous Element

According to [10,12-14], near the crack tip, the fields $\mathbf{u}, \mathbf{q}, \mathbf{R}$ and \mathbf{p} vary as $r^{3/2}, r^{1/2}, r^{-1/2}$ and $r^{-3/2}$ respectively, with r being the distance from the tip. In the present work, adopting the idea of using variable-order boundary elements around the crack's tip for the evaluation of the corresponding SIF [21,22], a new special variable-order discontinuous element is proposed here for the treatment of singular fields around the tip of the crack.

In this special element, the local coordinates of the functional nodes are identical to those of a classical discontinuous three-noded quadratic element, with the discontinuous side residing always on the crack tip. The main advantage of using discontinuous elements is that no functional nodes are located on the tip of the

crack and thus, despite the singularity of \mathbf{R} and \mathbf{p} on the tip, the field nodal values are finite and can be computed.

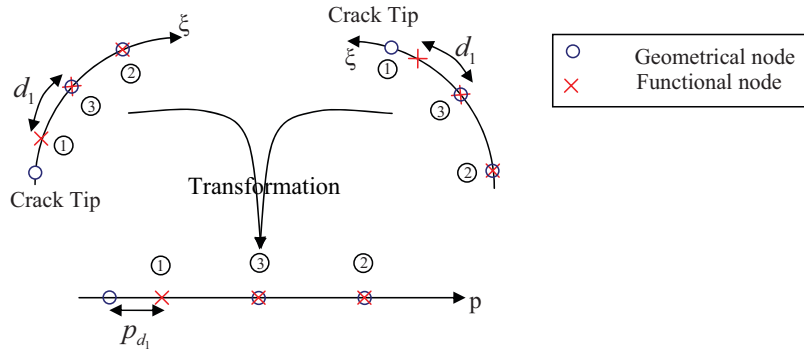


Figure 1: Variable-order discontinuous element transformation

As shown in Figure 1 the tip of the crack can be located either at $\xi = -1$ or at $\xi = 1$. In order to unify these two possible cases, a linear transformation is introduced:

$$p = 1 + c\xi/2 \tag{13}$$

with $c = \pm 1$ if the tip resides at $\xi = \mp 1$ respectively, noting that $p \in [0,1]$ and the tip of the crack is always located at $p = 0$. The fields, in terms of the asymptotic solutions [21,22], can be expressed as:

$$\mathbf{F} = \mathbf{K}_1 r^{\lambda_1} + \mathbf{K}_2 r^{\lambda_2} + \mathbf{C} \tag{14}$$

with the symbol \mathbf{F} representing $\mathbf{u}, \mathbf{q}, \mathbf{R}$ or \mathbf{p} and λ_1, λ_2 taking values from Table 1.

\mathbf{F}	λ_1	λ_2
\mathbf{u}	3/2	1
\mathbf{q}	1/2	1
\mathbf{R}	-1/2	1
\mathbf{P}	-3/2	-1/2

Table 1: Orders of magnitude of the asymptotic fields

Writing eq (14) for the three functional nodes of the variable-order discontinuous element we obtain:

$$\begin{aligned} r = p_d L: \mathbf{K}_1 (Lp_d)^{\lambda_1} + \mathbf{K}_2 (Lp_d)^{\lambda_2} + \mathbf{C} &= \mathbf{F}_1 \\ r = \frac{L}{2}: \mathbf{K}_1 \left(\frac{L}{2}\right)^{\lambda_1} + \mathbf{K}_2 \left(\frac{L}{2}\right)^{\lambda_2} + \mathbf{C} &= \mathbf{F}_3 \\ r = L: \mathbf{K}_1 L^{\lambda_1} + \mathbf{K}_2 L^{\lambda_2} + \mathbf{C} &= \mathbf{F}_2 \end{aligned} \tag{15}$$

where $\mathbf{F}_1, \mathbf{F}_2$ and \mathbf{F}_3 are the nodal values of the field, p_d is the local coordinate of the discontinuous functional node and L is the length of the element. In the present work p_d is considered to be equal to $1/6$. The solution to the above linear system yields the values for the parameters $\mathbf{K}_1, \mathbf{K}_2$ and \mathbf{C} as functions of the nodal values $\mathbf{F}_1, \mathbf{F}_2$ and \mathbf{F}_3 . Substituting $\mathbf{K}_1, \mathbf{K}_2$ and \mathbf{C} into eq (14), rearranging with respect to the nodal values $\mathbf{F}_1, \mathbf{F}_2$ and \mathbf{F}_3 and taking into account that the distance from the tip of the crack is $r = Lp$, the field \mathbf{F} can be written as:

$$\mathbf{F} = N_1 \mathbf{F}_1 + N_2 \mathbf{F}_2 + N_3 \mathbf{F}_3 \tag{16}$$

with the interpolation functions N_i being:

$$\begin{aligned}
 N_1(p) &= \frac{2^{\lambda_1} [(1-2^{\lambda_2})p^{\lambda_1} - 1] - 2^{\lambda_2} [(1-2^{\lambda_1})p^{\lambda_2} - 1]}{2^{\lambda_1} [(1-2^{\lambda_2})p_{d_1}^{\lambda_1} - 1] - 2^{\lambda_2} [(1-2^{\lambda_1})p_{d_1}^{\lambda_2} - 1]} \\
 N_2(p) &= \frac{-2^{\lambda_1} [(1-2^{\lambda_2} p_{d_1}^{\lambda_2})p^{\lambda_1} - p_{d_1}^{\lambda_1}] + 2^{\lambda_2} [(1-2^{\lambda_1} p_{d_1}^{\lambda_1})p^{\lambda_2} - p_{d_1}^{\lambda_2}]}{2^{\lambda_1} [(1-2^{\lambda_2})p_{d_1}^{\lambda_1} - 1] - 2^{\lambda_2} [(1-2^{\lambda_1})p_{d_1}^{\lambda_2} - 1]} \\
 N_3(p) &= \frac{2^{\lambda_1 + \lambda_2} [(1-p_{d_1}^{\lambda_2})p^{\lambda_1} - (1-p_{d_1}^{\lambda_1})p^{\lambda_2} - p_{d_1}^{\lambda_1} + p_{d_1}^{\lambda_2}]}{2^{\lambda_1} [(1-2^{\lambda_2})p_{d_1}^{\lambda_1} - 1] - 2^{\lambda_2} [(1-2^{\lambda_1})p_{d_1}^{\lambda_2} - 1]}
 \end{aligned} \tag{17}$$

It is obvious that for the fields \mathbf{R} and \mathbf{p} the interpolation functions (17) become singular while approaching the tip of the crack. It can be easily verified that $\sum N_i = 1$ and for $\lambda_1 = 2$ and $\lambda_2 = 1$ the functions (17) coincide with the classical discontinuous quadratic element interpolation functions.

BEM Procedure and SIF Calculation

The goal of the BEM is to solve numerically the well-posed boundary value problem constituted by the system of two integral equations (11) and (12) and the boundary conditions (3) and (4). To this end the global boundary S is discretized into three-noded, quadratic, continuous and discontinuous isoparametric boundary elements, while two special variable-order discontinuous elements are placed on either side of the crack. Then, the integral eqs (11) and (12) for a node k are written as

$$\begin{aligned}
 \frac{1}{2} \mathbf{u}^k + \sum_{\beta=1}^M \tilde{\mathbf{H}}_{\beta}^k \mathbf{u}^{\beta} + \sum_{\beta=1}^M \tilde{\mathbf{K}}_{\beta}^k \mathbf{q}^{\beta} &= \sum_{\beta=1}^M \tilde{\mathbf{G}}_{\beta}^k \mathbf{p}^{\beta} + \sum_{\beta=1}^M \tilde{\mathbf{L}}_{\beta}^k \mathbf{R}^{\beta} \\
 \frac{1}{2} \mathbf{q}^k + \sum_{\beta=1}^M \tilde{\mathbf{S}}_{\beta}^k \mathbf{u}^{\beta} + \sum_{\beta=1}^M \tilde{\mathbf{T}}_{\beta}^k \mathbf{q}^{\beta} &= \sum_{\beta=1}^M \tilde{\mathbf{V}}_{\beta}^k \mathbf{p}^{\beta} + \sum_{\beta=1}^M \tilde{\mathbf{W}}_{\beta}^k \mathbf{R}^{\beta}
 \end{aligned} \tag{18}$$

where M is the total number of nodes. Explicit expressions for $\tilde{\mathbf{H}}_{\beta}^k, \tilde{\mathbf{K}}_{\beta}^k, \tilde{\mathbf{G}}_{\beta}^k, \tilde{\mathbf{L}}_{\beta}^k, \tilde{\mathbf{S}}_{\beta}^k, \tilde{\mathbf{T}}_{\beta}^k, \tilde{\mathbf{V}}_{\beta}^k$ and $\tilde{\mathbf{W}}_{\beta}^k$ are given in [19]. Collocating eqs (18) at all nodal points M and applying the boundary conditions (eqs (3) and (4)) one produces the final linear system of algebraic equations of the form $\tilde{\mathbf{A}} \cdot \mathbf{X} = \mathbf{B}$, where the vectors \mathbf{X} and \mathbf{B} contain all the unknown and known nodal components of the boundary fields, respectively. The singular and hypersingular integrals involved, are evaluated with high accuracy applying a methodology for direct treatment of CPV and hypersingular integrals [19], noting that an extra singularity due to the singular behaviour of the interpolation functions (17) near the tip of the crack should be taken into account. Finally, the linear system is solved via a typical LU-decomposition algorithm and the vector \mathbf{B} comprising all the unknown nodal values of $\mathbf{u}, \mathbf{p}, \mathbf{R}, \mathbf{q}$ is evaluated.

Approaching the crack tip ($r \rightarrow 0$) the traction \mathbf{p} , according to eq (14), admits a representation of the form:

$$\mathbf{p} = \mathbf{K}_1 (\mathbf{p}_1, \mathbf{p}_2, \mathbf{p}_3) \lim_{r \rightarrow 0} r^{-3/2} + \mathbf{K}_2 (\mathbf{p}_1, \mathbf{p}_2, \mathbf{p}_3) \lim_{r \rightarrow 0} r^{-1/2} \tag{19}$$

where the components of the vectors \mathbf{K}_1 and \mathbf{K}_2 stand for the stress intensity factors corresponding to x and y directions according to the following relations:

$$\begin{aligned}
 \mathbf{K}_1 &= \begin{Bmatrix} K_{1x} \\ K_{1y} \end{Bmatrix} = L^{3/2} p_{d_1} \frac{\sqrt{p_{d_1}} (2 - \sqrt{2}) \mathbf{p}_1 + (\sqrt{2} - 2\sqrt{p_{d_1}}) \mathbf{p}_2 - (\sqrt{2} - \sqrt{2p_{d_1}}) \mathbf{p}_3}{2 - \sqrt{2} + (-4 + \sqrt{2}) p_{d_1} + 2p_{d_1}^{3/2}} \\
 \mathbf{K}_2 &= \begin{Bmatrix} K_{2x} \\ K_{2y} \end{Bmatrix} = \sqrt{L} \frac{p_{d_1}^{3/2} (\sqrt{2} - 4) \mathbf{p}_1 + (4p_{d_1}^{3/2} - \sqrt{2}) \mathbf{p}_2 + \sqrt{2} (1 - p_{d_1}^{3/2}) \mathbf{p}_3}{2 - \sqrt{2} + (-4 + \sqrt{2}) p_{d_1} + 2p_{d_1}^{3/2}}
 \end{aligned} \tag{20}$$

Mode-I Crack Problem

A two dimensional problem dealing with a square gradient elastic plate with a central horizontal line crack is solved numerically. The plate is subjected to a constant tensile stress $P_0 = 100\text{MPa}$, normal to all of its sides. Crack length is chosen to be equal to $a = 1\text{m}$ and the side of the square plate is $L = 8a$. The Young modulus and the Poisson ratio of the gradient elastic plate is $E = 210\text{GPa}$ and $\nu = 0.2$, respectively, while the volumetric strain energy gradient coefficient takes the values $g^2 = 5.625 \cdot 10^{-5}$, 0.0025 and 0.04 m . The BEM procedure described in the previous section is exploited for the solution of the above 2D fracture mechanics problem. Figure 2 displays the upper-right-quarter of the crack shape obtained from the present BEM for three different values of the material volumetric strain energy gradient coefficient g^2 . In the same figure, the crack profile provided by the classical elasticity theory ($g^2 = 0$) is addressed. The main conclusion here is that the crack profile near the tip in the gradient elastic case remains sharp, i.e. the crack tip is not blunted as in the classical case. Also, it should be noticed that as the volumetric strain energy gradient coefficient increases the crack becomes stiffer.

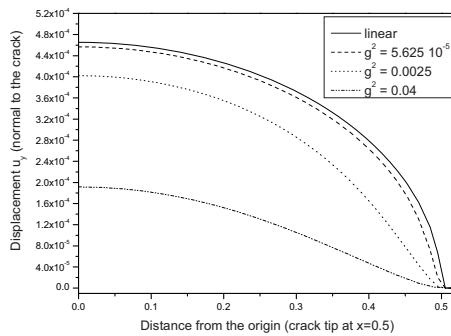


Figure 2: Shape of mode-I crack for different values of the gradient coefficient g^2

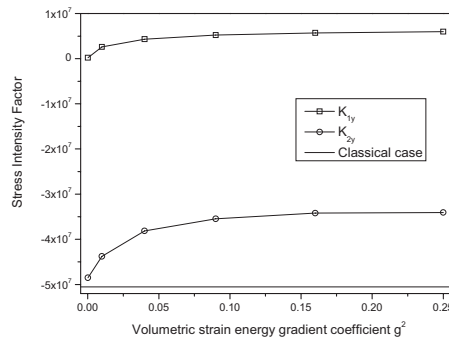


Figure 3: Stress Intensity Factors with respect to g^2

In Figure 3 the stress intensity factors, K_{1y} , K_{2y} , normal to the crack, are plotted with respect to g^2 . The interesting remark here is that the stress intensity factor K_{1y} tends to zero as the gradient coefficient g^2 tends to zero. As a result eq(19) becomes $p_y = K_{2y} \lim_{r \rightarrow 0} r^{-1/2}$, with K_{2y} being the classical SIF provided by the literature for the present Mode-I problem.

References

- [1] Exadaktylos, G., Vardoulakis, I., "Microstructure in linear elasticity and scale effects: a reconsideration of basic rock mechanics and rock fracture mechanics", *Technophysics* 335, pp. 81-109 (2001).
- [2] Mindlin, R. D.: "Microstructure in linear elasticity", *Arch. Rat. Mech. Anal.*, Vol. 10, pp. 51-78 (1964).
- [3] Mindlin, R. D., "Second gradient of strain and surface tension in linear elasticity", *Int. J. Solids Struct.*, Vol. 1, pp. 417-438 (1965).
- [4] Koiter, W. T., "Couple stresses in the theory of elasticity. I and II. Proceedings of the Koninklijke Nederlandse Akademie Van Wetenschappen (B) 67, pp. 17-44 (1964).
- [5] Kleinert, H., "Gauge fields in condensed matter", Vol.2, World Scientific (1989).

- [6] Zhang, X., Sharma, P., "Inclusions and inhomogeneities in strain gradient elasticity with couple stresses and related problems", *Int. J. Solids Struct.*, Vol. 42, pp. 3833-3851 (2005).
- [7] Vardoulakis, I., Sulem, J., "Bifurcation Analysis in Geomechanics", Blackie - Chapman and Hall, London (1995).
- [8] Ru, C. Q. and Aifantis, E. C., "A simple approach to solve boundary value problems in gradient elasticity", *Acta Mechanica*, Vol. 101, pp. 59-68 (1993).
- [9] Aifantis, E. C., "On the role of gradients in the localization of deformation and fracture", *Int. J. Engng. Sci.*, Vol. 30, pp. 1279-1299 (1992).
- [10] Exadaktylos G., "Gradient elasticity with surface energy: Mode-I crack problem", *Int. J. Solids Structures*, Vol. 35, Nos. 5-6, pp. 421-456 (1998).
- [11] Shi, M.X., Huang, Y., Hwang, K.C., "Fracture in a higher-order elastic continuum", *J. Mech. Phys. Solids*, 48, pp. 2513-2538 (2000).
- [12] Vardoulakis, I., Exadaktylos, G., "The asymptotic solution of anisotropic gradient elasticity with surface energy for a mode-II crack", Durban, D., Pearson, J.R.A., (Eds), IUTAM Symposium, Haifa, Israel (1997).
- [13] Vardoulakis, I., Exadaktylos, G., Aifantis, E., "Gradient elasticity with surface energy: Mode-III crack problem", *Int. J. Solids Struct.*, Vol. 33, pp. 4531-4559 (1996).
- [14] Georgiadis, G., "The Mode-III crack problem in microstructured solids governed by dipolar gradient elasticity: static and dynamic analysis", *J. Appl. Mech.* Vol. 70, pp. 517-530 (2003).
- [15] Shu, J. Y., King, W. E., Fleck, N. A., "Finite elements for materials with strain gradient effects", *Int. J. Num. Meth. Engng.*, Vol. 44, pp. 373-391 (1999).
- [16] Amanatidou, E. and Aravas, N., "Mixed finite element formulations of strain-gradient elasticity problems", *Comp. Meth. Appl. Mech. Engng.*, Vol. 191, pp. 1723-1751 (2002).
- [17] Tang, Z., Shen, S., Atluri, S.N., "Analysis of materials with strain-gradient effects: A Meshless Local Petrov-Galerkin (MLPG) approach with nodal displacements only", *CMES: Computer Modeling in Engineering & Sciences*, Vol. 4, pp. 177-196 (2003).
- [18] Polyzos D., Tsepoura K. G., Tsinopoulos S. V. and Beskos D. E., "A Boundary Element Method for solving 2-D and 3-D Static Gradient Elastic problems. Part I: Integral Formulation", *Comp. Meth. Appl. Mech. Engng.*, Vol. 192, Issue 26-27, pp. 2845-2873 (2003).
- [19] Tsepoura K. G., Tsinopoulos S. V., Polyzos D. and Beskos D. E., "A Boundary Element Method for solving 2-D and 3-D Static Gradient Elastic problems. Part II: Numerical Implementation", *Comp. Meth. Appl. Mech. Engng.*, Vol. 192, Issue 26-27, pp. 2875-2907 (2003).
- [20] Tsepoura, K. G., Polyzos, D., "Static and harmonic BEM solutions of gradient elasticity problems with axisymmetry", *Comput. Mech.*, Vol. 32, pp. 89-103 (2003).
- [21] K.M. Lim, K.H. Lee, A.A.O. Tay, W. Zhou, "A new variable-order singular boundary element for two-dimensional stress analysis", *Int. J. Numer. Meth. Engng* 2002; 55: 293-316 (2002)
- [22] W. Zhou, K.M. Lim, K.H. Lee, A.A.O. Tay, "A new variable-order singular boundary element for calculating stress intensity factors in three-dimensional elasticity problems", *Int. J. Solids & Structures*;42:159-185 (2005)

A Boundary-Integral Method for iterative solution of scattering problems with variable impedance surface condition

F. Collino¹, F. Millot² and S. Pernet³

CERFACS, 42, Avenue Gaspard Coriolis, 31057 Toulouse Cedex 01, France

Email: ¹collino@cerfacs.fr, ²millot@cerfacs.fr, ³pernet@cerfacs.fr

keywords: Electromagnetic scattering, Boundary integral equations, Impedance boundary condition, Combined Field Integral Equation

Abstract. A boundary element method is used to solve electromagnetic scattering problems relative to an impedance boundary condition on an obstacle of arbitrary shape in the frequency domain. In particular, a technique based on the Combined Field Integral Equation (CFIE) is introduced. After discretization, the final system is solved by an iterative method coupled with the Fast Multipole Method (FMM). Finally, a numerical comparison with a well-trying method to solve this kind of problem justifies the pertinence of our choice and proves that we obtain an attractive technique in terms of memory storage and CPU time spent.

Introduction

We address the solution of electromagnetic scattering problems by an obstacle whose surface is covered with imperfectly conductor materials. This type of materials is generally taken into account by imposing an impedance boundary condition like the Leontovich condition [1] on the surface of the object. This latter connects the tangential component of the magnetic field with the tangential trace of the electric field via an operator. More precisely, we have the relation $\mathbf{n} \times (\mathbf{E} \times \mathbf{n}) = Z_0 \eta (\mathbf{n} \times \mathbf{H})$ where \mathbf{E} and \mathbf{H} are the electric and magnetic fields respectively, \mathbf{n} is the unit normal to the surface of the object, Z_0 is the intrinsic impedance of the vacuum and η is the impedance operator which is not necessary constant. It was recognized that this type of boundary condition can be extensively used to get a more tractable problem in numerous complex situations of electromagnetic scattering computations. For example, in order to avoid detection by radar, objects are often partially coated by a thin dielectric to reduce the radar cross section of the scattering wave. In this case, the direct scattering problem is a mixed boundary value problem for Maxwell's equations where on the coated part of the boundary the electromagnetic field satisfies an impedance boundary condition and on the remaining part of the boundary the tangential component of the total electric field vanishes. So, it is crucial to have numerical methods which are able to deal with such a boundary condition.

In the frequency domain, the total electromagnetic fields are expressed in terms of the equivalent electric and magnetic currents on the scatterer surface to satisfy the boundary conditions. And the boundary integral methods (BIM) can be used to solve this kind of problem. Nevertheless, several difficulties appear. Firstly, the BIM lead to the resolution of a dense system which needs the use of an iterative solver when the size of the problem becomes more important. The convergence rate of most of iterative methods depends, amongst other things, on the condition number and on the clustering of the eigenvalues of the system's matrix on the complex plane. However, we remark that the presence of the impedance operator, especially if it is variable, produces a main dispersion of the spectrum of the system which significantly deteriorates the convergence rate. The second difficulty comes from the fact that the electric \mathbf{J} and magnetic \mathbf{M} currents are linked by the relation induced by the IBC. This characteristic forces to be cautious when discretizing. Indeed, it is well known that the flux continuity of \mathbf{M} and \mathbf{J} across the edges of the mesh is crucial to ensure the charge conservation. Charges are themselves very important for the numerical scheme consistency. That is why, a direct elimination of one current via the IBC is not desirable if one wants to stay in the natural framework for the electromagnetism and a more judicious technique is also necessary to impose the IBC [2] [3]. The main interest of this paper is to propose a numerical scheme well-adapted to the iterative resolution of impedant problems.

Derivation of an integral formulation

Integral representation of the solution

We want to find the radiating electromagnetic fields \mathbf{E} and \mathbf{H} solution to the Maxwell system satisfying the impedance boundary condition $\mathbf{n} \times (\mathbf{E}|_{\Gamma} \times \mathbf{n})(x) - Z_0(\eta(x)\mathbf{n} \times \mathbf{H}|_{\Gamma}) = 0$ where Γ is the surface of the scatterer Ω^- , \mathbf{n} denotes the unit normal to Γ pointing into the exterior, Z_0 is the intrinsic impedance of the vacuum and $\eta(x)$ is a scalar complex piecewise constant functions satisfying the condition $\Re(\eta) > 0$ (ie the scatterer is absorbing).

Any radiating electromagnetic field (\mathbf{E}, \mathbf{H}) is uniquely determined by the knowledge of the two equivalent currents $\mathbf{J}(x) = \mathbf{n} \times \mathbf{H}(x)$ and $\mathbf{M}(x) = -\mathbf{n} \times \mathbf{E}(x)/iZ_0$ (we have divided the electric field by iZ_0 in order to work with two homogeneous currents currents \mathbf{J} and \mathbf{M}) through the well known Stratton-Chu formulae, [4]

$$\begin{cases} \mathbf{E}(x) = \mathbf{E}^{\text{inc}}(x) + iZ_0(\tilde{T}\mathbf{J}(x) + \tilde{K}\mathbf{M}(x)) & x \in \Omega^+ = (\Omega^-)^c \\ \mathbf{H}(x) = \mathbf{H}^{\text{inc}}(x) - \tilde{K}\mathbf{J}(x) - \tilde{T}\mathbf{M}(x) & x \in \Omega^+, \end{cases} \quad (1)$$

where $(\mathbf{E}^{\text{inc}}, \mathbf{H}^{\text{inc}})$ stands for an electromagnetic incident field and the respective potentials \tilde{T} and \tilde{K} are defined by

$$\begin{cases} \tilde{T}\mathbf{J}(x) = k \int_{\Gamma} G(x, y)\mathbf{J}(y)d\Gamma(y) + \frac{1}{k} \int_{\Gamma} \vec{\nabla}_x G(x, y)\text{div}_{\Gamma}\mathbf{J}(y)d\Gamma(y) \\ \tilde{K}\mathbf{J}(x) = \int_{\Gamma} \vec{\nabla}_y G(x, y) \wedge \mathbf{J}(y)d\Gamma(y). \end{cases} \quad (2)$$

$G(x, y)$ is the Green kernel for the radiating solution of the 3-D Helmholtz equation

$$G(x, y) = \frac{\exp(ik|x - y|)}{4\pi|x - y|}, \quad (3)$$

and $\text{div}_{\Gamma}\mathbf{J}$ denotes the surface divergence of \mathbf{J} .

The tangential traces on Γ of the potentials \tilde{T} and \tilde{K} are known When x approaches the boundary Γ in (1), we get

$$\begin{aligned} (\mathbf{n} \times (\mathbf{E} - \mathbf{E}^{\text{inc}})|_{\Gamma} \times \mathbf{n})(x) &= iZ_0(T\mathbf{J}(x) + K\mathbf{M}(x) + \frac{1}{2}\mathbf{n} \times \mathbf{M}(x)), \\ (\mathbf{n} \times (\mathbf{H} - \mathbf{H}^{\text{inc}})|_{\Gamma} \times \mathbf{n})(x) &= -K\mathbf{J}(x) - \frac{1}{2}\mathbf{n} \times \mathbf{J}(x) - T\mathbf{M}(x), \end{aligned} \quad (4)$$

where T and K are defined by

$$\begin{aligned} T\mathbf{J}(x) &= \lim_{y \rightarrow x} \mathbf{n}(x) \times (\tilde{T}\mathbf{J}(y) \times \mathbf{n}(x)), \\ K\mathbf{J}(x) &= \left(\int_{\Gamma} \mathbf{n}(x) \times (\nabla_y G(x, y) \times \mathbf{J}(y))d\Gamma(y) \right) \times \mathbf{n}(x) \end{aligned} \quad (5)$$

Using the definition of currents, we can get rid of the tangential trace of the electromagnetic field, we obtain

$$\begin{cases} -(\mathbf{n} \times (\mathbf{E}^{\text{inc}})|_{\Gamma} \times \mathbf{n})(x) &= iZ_0(T\mathbf{J}(x) + K\mathbf{M}(x) - \frac{1}{2}\mathbf{n} \times \mathbf{M}(x)) \quad , \\ (\mathbf{n} \times (\mathbf{H}^{\text{inc}})|_{\Gamma} \times \mathbf{n})(x) &= +K\mathbf{J}(x) + T\mathbf{M}(x) - \frac{1}{2}\mathbf{n} \times \mathbf{J}(x) \end{cases} \quad (6)$$

This relation holds whatever the boundary condition is; when impedant boundary condition is considered, we have to add the impedance boundary condition or equivalently

$$\mathbf{n} \times \mathbf{M}(x) = -i\eta\mathbf{J}(x) \text{ or } \mathbf{n} \times \mathbf{J}(x) = -i\eta^{-1}\mathbf{M}(x) \quad (7)$$

The two unknowns \mathbf{J}, \mathbf{M} have to be determined using the four previous equations. And several boundary integral formulations can be constructed to solve the considered scattering problem. The derivations of these formulations can be shown for example in [2].

In particular, one can derive a formulation which keeps the two currents as unknowns [3] and that we note BGLF (Bachelot-Gay-Lange Formulation) in reference to these authors. Note that only classical integrals operators T and K take place in this formulation and must be evaluated. The main advantage of this formulation is that the conservation of the electric and magnetic flux through the edges of the surface mesh is ensured in an independent way. But on the perfectly metallic part of the surface Γ , this formulation degenerates into a EFIE. We know that in this case, the convergence of the iterative solver is not good. After discretization, the size of the linear system is twice larger than in the perfect conductor case because of the presence of the two unknowns. For all these reasons, we propose to construct another formulation with only one unknown, which degenerates into a CFIE equation when the obstacle is perfectly conductor. Nevertheless, BGLF is used to compare the performance of the new technique proposed in this paper.

An Impedante Combined Field Integral Equation formulation (ICFIE)

To overcome the main drawback of the BGLF (EFIE on the perfectly metallic parts) and to improve the convergence rates, we have studied the possibility to construct a Combined Field Integral Equation to solve the impedance problem that we have considered. Indeed, it is well known that, in the case of perfectly metallic object, this type of formulation leads to linear systems that can be solved by iterative methods with a good convergence rate. So, we expect that this property will remain true for the impedant case.

As for BGLF, we use a simple combinaison of (6) and (7) to derive our Impedante Combined Field Integral Equation formulation (ICFIE). More precisely, we make a linear combination of the first equation of (6) with the second having undergoes a rotation of $\frac{\pi}{2}$ (ie by applying the operator $\mathbf{n} \times \cdot$) and we formally obtain the well known equation: $CFIE = \alpha EFIE + \gamma MFIE$ with $\gamma = (1 - \alpha)$ or $CFIE = EFIE + \beta MFIE$ where α, β are real or complex numbers.

Remark: We keep the designations of EFIE and Magnetic Field Integral Equation (MFIE) because these two equations degenerate into their classical form on the perfectly metallic part of Γ ie when $\mathbf{M} = 0$.

Now, write the ICFIE system

$$\begin{cases} -\frac{\mathbf{E}_t^{\text{inc}}}{iZ_0} + \beta \mathbf{n} \times \mathbf{H}_t^{\text{inc}} = (T + \beta \mathbf{n} \times K + \frac{\beta}{2})\mathbf{J} + \mathbf{n} \times (\beta T - \mathbf{n} \times K - \frac{1}{2})\mathbf{M} \\ \mathbf{n} \times \mathbf{M} = -i\eta \mathbf{J} \end{cases} \quad (8)$$

We remark that the first equation of ICFIE system (8) could be written under the form $CFIE(\mathbf{J}) + \beta \mathbf{n} \times CFIE(\mathbf{M})$ where the CFIE terms correspond to the case of perfectly conducting obstacle and by taking different coupling parameters (ie β and $-\frac{1}{\beta}$). So after discretization, the matrix-vector product is easy to compute by the FMM algorithm applied to the ‘‘classical’’ CFIE equation.

To implement a numerical resolution of the system (8), we are confronted to two main difficulties:

A difficulty is the choice of the parameter β . Indeed β acts upon the robustness and the accuracy of the scheme. For the perfectly metallic case, it is commonly admitted that $\beta = 4$ (i.e. $\alpha = 0.2$) is, in most cases, the best compromise. One would like to know if this value is still a good choice for the impedant material. In fact, it is not the case. One can prove theoretically on the spherical geometry that $\beta = -1$ allows the best clustering of eigenvalues of the ICFIE system in the complex plan [5]. Moreover, it is well known that the MFIE term penalizes the CFIE in term of accuracy. The choice $\beta = -1$ is apriori less penalizing that $\beta = 4$. Numerical results in section 5 will show that the ICFIE chosen has a correct behaviour in term of accuracy.

The main difficulty which appears is: how to eliminate the magnetic current and more generally how to treat the rotation operator $\mathbf{n} \times \cdot$?

When one wants to build an integral equation to solve this type of problems, one is quickly confronted with a difficulty of functional nature. Indeed, the impedance condition implies a relation between two quantities of different nature. The discretization with the classical finite elements, which ensures only the conservation of flux through the edges of the surface mesh, can prove to be problematic. For example, it is legitimate to want to eliminate one of the currents directly via the impedance condition, unfortunately, one is quickly confronted with the computation of complicated integral operators [2]. More generally, the mapping $\Phi : \mathbf{u} \rightarrow \mathbf{n} \times \mathbf{u}$ is an isomorphism between the functional spaces $H^{-\frac{1}{2}}(div_\Gamma, \Gamma)$ and $H^{-\frac{1}{2}}(rot_\Gamma, \Gamma)$ and the composition of this

mapping with the single layer potential is not obvious to make numerically (Recall that the single layer operator T is well-defined on the functional space $H^{-\frac{1}{2}}(\text{div}, \Gamma)$). Moreover, even if the magnetic charges have been expressed in terms of the electric currents, they stay present in the formulation. Since the conservation of these charges as well as the electric ones is crucial to the consistency of the numerical scheme, the electric currents must fulfill the following requirement: their tangentials well as their normal component must be continuous at each interface between two elements of the mesh. No finite-element method is yet available which, while remaining simple enough, at the same time satisfies such a degree of continuity constraint and applies to a surface of arbitrary shape.

All these reasons have brought us to keep the magnetic current as an intermediate variable and not to directly evaluate the term $\mathbf{n} \times CFIE(\mathbf{M})$. To take into account this last term, we have considered the following process:

$$\begin{cases} -\frac{\mathbf{E}_t^{\text{inc}}}{iZ_0} + \beta \mathbf{n} \times \mathbf{H}_t^{\text{inc}} = (T + \beta \mathbf{n} \times K + \frac{\beta}{2}) \mathbf{J} + \beta \mathbf{n} \times V \\ V = (T - \frac{1}{\beta} \mathbf{n} \times K - \frac{1}{2\beta}) \mathbf{M} \\ \mathbf{n} \times \mathbf{M} = -i\eta \mathbf{J} \end{cases} \quad (9)$$

The goal is to reveal the term $(T - \frac{1}{\beta} \mathbf{n} \times K - \frac{1}{2\beta}) \mathbf{M}$ which is easy to discretize (it corresponds to a classical CFIE) and to determine an approximate of its composition with $\mathbf{n} \times \cdot$.

After a brief description of the classical Wilton-Rao-Glissson (WRG) finite elements space [6], we will present the discretization of (9).

Discrete scheme

The discrete problem is obtained by means of Galerkin's method; the scatterer's surface Γ is meshed with triangles, and the surface electric and magnetic currents are expanded as $J(x) \approx \sum_{j=1}^N I_j \phi_j(x)$ and $M(x) \approx \sum_{j=1}^N M_j \phi_j(x)$, where the $\phi_j(x)$'s are WRG basis functions associated to the mesh ; for each edge j , each $\phi_j(x)$ is supported by the two triangles $T^\pm(j)$ having j as an edge. If $v_\pm(j)$ are the vertices of $T^\pm(j)$ opposite to the edge j , we have

$$\phi_j(x) = +\frac{x - v_+(j)}{2 \text{Area}(T_+(j))} \text{ on } T_+(j), -\frac{x - v_-(j)}{2 \text{Area}(T_-(j))} \text{ on } T_-(j), 0 \text{ elsewhere.} \quad (10)$$

We denote by *WRG* the space spanned by the WRG basis functions.

(a)-Evaluation of the term $T + \beta \mathbf{n} \times K + \frac{\beta}{2}$ (*CFIE*(\mathbf{J})):

The term $(T + \beta \mathbf{n} \times K + \frac{\beta}{2}) \mathbf{J}$ is transformed to the matrix form $\mathcal{Z}_{h,\beta} \mathbf{J}$ where \mathbf{J} is the column vector which contains the degrees of freedom of the electric current and $\mathcal{Z}_{h,\beta}$ is the matrix of interactions between the basis functions given by:

$$\begin{aligned} \mathcal{Z}_{h,\beta}^{i,j} &= \int_{\Gamma} \int_{\Gamma} G(x,y) \left(\phi_i(x) \cdot \phi_j(y) - \frac{1}{k^2} \vec{\nabla}_{\Gamma} \cdot \phi_j \vec{\nabla}_{\Gamma} \cdot \phi_i \right) d\Gamma(x) d\Gamma(y) \\ &+ \frac{\beta}{2} \int_{\Gamma} \phi_j(x) \cdot \phi_i(x) d\Gamma(x) + \beta \int_{\Gamma} \int_{\Gamma} \nabla_y G(x,y) \wedge \phi_j(y) \cdot (\phi_i(x) \wedge \mathbf{n}(x)) d\Gamma(y) d\Gamma(x) \end{aligned} \quad (11)$$

(b)-Elimination of the magnetic current:

The first idea which comes at the spirit to determine the current \mathbf{M} when we know \mathbf{J} is to project the impedance condition directly onto the H-rot conform boundary finite elements space which corresponds to the space $\mathbf{n} \times \text{WRG}$.

This is written : for all test function \mathbf{M}' belonging to *WRG*

$$\int_{\Gamma} (\mathbf{n} \times \mathbf{M}) \cdot (\mathbf{n} \times \mathbf{M}') d\Gamma = -i \int_{\Gamma} \eta \mathbf{J} \cdot (\mathbf{n} \times \mathbf{M}') d\Gamma \quad (12)$$

One can then write the following matrix relation between the discrete electric and magnetic currents

$$\mathcal{M}_h \mathbf{M} = \mathcal{M}_{div/rot,h}^\eta \mathbf{J} \tag{13}$$

where \mathbf{J} and \mathbf{M} are column vectors which contains the degrees of freedom of the electric and magnetic currents respectively, \mathcal{M}_h is the mass matrix of the interactions between the basis functions of the finite elements space $\mathbf{n} \times WRG$ and $\mathcal{M}_{div/rot,h}^\eta$ is the matrix of the elementary integrals $\int_\Gamma \eta \phi_i \cdot (\mathbf{n} \times \phi_j) d\Gamma$.

(c)-Discretization of the second equation of 9:

We choose to find V in WRG (ie $V(x) \approx \sum_{j=1}^N V_j \phi_j(x)$). Now, by taking as $J^t(x)$ the WRG basis functions, the second equation of 9 immediatly leads to the matrix system:

$$\mathcal{M}_h V = \mathcal{L}_{h,-\frac{1}{\beta}} \mathbf{M} \tag{14}$$

Knowing V , they remain us simply to carry out the sparse matrix-vector product $\mathcal{M}_{rot/div,h} V$ where $\mathcal{M}_{rot/div,h}$ is the matrix of interactions $(\mathbf{n} \times \phi_i, \phi_j)$.

Formally, we can write the system corresponding to the resolution of the ICFIE by using the steps **a**, **b** and **c**

$$\left(\mathcal{L}_{h,\beta} + \beta \mathcal{M}_{rot/div,h} \mathcal{M}_h^{-1} \mathcal{L}_{h,-\frac{1}{\beta}} \mathcal{M}_h^{-1} \mathcal{M}_{div/rot,h}^\eta \right) \mathbf{J} = B^{inc} \tag{15}$$

where the vector column B^{inc} corresponds to the the second member.

After discretization the ICFIE system (15) is solved by an iterative solver in particular the GMRES solver [7] and by using a SParse Approximate Inverse (SPAI) preconditioner. The only unknown is the electric current \mathbf{J} . The magnetic current \mathbf{M} is eliminated during the matrix-vector product needed at each iteration by using the strategy **a**. To solve the system (13) and (14), we use a sparse solver which allows a quick and low cost inversion. In particular, we have used MUMPS (MULTifrontal Massively Parallel sparse direct Solver) [8].

Numerical experiments

We consider a cylinder of height $60m$ and radius $15m$. The mesh is composed of 65392 triangles that corresponds to 98088 degrees of freedom for the electric current. The value of the wavenumber is fixed to 1.28 and consequently we have about 10 points per wavelength for the discretization. We have considered two configurations. The first one corresponds to a constant value of the impedance operator $\eta = 0.34$ and in the second case, we have divided the cylinder in three section on which we have imposed different impedances values. In particular, $\eta = 0.34$ for $0 < z < 20$ and $40 < z < 60$ and $\eta = 0$ for $20 < z < 40$.

Table 1 sums up the density of the preconditioners and the CPU times spent for their construction. As with the sphere, we note that the density (The number of non-zero values divided by the number of unknowns squared) are almost the same for both methods and that the ICFIE is more expensive in terms of CPU time. One can also note that the CPU spent does not depend on the value of the impedance.

case	density	CPU time	
		FBGL	ICFIE
case 1	0.07%	40min	80min
case 2	0.075%	40min	80min

Table 1-Density of the preconditioners and CPU times spent to obtain them

Case	currents	RCS
case 1	4.6%	0.2%
case 2	6.7%	0.31%

Table 2-Relative error between the currents and the RCS in function of the value of the impedance operator

We can notice that the two solutions are similar in terms of current and RCS (see table 2). One can also see a little increase of the error when the impedance operator becomes variable.

Table 3 gives the number of iteration and the CPU times needed for the construction of the solution. One notices that:

- On the one hand, the number of iterations for the ICFIE does not depend very much of the value of the impedance operator. On the other hand, the FBGL is very sensitive to the variations of η and particularly when there is perfectly conducting part on the surface of the obstacle.
- The important gain is obtained by using the ICFIE. Moreover, one can notice that it is directly connected to the gain in term of number of iterations.

Figures (1) show the RCS for the case 1 and 2. One sees that they are very close.

Case	number of iterations		CPU time	
	FBGL	ICFIE	FBGL	ICFIE
case 1	34	16	48min	24min
case 2	159	17	240min	25min

Table 3-Number of iterations and CPU time needed to obtain the solution in function to the value of η

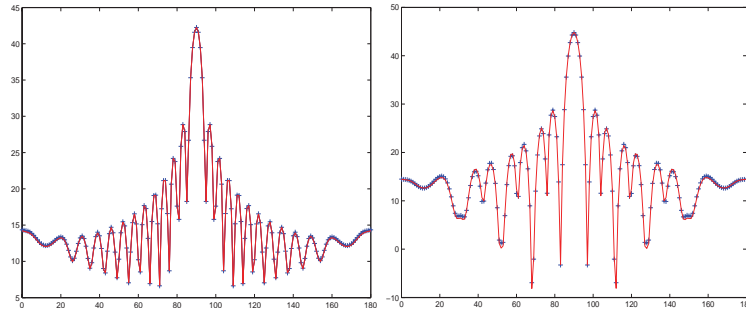


Figure 1: RCS for the case 1 (left) and RCS for the case 2 (right) (+:ICFIE: -: FBGL)

Conclusion

In this paper, we have studied a technique based on the CFIE formulation to solve electromagnetic scattering problems relative to an impedance boundary condition on an obstacle of arbitrary shape in the frequency domain. This formulation can be rewritten with two terms, one which is directly linked to the CFIE term when the obstacle is perfectly conducting $CFIE(\mathbf{J})$ and another term which is related to $\mathbf{n} \times CFIE(\mathbf{M})$. The magnetic current is computed via the impedance relation. We have proposed to eliminate the magnetic current and we keep only the electric current as unknown. After discretization, the final system is solved with an iterative solver coupled with a FMM algorithm. Numerical results are presented. Comparison with a well-tried method is proposed. Good accuracy is obtained. The proposed method improves the CPU time.

References

- [1] M.A. Leontovitch, "Approximate boundary conditions for the electromagnetic field on the surface of a good conductor", Investigations Radiowave Propagation part II, Moscow, Academy of Sciences, 1978.
- [2] A. Bendali, M'B Fares, J. Gay, "A Boundary-Element Solution of the Leontovitch Problem", IEEE Transaction on antennas and propagation, **47**, 10, pp. 1597-1605, 1999.
- [3] V. Lange, "Equations intégrales espace-temps pour les équations de Maxwell. Calcul du champ diffracté par un obstacle dissipatif", PhD thesis, Université de Bordeaux I, oct. 1995.
- [4] D. Colton, R. Kress, "Inverse acoustic and electromagnetic scattering theory", Applied Mathematical Sciences, **93**, Springer, Berlin, 1992.
- [5] A. Makhlouf, "Résolution de problèmes de diffraction d'ondes électromagnétiques par équations intégrales de frontière avec condition d'impédance", CERFACS Working Note WN/EMC/04/93.
- [6] S.M. Rao, D.R. Wilton and A.W. Glisson, "Electromagnetic scattering by surfaces of arbitrary shape", IEEE trans. Antennas Propagat., vol. AP-30, pp. 409-418, May 1982.
- [7] V. Frayssé, L. Giraud, S. Gratton, J. Langou, "A Set of GMRES Routines for Real and Complex Arithmetics on High Performance Computers", CERFACS Technical Report, TR/PA/03/3.
- [8] Multifrontal Massively Parallel Solver, <http://www.enseiht.fr/lima/apo/MUMPS>.

Dual BEM for fracture analysis of magnetoelastoelectroelastic solids

F. García-Sánchez¹, A. Sáez², R. Rojas-Díaz² and Ch. Zhang³

¹ Civil Engineering Dept. Escuela de Ingenieros industriales. University of Málaga. Campus de El Ejido S/N, E-29013 Málaga (Spain). E-mail: fgsanchez@uma.es

² Continuum Mechanics Dept. Escuela Superior de Ingenieros. University of Sevilla. Camino de los Descubrimientos S/N, E-41092 Sevilla (Spain). E-mail: andres@us.es

³ Civil Engineering Dept. University of Siegen. Paul-Bonatz-Str. 9-11, D-57076 Siegen (Germany). E-mail: c.zhang@uni-siegen.de

Keywords: BEM, magnetoelastoelectroelastic materials, cracks, fracture mechanics.

Abstract. In this work the dual or hypersingular BEM is implemented for the study of fracture applications in 2-D magnetoelastoelectroelastic solids under static loading conditions. Previously obtained Green's functions for the infinite plane are implemented, and the integration procedure developed by García-Sánchez et al. [3] for anisotropic and piezoelectric materials fracture analysis is extended to the general magnetoelastoelectroelastic case. Evaluation of fracture parameters directly from computed nodal values is discussed. The accuracy of the boundary element solution is confirmed by comparison with selected analytical solutions reported in the literature.

Introduction

Smart structures applications are receiving increasing attention in latter years. Solids showing piezoelectric and piezomagnetic couplings are being widely used as ultrasonic transducers, magnetic field probes, etc. The most recent advances involve composite materials consisting of both piezoelectric and piezomagnetic phases, so that a magnetoelectric coupling effect is obtained as well. Although such coupling is not shown by any of the phases alone, the magnetoelectric coupling of the resulting composite may be much larger than that of a single phase magnetoelectric material [1].

At present, there is a growing interest to solve fracture problems in solids with magnetoelastoelectroelastic coupling effects [2,6,7,8]. However, limited work has been done in the field so far, as compared to the cases of elasticity and piezoelectricity/piezomagnetism.

In this work the dual or hypersingular BEM is implemented for the study of fracture applications in 2-D magnetoelastoelectroelastic solids under static loading conditions. The aim is to extend the formulation previously developed by García-Sánchez et al. [3] for anisotropic and piezoelectric materials crack analysis to magnetoelastoelectroelastic fracture. Explicit Green's functions derived by using the extended Stroh's formalism are implemented (see, e.g., [4,5]). Quadratic quarter-point elements are used to represent the crack opening displacements and the electric and magnetic potential discontinuities at the crack tip. Stress, electric displacement and magnetic induction intensity factors are computed from such nodal values. Results for various crack configurations are obtained with different mechanical, electric and magnetic loadings.

Governing Equations and Dual BEM Formulation

The linear magnetoelastoelectroelastic problem may be formulated in an elastic-like fashion by considering a displacement vector extended with the electric potential ϕ and the magnetic potential ψ (see, e.g., [2,5])

$$u_I = \begin{cases} u_i & I = 1,2 \\ \phi & I = 3 \\ \psi & I = 4 \end{cases} \quad (1)$$

where u_i are the elastic displacements.

Similarly, a stress tensor extended with the electric displacement D_i and the magnetic induction B_i should be considered

$$\sigma_{ij} = \begin{cases} \sigma_{ij} & J = 1,2 \\ D_i & J = 3 \\ B_i & J = 4 \end{cases} \quad (2)$$

σ_{ij} being the elastic stresses.

In this way the field equations may be written as

$$\sigma_{ij,i} = 0 \quad (3)$$

and the constitutive relations as

$$\sigma_{ij} = C_{iJKl} u_{K,l} \quad (4)$$

where

$$C_{iJKl} = \begin{cases} C_{ijkl} & J, K = 1,2 \\ e_{ijl} & J = 1,2 ; K = 3 \\ h_{ijl} & J = 1,2 ; K = 4 \\ -\varepsilon_{il} & J = 3 ; K = 3 \\ -\alpha_{il} & J = 4 ; K = 4 \\ -\gamma_{il} & J = 3 ; K = 4 \end{cases} \quad (5)$$

C_{ijkl} , e_{ijl} , h_{ijl} , γ_{il} , ε_{il} and α_{il} denote elastic stiffness tensor, piezoelectric, piezomagnetic and magnetoelectric coupling tensor, dielectric permittivities and magnetic permeabilities, respectively.

Therefore, the extension of Stroh formalism to the magnetoelastoelectric case permits to obtain the static fundamental solution in a form similar to that of the anisotropic and piezoelectric materials cases (see, e.g., [4,5]).

The dual BEM approach for fracture mechanics applications may be then expressed using the extended formulation in terms of both the displacement and traction boundary integral equations as usual [3]

$$c_{IJ} u_J + \int_{\Gamma} p_{IJ}^* u_J d\Gamma = \int_{\Gamma} u_{IJ}^* p_J d\Gamma \quad ; \quad c_{IJ} p_J + N_r \int_{\Gamma} s_{rIJ}^* u_J d\Gamma = N_r \int_{\Gamma} d_{rIJ}^* p_J d\Gamma \quad (6)$$

where N_r is the outward unit normal at the collocation point, p_{IJ}^* and u_{IJ}^* are the fundamental solution extended tractions and displacements, associated to a line force (I=1,2) or to a line charge (I=3 electric; I=4 magnetic), and s_{rIJ}^* and d_{rIJ}^* are obtained by differentiation as

$$s_{rIJ}^* = C_{rIMn} p_{MJ,n}^* \quad ; \quad d_{rIJ}^* = C_{rIMn} u_{MJ,n}^* \quad (7)$$

Subsequently, the extension of the regularization procedure proposed by García-Sánchez et al. [3] for the piezoelectric case to evaluate the singular and hypersingular integrals in (6) for magnetoelastoelectric solids may be achieved in a straight-forward manner.

The BE discretization follows [3], so that discontinuous quadratic elements with the two extreme collocation nodes shifted towards the element interior are used to mesh the cracks. The asymptotic extended displacements behavior near the tip of the crack is captured by means of discontinuous quarter-point elements. For the rest of the boundaries, continuous quadratic elements are employed.

Stress (K_I , K_{II}), electric displacement (K_E) and magnetic induction (K_M) intensity factors can be directly obtained from the extended displacements nodal values from

$$\begin{pmatrix} K_{II} \\ K_I \\ K_E \\ K_M \end{pmatrix} = \sqrt{\frac{\pi}{8\bar{r}}} \mathbf{Q}^{-1} \begin{pmatrix} \Delta u_1 \\ \Delta u_2 \\ \Delta \varphi \\ \Delta \phi \end{pmatrix} \quad (8)$$

\bar{r} being the distance to the crack tip.

The mechanical strain energy release rates may be as well obtained from

$$G_I^M = (Q_{21} K_I K_{II} + Q_{22} K_I^2 + Q_{23} K_I K_E + Q_{24} K_I K_M) / 2$$

$$G_{II}^M = (Q_{11} K_{II}^2 + Q_{12} K_{II} K_I + Q_{13} K_{II} K_E + Q_{14} K_{II} K_M) / 2$$
(9)

In equations (8) and (9)

$$\mathbf{Q} = \text{Re}(\mathbf{B})$$
(10)

where the definition for \mathbf{B} follows from the extension of that found for piezoelectrics in ref. [3].

Applications

Numerical examples are presented in this section for different crack configurations to show the effectiveness of the dual BEM for magneto-electroelastic crack problems. The accuracy of the BE results is shown by comparison with available analytical solutions in the literature. The material considered is a BaTiO₃-CoFeO₄ (V_F=0.5) whose properties are listed in Table 1.

Table 1. Material constants of BaTiO₃-CoFeO₄ (V_F=0.5)

C_{11} N/m ²	C_{12} N/m ²	C_{22} N/m ²	C_{66} N/m ²	e_{21} C/m ²	e_{22} C/m ²	e_{16} C/m ²	h_{21} N/Am
226×10^9	124×10^9	216×10^9	44×10^9	-2.2	9.3	5.8	290.2
h_{22} N/Am	h_{16} N/Am	ϵ_{11} C/Nm ²	ϵ_{22} C/Nm ²	α_{11} Ns/VC	α_{22} Ns/VC	γ_{11} Ns ² /C ²	γ_{22} Ns ² /C ²
350	275	5.64×10^{-9}	6.35×10^{-9}	5.367×10^{-12}	2.7375×10^{-9}	2.97×10^{-4}	8.35×10^{-5}

First, a straight crack in an unbounded plane is considered. This simple problem has been taken as a benchmark since it has known analytical solution [2]. The obtained stress intensity factor is the same as that of an isotropic material, whilst the electric displacement and magnetic induction intensity factors depend on the stress intensity factor, but not on the applied electric-magnetic loads, as expected. In all cases BE results are within 0.1% of the exact solution.

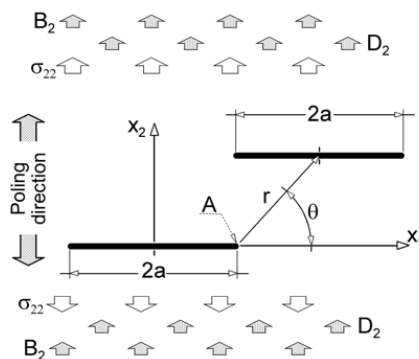


Figure 1. Two parallel cracks with remote loading

Next, interaction between two parallel cracks is considered, as shown in figure 1. The magnetic and electric poling directions are normal to the cracks and plane strain conditions are assumed.

In figure 2 the normalized mode I stress intensity factor at crack tip A ($K_I^A / \sqrt{\pi a} \sigma_{22}$) is plotted versus Tian and Gabbit [6] results for remote loading conditions given by: $\sigma_{22} \neq 0, D_2 = 0$ and $B_2 = 0; 10^{-6} \sigma_{22} A^{-1}m; -10^{-6} \sigma_{22} A^{-1}m$, respectively. Values for different location angles θ of the cracks are obtained (see figure 1).

Figure 3 shows the corresponding normalized magnetic induction intensity factor ($K_M^A / 10^{-6} \sqrt{\pi a} \sigma_{22}$) for this same loading.

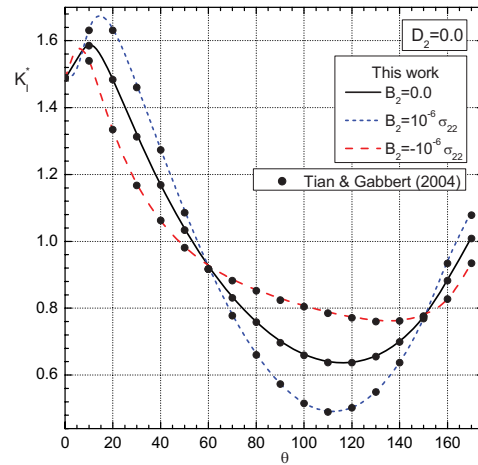


Figure 2. Normalized mode I stress intensity factor at crack tip A.

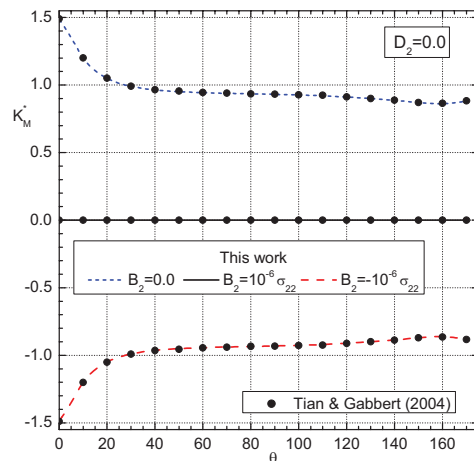


Figure 3. Normalized magnetic induction intensity factor at crack tip A.

Finally, in figure 4 the normalized mode I mechanical strain energy release rate ($G_I^A / 0.25\pi a H_{22} \sigma_{22}^2$ normalization as in ref. [6]) is plotted against the location angle θ for the following remote loading: $\sigma_{22} \neq 0$, $D_2 = 10^{-9} \sigma_{22} \text{ CN}^{-1}$ and $B_2 = 0; 10^{-6} \sigma_{22} \text{ A}^{-1}\text{m}; -10^{-6} \sigma_{22} \text{ A}^{-1}\text{m}$, respectively.

Good agreement between both sets of results is observed for all the cases.

Conclusions

An approach based on the dual boundary integral equation method has been developed to analyse plane cracks in magnetoelastoelectric solids. Green's functions obtained in closed form, by extending the anisotropic piezoelectric full-plane Green's functions -by means of Stroh formalism- to the general magnetoelastoelectric case, are implemented together with a generalization of the regularization procedure developed by García-Sánchez et al. [3] for anisotropic and piezoelectric materials BEM fracture analysis. Field intensity factors and energy release rates are accurately evaluated, as the comparison with analytical solutions previously reported in the literature illustrates.

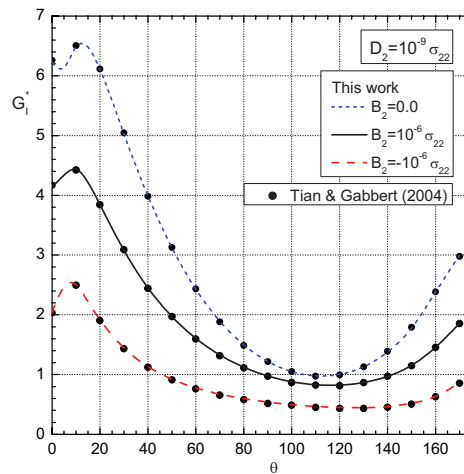


Figure 4. Normalized mode I mechanical strain energy release rate at crack tip A.

Acknowledgements

This work was partially supported by the *Ministerio de Educación y Ciencia* of Spain project DPI2004-08147-C02-02. The financial support is gratefully acknowledged.

References

- [1] Y. Benveniste, Magnetolectric effect in fibrous composites with piezoelectric and piezomagnetic phases, *Phys. Rev. B* **51**, 16424–16427 (1995).
- [2] C.-F. Gao, H. Kessler and H. Balke, Crack problems in magnetoelastoelectric solids. Part I: exact solution of a crack, *Int. J. Engrg. Sci.*, **41**, 969–981 (2003).
- [3] F. García-Sánchez, A. Sáez and J. Domínguez, Anisotropic and piezoelectric materials fracture analysis by BEM. *Computers and Structures*, **83**, 804-820 (2005).
- [4] X. Jiang and E. Pan, Exact solution for 2D polygonal inclusion problem in anisotropic magnetoelastoelectric full-, half-, and bimaterial-planes, *International Journal of Solids and Structures*, **41**, 4361–4382 (2004).
- [5] J.-X. Liu, X. Liu and Y. Zhao, Green's functions for anisotropic magnetoelastoelectric solids with an elliptical cavity or a crack, *Int. J. Engrg. Sci.*, **39**, 1405–1418 (2001).
- [6] W.-Y. Tian and U. Gabbert, Multiple crack interaction problem in magnetoelastoelectric solids. *European Journal of Mechanics - A/Solids*, **23**, 599-614 (2004).
- [7] W.Y. Tian and R.K.N.D. Rajapakse, Fracture analysis of magnetoelastoelectric solids by using path independent integrals, *International Journal of Fracture*, **131**, 311–335 (2005).
- [8] B.L. Wang and Y.W. Mai, Fracture of piezoelectromagnetic materials, *Mechanics Research Communications*, **31**, 65-73 (2004).

A 2-D Time-Domain BEM for Dynamic Analysis of Cracked Piezoelectric Solids

Felipe García-Sánchez¹, Chuanzeng Zhang² and Andres Sáez³

¹ Departamento de Ingeniería Civil, de Materiales y Fabricación, Universidad de Málaga, Plaza El Ejido s/n, 29013 Málaga, Spain

² Department of Civil Engineering, University of Siegen, Paul-Bonatz-Str. 9-11, D-57076 Siegen, Germany

³ Departamento de Mecánica de Medios Continuos, Teoría de Estructuras e I. del Terreno, Universidad de Sevilla, Camino de los Descubrimientos s/n, 41092 Sevilla, Spain

Keywords: Time-domain BEM, piezoelectric solids, dynamic crack analysis, dynamic intensity factors, convolution quadrature.

Abstract. A time-domain boundary element method (BEM) for transient dynamic crack analysis in two-dimensional (2-D), homogeneous and linear piezoelectric solids is presented in this paper. A combination of the strongly singular displacement boundary integral equations (BIEs) and the hypersingular traction BIEs is applied for this purpose. On the external boundary of the cracked solid strongly singular displacement BIEs are used, while on the crack-faces hypersingular traction BIEs are applied. Time-convolution is approximated by a convolution quadrature formula, while spatial discretization is performed by using collocation method. Numerical results for dynamic intensity factors are presented to show the accuracy of the present time-domain BEM.

Introduction

Due to the coupling effects between the mechanical and the electrical fields, piezoelectric materials are widely applied in transducers, actuators, sensors, and many other smart devices and structures. Dynamic crack analysis in piezoelectric solids is an important research issue in fracture and damage mechanics as well as non-destructive material testing, to characterize and evaluate the mechanical and the electrical integrity, the reliability and the durability of piezoelectric devices and structures. With this motivation in mind, transient dynamic crack analysis in 2-D, homogeneous and linear piezoelectric solids is presented in this paper. A time-domain BEM is developed for this purpose. The method uses a combination of strongly singular displacement BIEs and hypersingular traction BIEs. On the external boundary of the cracked piezoelectric solids, the classical displacement BIEs are applied, while on the crack-faces the hypersingular traction BIEs are used. For temporal discretization, the quadrature formula of Lubich [1,2] is adopted for approximating the Riemann convolution involved in the time-domain BIEs. For spatial discretization, collocation method with continuous and discontinuous quadratic elements is implemented. A special feature of the present time-domain BEM is that it requires only Laplace-domain instead of time-domain dynamic piezoelectric fundamental solutions.

Hypersingular boundary integrals arising in the present time-domain BEM are computed by using a special regularization technique based on a suitable change of variable consistent with the used fundamental solutions [3,4]. Regular boundary integrals and line-integrals contained in the dynamic piezoelectric fundamental solutions are computed numerically by using standard Gaussian quadrature formula. Quarter-point elements are applied at the crack-tips, to describe the local behavior of the generalized crack-opening-displacements (CODs) properly, and to ensure a direct and accurate computation of the dynamic intensity factors from the numerically determined generalized CODs.

To verify the accuracy of the present time-domain BEM, numerical results for the dynamic intensity factors are presented and compared with the numerical results obtained by the finite element method (FEM). As dynamic loading, mechanical impact, electrical impact, and combined mechanical and electrical impacts are considered. The effects of the electrical impact on the dynamic intensity factors and their dynamic overshoots are analyzed for different values of the loading parameter.

Problem formulation and time-domain BIEs

We consider a two-dimensional (2-D), homogeneous and linear piezoelectric solid with a crack. Using the quasi-electrostatic assumption and in the absence of body forces and electrical charges, the cracked piezoelectric solid satisfies the generalized equations of motion

$$\Sigma_{iJ,i} = \rho \delta_{JK}^* \dot{U}_K, \quad (1)$$

and the constitutive equations

$$\Sigma_{iJ} = E_{iJKl} U_{K,l}, \quad (2)$$

where ρ is the mass density, U_K , Σ_{iJ} , E_{iJKl} and δ_{JK}^* represent the generalized displacements, the generalized stresses, the generalized elasticity tensor and the generalized Kronecker delta, which are defined by

$$U_I = \begin{cases} u_I, & I = 1, 2, \\ \phi, & I = 3, \end{cases} \quad (3)$$

$$\Sigma_{iJ} = \begin{cases} \sigma_{iJ}, & J = 1, 2, \\ D_i, & J = 3, \end{cases} \quad (4)$$

$$E_{iJKl} = \begin{cases} c_{iJKl}, & J, K = 1, 2, \\ e_{Kli}, & J = 3, K = 1, 2, \\ e_{Jil}, & K = 3, J = 1, 2, \\ -\kappa_{il}, & J = K = 3, \end{cases} \quad (5)$$

$$\delta_{JK}^* = \begin{cases} \delta_{JK}, & J, K = 1, 2, \\ 0, & \text{otherwise.} \end{cases} \quad (6)$$

In eqs (3)-(6), u_i , σ_{ij} and D_i represent the displacement, the stress and the electric displacement components, c_{ijkl} is the elasticity tensor, e_{ijk} is the piezoelectric tensor, κ_{il} is the dielectric permittivity tensor, ϕ is the electrical potential, and δ_{jk} is the Kronecker delta. Throughout the analysis, a comma after a quantity represents partial derivatives with respect to spatial variables, while superscript dots denote temporal derivatives. Also, the conventional summation rule over double indices is applied. Lower case Latin indices take the values 1 and 2, while capital Latin indices take the values 1, 2 and 3.

As initial conditions, zero initial conditions are assumed

$$U_I(\mathbf{x}, t) = \dot{U}_I(\mathbf{x}, t) = 0 \text{ for } t \leq 0, \quad (7)$$

and the following boundary conditions are considered

$$P_I(\mathbf{x}, t) = 0, \quad \mathbf{x} \in \Gamma_c = \Gamma_c^+ + \Gamma_c^-, \quad (8)$$

$$P_I(\mathbf{x}, t) = P_I^*(\mathbf{x}, t), \quad \mathbf{x} \in \Gamma_\Sigma, \quad (9)$$

$$U_I(\mathbf{x}, t) = U_I^*(\mathbf{x}, t), \quad \mathbf{x} \in \Gamma_U. \quad (10)$$

Here, $P_I = \Sigma_{iJ} n_j$ is the generalized traction vector with n_j being the outward unit normal vector, $\Gamma_c = \Gamma_c^+ + \Gamma_c^-$ represents the upper and the lower crack-faces, Γ_Σ and Γ_U denote the external boundaries with prescribed generalized tractions P_I^* and generalized displacements U_I^* , respectively. It should be noted here that traction-free and electrically permeable boundary conditions on the crack-faces are assumed in eq (8).

Time-domain displacement BIEs can be written as

$$c_{iJ}(\xi) \cdot U_J(\xi, t) = \int_{\Gamma_\Sigma + \Gamma_U} (U_{iJ}^G * P_J - P_{iJ}^G * U_J) ds + \int_{\Gamma_c^+} P_{iJ}^G * \Delta U_J ds, \quad (11)$$

where the coefficients $c_{IJ}(\xi)$ depend on the smoothness of the boundary, $U_{IJ}^G(\xi, \mathbf{x}; t, \tau)$ and $P_{IJ}^G(\xi, \mathbf{x}; t, \tau)$ are the dynamic piezoelectric displacement and traction fundamental solutions, ξ and \mathbf{x} represent the observation and the source points, $\Delta U_I(\mathbf{x}, t)$ are the generalized crack-opening-displacements (CODs) which are defined by

$$\Delta U_I(\mathbf{x}, t) = U_I(\mathbf{x} \in \Gamma_c^+, t) - U_I(\mathbf{x} \in \Gamma_c^-, t), \tag{12}$$

and an asterisk * denotes Riemann convolution

$$f(t) * g(t) = \int_0^t f(t-\tau)g(\tau)d\tau. \tag{13}$$

By substituting eq (11) into the constitutive equations (2), using the relation $P_I = \Sigma_{jI} n_j$, taking the limit process $\xi \rightarrow \Gamma_\Sigma + \Gamma_U + \Gamma_c$, and considering the boundary conditions (8)-(10), time-domain traction BIEs can be obtained as

$$P_I(\xi, t) = \int_{\Gamma_\Sigma + \Gamma_U} (T_{IJ}^G * P_J - S_{IJ}^G * U_J) ds + \int_{\Gamma_c} S_{IJ}^G * \Delta U_J ds. \tag{14}$$

In eq (14), T_{IJ}^G and S_{IJ}^G are the dynamic piezoelectric fundamental solutions higher order, which are defined by

$$T_{IJ}^G = -E_{rIM} U_{MJ,I}^G n_r(\xi), \quad S_{IJ}^G = -E_{rIM} P_{MJ,I}^G n_r(\xi). \tag{15}$$

Time-domain and Laplace-domain dynamic fundamental solutions for homogenous and linear piezoelectric solids have been derived by Khutoryansky and Sosa [5], and Wang and Zhang [6]. Unfortunately, they cannot be given in closed forms, but they can be represented by line-integrals over a unit-circle in 2-D case. It will be shown in the next section that the present time-domain BEM requires only the Laplace-domain instead of the time-domain fundamental solutions. Note here that the displacement BIEs (11) are strongly singular and should be understood in the sense of Cauchy-principal value integrals, while the tractions BIEs (14) are hypersingular and should be regarded as Hadamard finite-part integrals.

Numerical solution procedure

To solve the strongly singular displacement BIEs (11) and the hypersingular traction BIEs (14), the convolution quadrature formula of Lubich [1,2] is applied for the temporal discretization while the collocation method is used for the spatial discretization. In the convolution quadrature formula of Lubich [1,2], the Riemann convolution is approximated by

$$f(t) = g(t) * h(t) = \int_0^t g(t-\tau)h(\tau)d\tau \cong \sum_{j=0}^n \omega_{n-j}(\Delta t)h(j\Delta t), \tag{16}$$

where the time t is divided into N equal time-steps Δt , and the weights $\omega_n(\cdot)$ are determined by

$$\omega_n(\Delta t) = \frac{r^{-n}}{N} \sum_{m=0}^{N-1} \hat{g}[\delta(\zeta_m) / \Delta t] \cdot e^{-2\pi imn/N}, \tag{17}$$

in which $\hat{g}(\cdot)$ stands for the Laplace-transform of the function $g(t)$, and

$$\delta(\zeta_m) = \sum_{j=1}^2 (1-\zeta_m)^j / 2, \quad \zeta_m = r \cdot e^{2\pi im/N}, \quad r = \varepsilon^{1/(2N)}, \tag{18}$$

with ε being the numerical error in computing the Laplace-transform $\hat{g}(\cdot)$.

For the spatial discretization of the crack-faces, discontinuous quadratic shape function for elements away from the crack-tips and discontinuous quarter-point shape function for elements adjacent to the crack-tips are applied. For the spatial discretization of the external boundary, standard continuous quadratic shape function is used. Hypersingular boundary integrals are computed analytically and numerically by using a special regularization technique based on a suitable change of variable consistent with the used fundamental solutions [3,4]. Regular boundary integrals and line-integrals over a unit-circle contained in the dynamic piezoelectric fundamental solutions are computed numerically by using standard Gaussian quadrature formula.

After temporal and spatial discretizations, a system of linear algebraic equations can be obtained as

$$\sum_{j=0}^n \mathbf{H}^{n-j} \cdot \mathbf{U}^j = \sum_{j=0}^n \mathbf{G}^{n-j} \cdot \mathbf{P}^j, \quad n=0,1,2,\dots,N, \quad (19)$$

where \mathbf{G}^{n-j} and \mathbf{H}^{n-j} are the time-domain system matrices, \mathbf{U}^j is the vector containing the generalized boundary displacements and the generalized CODs, and \mathbf{P}^j is the traction vector for the external boundary and the crack-faces. The time-domain system matrices \mathbf{G}^{n-j} and \mathbf{H}^{n-j} can be obtained by using eq (17), i.e.,

$$\mathbf{H}^{n-j}(\Delta t) = \frac{r^{-(n-j)}}{N} \sum_{m=0}^{N-1} \hat{\mathbf{H}}[\delta(\zeta_m)/\Delta t] \cdot e^{-2\pi im(n-j)/N}, \quad (20)$$

$$\mathbf{G}^{n-j}(\Delta t) = \frac{r^{-(n-j)}}{N} \sum_{m=0}^{N-1} \hat{\mathbf{G}}[\delta(\zeta_m)/\Delta t] \cdot e^{-2\pi im(n-j)/N}, \quad (21)$$

where $\hat{\mathbf{G}}(\cdot)$ and $\hat{\mathbf{H}}(\cdot)$ are the Laplace-domain system matrices, whose computation requires only the Laplace-domain instead of the time-domain dynamic piezoelectric fundamental solutions. This special feature distinguishes the present time-domain BEM from the classical time-domain BEM formulation. In this analysis, the Laplace-domain dynamic piezoelectric fundamental solutions derived by Wang and Zhang [6] are implemented.

By invoking the boundary conditions (8)-(10), equation (19) can be rearranged as

$$\sum_{j=0}^n \mathbf{A}^{n-j} \cdot \mathbf{X}^j = \mathbf{Y}^n, \quad n=0,1,2,\dots,N, \quad (22)$$

where \mathbf{X}^j denotes the vector of the unknown boundary quantities, while \mathbf{Y}^n is the vector of the known or prescribed boundary quantities. By using the initial conditions (7), we obtain an explicit time-stepping scheme as

$$\mathbf{X}^n = (\mathbf{A}^0)^{-1} \cdot \left(\mathbf{Y}^n - \sum_{j=1}^{n-1} \mathbf{A}^{n-j} \cdot \mathbf{X}^j \right), \quad n=1,2,\dots,N. \quad (23)$$

Equation (23) can be used for computing the unknown boundary quantities including the generalized CODs time-step by time-step. Subsequently, the dynamic stress intensity factors and the dynamic electrical displacement intensity factor can be computed from the numerically determined generalized CODs.

Numerical results and discussions

As numerical example, we consider a finite crack of length $2a$ in a homogeneous and linear piezoelectric plate as shown in Fig. 1. The corresponding crack problem in an infinite, homogeneous and linear piezoelectric solid has been investigated by Garcia-Sanchez *et al.* [4]. The cracked plate is subjected either to an impact tensile mechanical loading of the form $\sigma_{22} = \sigma(t) = \sigma_0 \cdot H(t)$, or to an impact electrical loading of the form $D_2 = D(t) = D_0 \cdot H(t)$, or a combination of both impact loadings, where σ_0 and D_0 are the loading amplitudes and $H(t)$ is the Heaviside step function. PZT-5H with the following material properties is considered in the numerical calculations:

$$\begin{aligned} C_{11} &= 126.0 \text{ GPa}; C_{12} = 84.1 \text{ GPa}; C_{22} = 117.0 \text{ GPa}; C_{66} = 23.0 \text{ GPa}; \\ e_{21} &= -6.5 \text{ C/m}^2; e_{22} = 23.3 \text{ C/m}^2; e_{16} = 17.0 \text{ C/m}^2; \\ \kappa_{11} &= 15.04 \text{ C/GVm}; \kappa_{22} = 13.0 \text{ C/GVm}; \\ \text{Mass density } \rho &= 7500.0 \text{ kg/m}^3. \end{aligned}$$

The geometry of the cracked plate is described by $h = 40 \text{ mm}$ and $a = 2.4 \text{ mm}$. Plane strain condition is assumed. For convenience of the presentation, the following normalized dynamic stress intensity factor and dynamic electrical displacement intensity factor are introduced

$$K_I^*(t) = \frac{K_I(t)}{K_I^{st}}, \quad K_{IV}^*(t) = \Lambda \frac{K_{IV}(t)}{K_I^{st}}, \quad (24)$$

where

$$\Lambda = \frac{e_{22}}{\kappa_{22}}, \quad K_I^{st} = \sigma_0 \sqrt{\pi a}. \tag{25}$$

To measure the intensity of the electrical impact, the following loading parameter is defined

$$\lambda = \frac{e_{22}}{\kappa_{22}} \cdot \frac{D_{22}}{\sigma_{22}}. \tag{26}$$

On the external boundary of the cracked plate, 24 standard continuous quadratic elements are used, while 10 discontinuous quadratic elements on the crack-faces including two discontinuous quarter-point elements at the crack-tips are applied. The use of quarter-point elements at the crack-tips enables us to describe the local behavior of the generalized CODs at the crack-tips correctly, and ensures a direct and accurate computation of the dynamic intensity factors from the numerically computed generalized CODs.

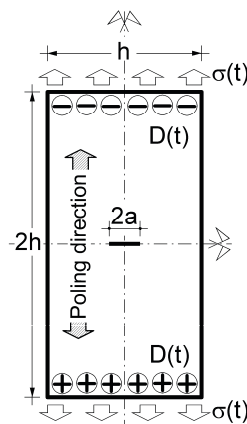


Fig. 1: A crack of length $2a$ in a piezoelectric plate subjected to an impact loading

To check the accuracy of the present time-domain BEM, numerical calculations are carried for $\lambda = 1.0$ by using a time-step $\Delta t = 0.2a/c_L$, where $c_L = \sqrt{(C_{22} + e_{22}^2/\kappa_{22})/\rho}$ is the velocity of the longitudinal wave along the second principal material axis. Numerical results for the normalized dynamic intensity factors are presented and compared with the FEM results in Fig. 2. The FEM results are obtained by using ANSYS. A comparison of both numerical results shows a very good agreement.

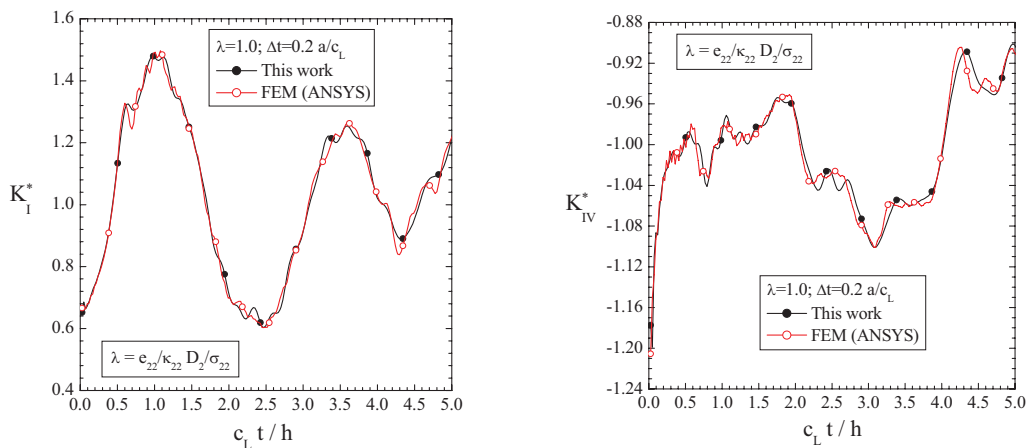


Fig. 2: Normalized dynamic intensity factors versus the dimensionless time

For several values of the loading parameter λ , the normalized dynamic intensity factors are shown in Fig. 3 versus the dimensionless time. Figure 3 implies that the maximum values of the normalized dynamic intensity factors are reduced with increasing loading parameter λ . Also, the electrical impact could cause a crack-face contact, which is characterized by a negative value of $K_I^*(t)$. Similar to the elastodynamic case without piezo-effects, the normalized dynamic stress intensity factor $K_I^*(t)$ shows a dynamic overshoot over its corresponding static value. For dynamic crack problems in linear piezoelectric solids as considered here, the dynamic overshoot of $K_I^*(t)$ depends also on the intensity of the electrical impact as can be seen in Fig. 3.

Finally, figure 4 shows the effects of the direction of the applied electrical impact on the normalized intensity factors. A change of the sign in the loading parameter λ , which means a change of the direction in the applied electrical impact loading for a fixed mechanical impact loading, does not change the amplitude of the normalized dynamic intensity factors, but it leads to a change of the sign in the normalized dynamic intensity factors.

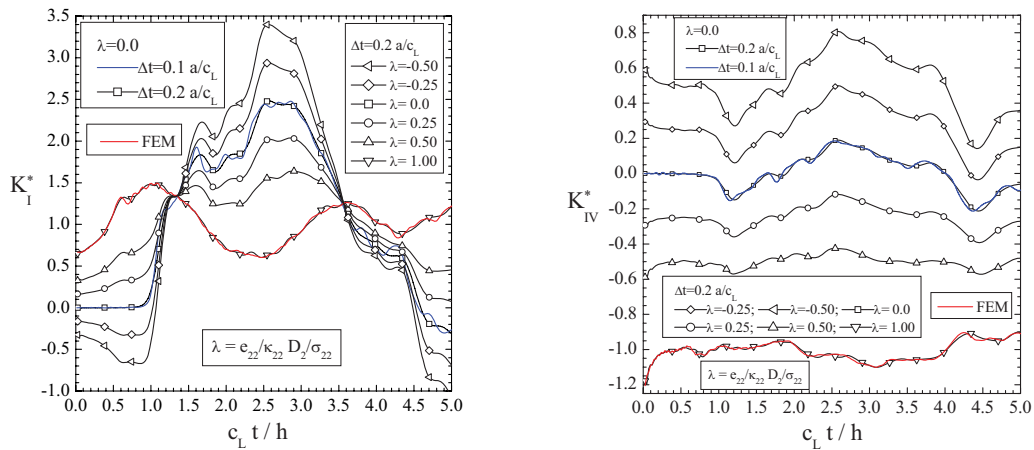


Fig. 3: Normalized dynamic intensity factors for different values of the loading parameter λ

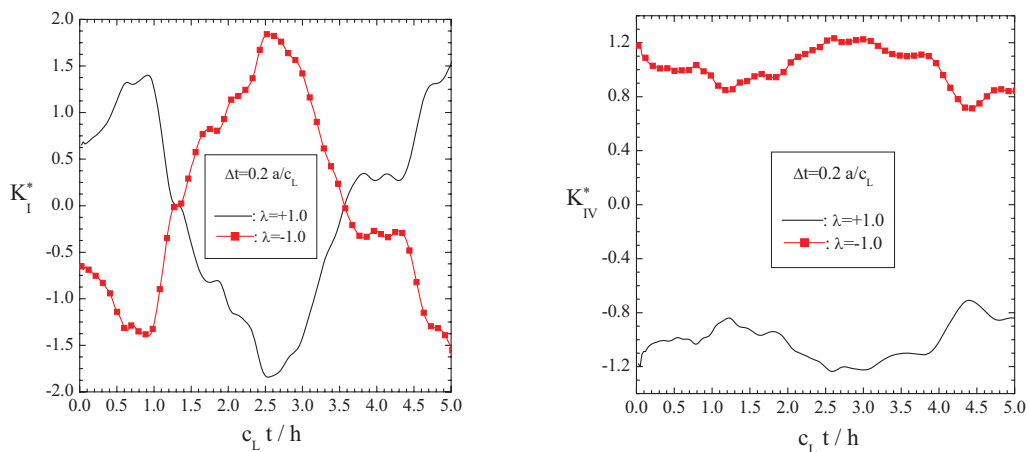


Fig. 4: Effect of the direction of the electrical impact on the normalized dynamic intensity factors

Conclusions

In this paper, a 2-D time-domain BEM for transient dynamic crack analysis in homogeneous and linear piezoelectric solids is presented. The present time-domain BEM uses a combination of the strongly singular displacement BIEs and the hypersingular traction BIEs. The convolution quadrature formula of Lubich [1,2] is adopted for the temporal discretization, while collocation method is implemented for the spatial discretization of the time-domain BIEs. To verify the accuracy of the present time-domain BEM, numerical results for the dynamic intensity factors are presented and compared with the FEM results. The effects of the electrical impact loading on the dynamic intensity factors are analyzed and discussed.

Acknowledgements

This work is supported by the German Research Foundation (DFG) under the project number ZH 15/6-1, and the German Academic Exchange Service (DAAD) under the project number D/04/42255, which are gratefully acknowledged.

References

- [1] C. Lubich *Numerische Mathematik*, **52**, 129-145 (1988).
- [2] C. Lubich *Numerische Mathematik*, **52**, 413-425 (1988).
- [3] F. Garcia-Sanchez, A. Saez and J. Dominguez *Computers & Structures*, **83**, 804-820 (2005).
- [4] F. Garcia-Sanchez, Ch. Zhang, J. Sladek and V. Sladek *Computational Materials Science*, in press, 2006.
- [5] N. Khutoryansky and H. Sosa *International Journal of Solids and Structures*, **32**, 3307-3325 (1995).
- [6] C.-Y. Wang and Ch. Zhang *Engineering Analysis with Boundary Elements*, **29**, 454-465 (2005).

Boundary Element Model for Breakup of a Free Conducting Droplet in the Electric Field

K. Adamiak¹, and J.M. Floryan²

¹ Department of Electrical and Computer Engineering, kadamiak@eng.uwo.ca

² Department of Mechanical and Materials Engineering, floryan@eng.uwo.ca

The University of Western Ontario, London, Ontario, Canada N6A 5B9

Keywords: droplet distortion, electric field, electrocapillary effect, Laplace equation, Boundary Element Method.

Abstract. This paper presents a numerical algorithm for simulating distortion and breakup of a liquid conducting droplet in an electric field. The droplet is suspended in a dielectric medium without gravity and an external uniform electric field is applied. The elongation continues until two thin liquid jets are formed at both ends of the droplet. The algorithm involves simulation of three different phenomena: electric field, droplet distortion and fluid flow. After neglecting space charge and viscosity of the fluid, two of these problems are governed by the Laplace equation, although in different computational domains and with different boundary conditions. In both cases the Boundary Element Method was effectively used as a numerical tool. Examples of dynamics of the droplet elongation and droplet shapes are shown.

Introduction

Although the first electrohydrodynamic phenomena were discovered more than 100 years ago, it was not until 1980's when researchers and engineers have realized their practical importance [1]. First, this happened for electrostatic spraying of liquids in agriculture and industry, more recently in the so-called digital microfluidics [2]. Liquid droplets can be produced, transported, deformed, broken-up and coalesced using the electric forces. The fluid surface tension can be altered using electric forces (electrocapillary effect) and the solid surface wetting can be controlled (electrowetting effect). Depending on an application, the droplet fluids can be conducting, semiconducting or insulating (dielectric). Free droplets suspended in gas or liquid phases, and sessile or pending droplets have been studied. The typical configuration in microfluidics involves a sessile droplet placed on a thin dielectric film, backed with conducting electrodes – a voltage is applied between the droplet and the counter-electrode [3]. A combination of the electrocapillary and electrowetting effects allows for the droplet manipulation. The paper presents a numerical algorithm, which can be used to predict dynamics of the droplet distortion and break-up.

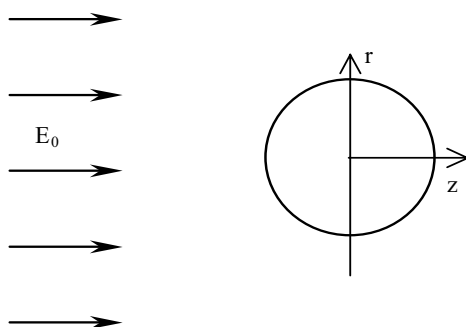


Fig. 1 A conducting droplet suspended in dielectric medium and exposed to a uniform electric field

Mathematical Model

In the simplest case of a free liquid droplet in an external uniform electric field (Fig.1) the surface charges are induced on the droplet surface. The mutual field-charge interaction results in the Coulomb force elongating the droplet in the direction of the field lines. The field magnitude and fluid parameters control the droplet shape, but also the distortion dynamics: for the strong electric fields the droplet elongation increases, the process is faster and the droplet can eventually be disintegrated.

The full simulation of the droplet distortion involves calculation of the

electric field, fluid flow, pressure and the surface shape [4]. Assuming that the droplet is conducting and that the ambient medium is uniform and uncharged, the electric potential V is governed by the Laplace equation

$$\nabla^2 V = 0 \quad (1)$$

with the Dirichlet boundary conditions

$$V|_F = 0 \quad (2)$$

where F is the droplet surface.

The droplet shape is calculated by solving the Laplace-Young equation, which results from the balance of capillary and electric forces:

$$-\rho g z + \sigma \left(\frac{1}{R_1} + \frac{1}{R_2} \right) + \frac{\varepsilon E_n^2}{2} + p = 0 \quad (3)$$

where ρ is the fluid density, g – the gravitational acceleration, z – the axial coordinate, γ – the surface tension, $1/R_1 + 1/R_2$ – the sum of principal radii of curvature, ε – the permittivity of ambient medium, E_n – the normal component of the electric field and p – the pressure difference. Under normal conditions the gravity is often negligible.

The fluid flow caused by the surface distortion is usually the most difficult part of the algorithm, as it requires solution of the Navier-Stokes equation. However, for fast distortions the effects of fluid viscosity can be neglected and so-called potential flow can be assumed. A new scalar function, called the flow potential Φ is defined as $\mathbf{u} = -\nabla\Phi$, where \mathbf{u} is the flow velocity vector. The potential Φ satisfies again the Laplace equation

$$\nabla^2 \Phi = 0 \quad (4)$$

but this time with the kinematic boundary conditions

$$\frac{\partial F}{\partial t} + \nabla\Phi \cdot \nabla F = 0 \quad (5)$$

where F is the droplet surface equation.

Finally, the Bernoulli equation has to be also satisfied

$$\frac{\partial \Phi}{\partial t} + p + \nabla\Phi \cdot \nabla\Phi / 2 = 0 \quad (6)$$

Numerical Algorithm

The numerical algorithm involves four different problems, which are solved iteratively: assuming initially stationary and undistorted droplet the electric field is calculated. The normal component of the electric field is sufficient to calculate the droplet elongation from the capillary equation. The droplet elongation causes the fluid motion, so the fluid potential needs to be determined. In the final step, the pressure inside of the droplet has to be evaluated from the Bernoulli equation. All these steps are repeated until convergence is achieved for one time step. The process continues for required number of steps, or until a steady state is reached, or until the droplet is disintegrated.

The total number of iterations in this process can be very high. For this reason fast techniques must be adopted for all four equations. When the Finite Difference Method is applied to the capillary equation, it is converted to a nonlinear algebraic equation, which can be easily solved. The Bernoulli equation leads to a

simple adding. For both Laplace equations the Boundary Element Technique has been selected as a numerical tool, because of a few important reasons: the electric field domain is open, normal electric field is proportional to the surface charge density, which is the principal unknown, if an appropriate version of the BEM is used, only boundary parameters are involved (no need to calculate any parameters at arbitrary points in space), and easiness of local adjustment of the discretization, if the droplet is elongated.

For both cases (electric field and fluid flow), a simple layer potential was used to formulate the integral equations. The electric potential has to satisfy the Dirichlet boundary conditions, therefore, the Fredholm integral of the first kind can be derived

$$\int_{\Gamma} \rho(Q)E(P,Q)d\Gamma = -E_0z \tag{7}$$

where $E(P,Q)$ is the Green function, P and Q field and source points on the droplet surface. As this problem is two-dimensional in the cylindrical coordinates, the Green function is given as

$$G(P,Q) = \frac{k}{2\pi\epsilon} \sqrt{\frac{r_p}{r_q}} K(k) \tag{8}$$

where r_p and r_q are radial coordinates of points P and Q , respectively, $K(k)$ is the complete elliptic function of the first order with parameter k equal to

$$k^2 = \frac{2r_p r_q}{(r_p + r_q)^2 + (z_p - z_q)^2}$$

The boundary equations for the fluid potential are of the Neumann kind, so the simple layer potential formulaation leads to the Fredholm integral equation of the second kind

$$\frac{\sigma(P)}{2\pi} + \int_{\Gamma} \sigma(Q) \frac{\partial}{\partial n} E(P,Q)d\Gamma = \frac{\partial \Phi}{\partial n} \tag{9}$$

where the normal derivative of Φ is calculated from the kinematic boundary condition (5).

After Eq.(9) is solved for the function $\sigma(P)$, the value of potential Φ at any point of space can be calculated by simple integration

$$\Phi(R) = \int_{\Gamma} \sigma(Q)E(R,Q)d\Gamma$$

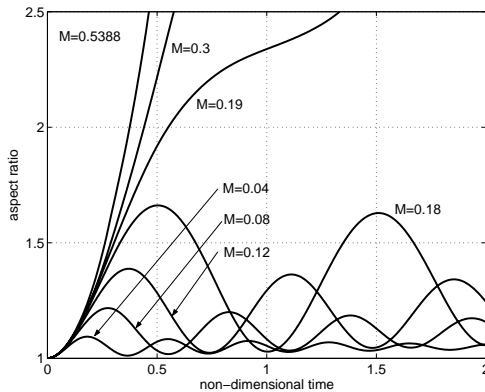


Fig. 2 Transient elongation of liquid droplet in an electric field for different values of parameter M

The conventional Boundary Element Method was used to solve Equations (7) and (9): first the droplet surface was discretized into some number (usually between 50 and 200) of linear elements with two nodes at both ends. The node distribution was non-uniform: very small elements were used close to the droplet tip, where the most significant surface distortion was expected, with much larger elements in other areas. Additional nodes can be added during iterations, if too large elements are created due to the droplet elongation. This procedure converts the integral equations into sets of linear algebraic equations, which can be solved easily.

Results

The numerical algorithm has been tested on many different examples, with varying field strengths and voltage waveforms. In order to reduce the number of different parameters affecting the solution all equations were written in the non-dimensional form. Normalizing all distances with respect of the radius of an undistorted droplet R , the electric field with respect of the intensity of the external uniform field E_0 , velocity with $\sqrt{\epsilon_0/\rho}E_0$, and time with $R/E_0\sqrt{\rho/\epsilon_0}$, makes it possible to prove that all equations in the non-dimensional form remain identical, except for the capillary equation, which assumes the form:

$$\frac{1}{R_1^*} + \frac{1}{R_2^*} + M\left(\frac{1}{2}E_n^{*2} + p^* + G^*\right) = 0 \tag{7}$$

where $M = \epsilon_0 R E_0^2 / \sigma$ is the only non-dimensional parameter affecting the process; physically it is a ratio of electrical and capillary forces. When $M \rightarrow 0$ the electric effects are negligible and capillary effects dominate. When $M \rightarrow \infty$ the capillary forces can be neglected as compared with the electrical ones.

When the electric field is not very strong the droplet is elongated and eventually starts to oscillate (Fig.2). The amplitude and frequency of oscillations depends on the electric field intensity: When $M=0.04$ the amplitude is very small and frequency high. Theoretically, the oscillations should not be damped – small attenuation seen in Fig. 2 is probably a numerical artifact. For real droplets a similar effect could be caused

by the fluid viscosity, but an ideal fluid has been assumed in this paper. With increasing M the oscillations are larger and slower.

When a sufficiently high field is applied, the droplet is elongated and no steady state can be reached. The process continues until eventually a sharp conical tip and liquid jet is formed (Fig. 3). This tip accelerates fast and small droplets are detached due to the capillary instability. This happens because the equilibrium between capillary and electric forces doesn't exist. The relative electric field distributions on the surface of the droplet for $M=0.5388$ and different instants of time are given in Fig.4. For the ideally spherical droplet at $t=0$ the maximum electric field is three times larger than the external field. At the point of the droplet break-up this ratio can be close to hundred.

There is a known theory that the droplet surface forms a sharp cone at the point of break-up, called the Taylor cone [5]. The computational results for different values of the non-dimensional number M confirm existence of a sharp point (Fig. 6). However, contrary to Taylor's prediction, the angle of this cone is not constant and depends on the value of M . An additional effect, never reported before, has also been noticed. When the electric field is sufficiently strong the droplet is not only elongated in the direction of the electric field, but also a neck is formed in the vertical plane of symmetry. The numerical predictions have been compared with some experimental data obtained in microgravity conditions: agreement was satisfactory [6]. In particular, the existence

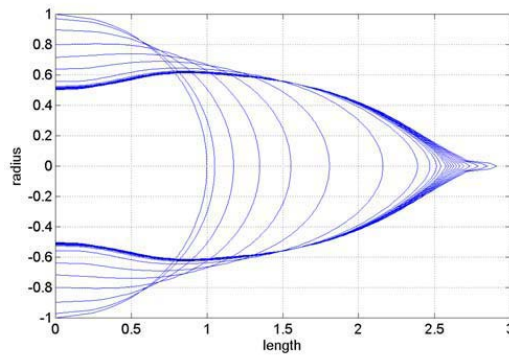


Fig. 3 Time evolution of the liquid droplet in a uniform electric field for $M=0.5388$

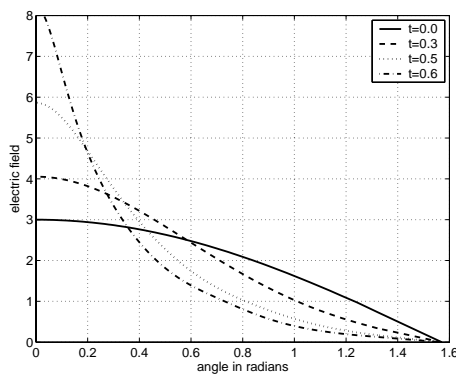


Fig. 4 Electric field intensity on the surface of liquid droplet at different instants of time

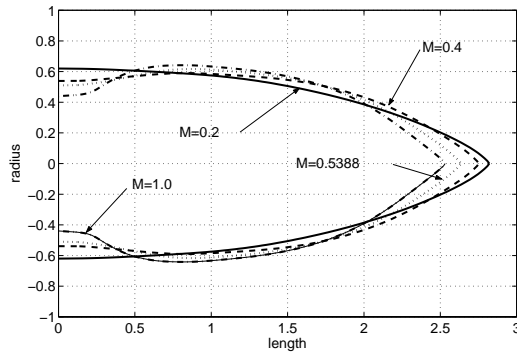


Fig. 5 Shape of the droplet prior to break-up point for different non-dimensional numbers M

The Boundary Element Method was a preferable technique for three important reasons: it naturally handles the electric boundary conditions at infinity, requires discretization of the droplet surface only and is easily adopted for the moving shape of the droplet.

The results of computation show behaviour of the distortion of a conducting droplet in a uniform electric field: elongation along the field lines, forming a thin jet at the tip and, eventually, forming a neck in the middle of the droplet. Depending of the electric field magnitude, the droplet will oscillate or will be disintegrated.

Acknowledgments

This work was supported in part by the Natural Sciences and Engineering Research Council of Canada (NSERC).

References

- [1] F. Mugele and J.-Ch. Baret *J. Phys.: Condens. Matter*, **17**, R705-R774 (2005).
- [2] M.G. Pollack, A.D. Shenderov and R.B. Fair *Lab on the Chip*, **2**, 96-101 (2002).
- [3] A.A. Darhuber and S.M. Troian *Ann. Rev. Fluid Mech.*, **37**, 425-455 (2005).
- [4] K. Adamiak Numerical investigation of shape of liquid droplets in an electric field. In C.A. Brebbia, S. Kim, T.A. Oswald, H. Power (eds.) *Boundary Elements XVII*, Comp. Mech. Publ., Southampton, pp. 459-469 (1995).
- [5] G. Taylor *Proc. R. Soc. London A*, **280**, 383-397 (1964).
- [6] K. Adamiak and J.M. Floryan *Proc. of IEJ-ESA Joint Symposium on Electrostatics*, Tokyo, Japan, pp. 191-199 (2004).

of a neck in the area close the droplet symmetry plane and forming a thin jet from the droplet tip have been confirmed, if the electric field is sufficiently strong.

Conclusions

A numerical algorithm for predicting dynamic distortion of a water droplet in an external electric field has been presented in the paper. The important part of this algorithm is a double solver for the Laplace equation: one governing the electric field distribution, another fluid flow inside of the droplet. As this equation has to be sometimes solved thousands of times, effectiveness of the solver is crucial for the success of the whole algorithm.